Freeze-in Production of Scalar Singlet Dark Matter

Scrutinizing the effect of quantum statistics and electroweak phase transition in the early universe

Kristian Gjestad Vangsnes

Thesis submitted for the degree of
Master in Theoretical Physics

Institute of Physics
Faculty of mathematics and natural sciences

UNIVERSITY OF OSLO

Spring 2021

Freeze-in Production of Scalar Singlet Dark Matter

Scrutinizing the effect of quantum statistics and electroweak phase transition in the early universe

Kristian Gjestad Vangsnes

Freeze-in Production of Scalar Singlet Dark Matter

http://www.duo.uio.no/

Printed: Reprosentralen, University of Oslo

Abstract

The mystery of dark matter (DM) has intrigued scientists for many decades. The type of DM particles that has been studied the most is Weakly Interacting Massive Particles (WIMPs). These particles are assumed to have been in thermal equilibrium with the visible sector heat bath at early times, and experienced freeze-out when the expansion rate of the universe became bigger than the interaction rate. However, the null result from DM searches and the shrinking parameter space for WIMP models have made it crucial to look at other models. A fascinating model to study is one that includes a Feebly Interacting Massive Particle (FIMP). These particles are assumed to never be in thermal equilibrium with the visible sector heat bath and are produced by the freeze-in mechanism. They naturally evade experimental constraints while explaining the observed relic density. Since FIMPs are never in thermal equilibrium with the visible sector, any thermal effect on the FIMP abundance will have to be accounted for. This is the main goal of this thesis. I consider the thermal effects coming from electroweak symmetry breaking (EWSB), thermal contribution to the masses and the QCD phase transition in the early universe for the scalar singlet model, where I include both higher order correction to the Standard Model (SM) couplings and quantum statistical effects. These effects result in an important correction to the DM relic abundance when the dominant contribution does not arise from Higgs boson decays, which happens when decays into scalar singlets are kinetically forbidden or if the reheating temperature after inflation is much smaller than the Higgs boson mass. Freeze-in has also been implemented in the FORTRAN package DarkSUSY together with the thermal effects for the scalar singlet model.

Acknowledgements

First and foremost, I would like to express my sincere gratitude to my supervisor Torsten Bringmann. I would not have been able to complete this thesis without your constant guidance, support, and feedback.

I would also like to thank Torsten Bringmann, Felix Kahlhoefer and Saniya Heeba for a wonderful collaboration. It has been a pleasure working with you, and I have learned a lot this year from our meetings.

I would also thank all the people at the theory section, both for enjoyable lunch breaks and fruitful discussions.

A sincere thanks also goes out to Sunniva for the constant love and support.

Finally, I would like to thank family and friends for all the love and encouragement they have provided.

Contents

Chapter 1

Introduction

One of the biggest mysteries in science is Dark Matter (DM), the matter component that makes up most of the matter in our universe. The reason DM is difficult to study is because the only observations we have are due to its gravitational nature. However, due to the advancement of cosmology in the last couple of decades, the Lambda cold dark matter model (ΛCDM) has exhibited great success and there is now scientific consensus that the dark matter paradigm is correct. The non-gravitational nature of DM is still a mystery, but we know its abundance is roughly a factor five the size of the visible matter abundance [1]. Models where the visible sector and DM are assumed to have been in thermal equilibrium in the early universe have been thoroughly studied in the last decades. The most prominent model is one that features Weakly Interacting Massive Particles (WIMPs) [2]. WIMPs will typically have masses and couplings to the Standard Model (SM) reminiscent to that of the weak scale, and the fact that this will give the observed relic abundance is the celebrated *WIMP miracle* [3]. WIMPs will decouple from the heat bath when the expansion rate of the universe becomes bigger than the interaction rate between the WIMPs and the visible sector heat bath [4]. This is the so-called *freeze-out* mechanism. A lot of work has gone into searches for WIMPs. In direct detection, scattering of DM with a nucleus here on earth is looked for. In indirect detection experiments one looks for annihilation products from DM collisions, and at collider searches one tries to observe DM production. However, the null result from these searches have made many researchers look at other models and production mechanisms. A promising class of DM candidates is the Feebly Interacting Massive Particles (FIMPs) [5]. These particles never reach thermal equilibrium with the visible sector, because their coupling to the visible sector is much smaller than the couplings WIMPs have. This would naturally explain the null result from DM searches, while the observed DM abundance can be produced by the *freeze-in* mechanism [5]. Since the coupling to the visible sector is very small, the DM abundance will solely be due to the annihilation or decay of visible sector particles into DM. The annihilation of DM will be negligible due to the smallness of the coupling. The fact that WIMPs must be in thermal equilibrium with the visible heat bath, means that any thermal effects before

decoupling will be washed away. For FIMPs, this is no longer the case. This means that one has to properly account for the thermal effects due to the plasma physics and events in the early universe before the FIMPs freeze-in, e.g. thermal masses, electroweak symmetry breaking and the QCD phase transition. The main goal of this work is to include such effects and apply them to an attractive DM model, namely the scalar singlet model [6]. This model is one of the simplest extensions of the SM. It is simply a new real scalar coupled to the SM through a four-point interaction with the complex Higgs doublet. I will explore the abundance coming from the freeze-in mechanism, where higher order effects, quantum statistical effects and thermal events such as the electroweak and the QCD phase transition will be included. The second goal is to implement freeze-in in the FORTRAN package DarkSUSY [7]. This will be done by rewriting the Boltzmann-equation for freeze-in on a form that is suitable for numerical implementation. This implementation will then be used to study the different effects on the scalar singlet model.

Thesis overview

This thesis is divided into four parts. In the first part I will go through the background physics relevant for the thesis. I start in chapter 2 with a short introduction to cosmology, while in chapter 3 I review how thermodynamics is applied to an expanding universe. This includes an introduction to equilibrium thermodynamics and the Boltzmann equation.

In the second part I will focus on dark matter. I start by giving the most compelling evidence we have for the existence of DM and the constraints this sets on the DM particle(s). I then introduce some of the most popular DM candidates and their properties. The most popular detection methods are presented together with their current limits. The standard treatment of freeze-out is reviewed and in chapter 5 the freeze-in mechanism is presented. I will start by explaining how the freeze-in mechanism works before presenting a non-standard way of calculating the relic density, one that is better for numerical implementation. I will also include both relativistic and quantum statistical effects.

In the third part I will start by reviewing how thermal effects are included, specifically the thermal effects on the effective Higgs potential and the Higgs mass, together with a discussion about phase transitions. I will then look at how higher order effects can be included for models where annihilations into SM final states proceed via the so-called Higgs portal. This includes a new and effective way of avoiding unitarity violation when higher order corrections are included.

In the last part I will introduce the scalar singlet model and apply the formalism I have introduced in the previous parts to it. I will specifically look at the cases where

we either have a high reheating temperature or a low reheating temperature. I will then in section 8.4 give a summary and discuss my results. Finally, the conclusions are presented in chapter 9.

I have implemented numerical solutions to the freeze-in Boltzmann equation together with the temperature- and higher order dependence to the scalar singlet model into the widely used FORTRAN package DarkSUSY [7]. An introduction to DarkSUSY and the routines I have implemented is given in appendix A. In appendix B I show that the special case when we have an s-channel resonance will in fact give the same relic abundance as when we have on-shell decay when Maxwell-Boltzmann (MB) distributions are used for the standard model particles. The main result in this work will be in a manuscript currently being prepared for submission to the Journal of Cosmology and Astroparticle Physics (JCAP), in collaboration with Torsten Bringmann, Felix Kahlhoefer (RWTH Aachen) and Saniya Heeba (RWTH Aachen).

Part I

Background Physics

Chapter 2

Cosmology

2.1 Friedmann-Robertson-Walker universe

In this chapter I will give a short introduction to the aspects of cosmology needed in this thesis, for a more thorough review covering the content in this chapter see chapter 8 of Sean Carroll's book *Spacetime and geometry* [8] or chapter 2 of E. Kolb & M. Turner's *The Early Universe* [4].

The cornerstone of cosmology is the cosmological principle, which states that the matter and radiation distribution of the universe is isotropic and homogeneous at scales corresponding to the size of the observable universe. Isotropic simply means that at a point, the distribution looks the same in all directions and homogeneous means that the metric is the same at all points in our universe. The universe is obviously not isotropic at smaller scales such as solar systems or galaxies, but at scales of order 100 Mpc or larger it is [4]. I want to stress that we cannot check if the universe is homogeneous since we cannot travel to all places of the universe, but the observable universe looks homogeneous from our vantage point. The fact that a 3D space is isotropic and homogeneous is the same as saying that it is maximally symmetric. The metric that describes a maximally symmetric space is the **Friedman-Robertson-Walker (FRW) metric**

$$ds^2 = dt^2 - a(t)^2 \left(\frac{dr^2}{1 - kr^2} + r^2 d\Omega^2 \right) , \tag{2.1}$$

where $a(t)$ is called the *scale factor*, while r, θ and ϕ are comoving coordinates and $d\Omega^2 = d\theta^2 + \sin^2\theta d\phi^2$. The factor k is chosen to be 0, 1 or -1, depending on whether the space is flat, has constant positive or constant negative curvature, respectively.

The Planck 2018 [1] observations are consistent with a flat universe, i.e. $k = 0$. The instantaneous physical distance d_P, between us ($r = 0$) and some galaxy at a

radial coordinate r, is then given by [8]

$$d_P(t) = a(t)r \ . \tag{2.2}$$

I will treat $a(t)$ to be dimensionless, where the scale factor today $t = t_0$ is $a_0 \equiv a(t_0) = 1$. From now on, if a parameter has subscript 0, it means the present value. Assuming that the galaxy's peculiar velocity is negligible ($\dot{r} = 0$), the instantaneous velocity is then given by

$$v_P = Hd_P \ , \tag{2.3}$$

where I have used that $\dot{r} \equiv \frac{dr}{dt}$ and $H \equiv \frac{\dot{a}}{a}$ is the *Hubble rate*. It is important to note that d_P is not observable since all observations we do are of our past light cone. We can use that a measurable distance to the object and the instantaneous physical distance coincide within reasonable errors if the redshift of some stellar object is very small. An example of a measurable distance is the **luminosity distance**, d_L, which is defined by

$$d_L^2 = \frac{L}{4\pi F} \ , \tag{2.4}$$

where L is the object's absolute luminosity and F is the flux measured by the observer. Evaluating Eq.(2.3) today we get **Hubble's Law**

$$v_P = H_0 d_P \ , \tag{2.5}$$

where $H_0 \equiv H(t_0)$ is the *Hubble constant*, which by today's best measurements[1] is $H_0 = (67.27 \pm 0.60)$ km s^{-1}Mpc^{-1} [1]. This is an important parameter which usually is defined in terms of the dimensionless parameter h, where

$$H_0 = 100h \text{ km s}^{-1}\text{Mpc}^{-1} \ . \tag{2.6}$$

Stress-energy tensor

The fact that space is homogeneous and isotropic poses constraints on which stress-energy tensors we can use. I will use the stress-energy for a perfect fluid which is given by two parameters, the energy density $\rho(t)$ and the pressure $p(t)$

$$T_{\mu\nu} = (\rho + p)U_\mu U_\nu - pg_{\mu\nu} \ , \tag{2.7}$$

where U_μ is the four-velocity to the reference frame with respect to the comoving coordinates to the fluid. In the comoving frame the fluid is at rest. This is due to the cosmological principle since the frame where the fluid is isotropic is the same frame as the frame where the metric is isotropic. The four-velocity in the comoving frame is thus given by

$$U_\mu = (1, 0, 0, 0) \ , \tag{2.8}$$

[1]This value is inferred from the cosmic microwave background. There is a non-zero discrepancy between this value and the value of H_0 found from local experiments using Eq.(2.5).

which means that the stress-energy tensor in the comoving frame becomes

$$T^{\mu}_{\nu} = \mathrm{diag}(-\rho, p, p, p) \ . \tag{2.9}$$

An equation describing the relationship between ρ and p is called an **equation of state**. I choose the relevant equation of state, which is

$$p = w\rho \ , \tag{2.10}$$

where w is constant in time. Since $\nabla_{\mu} T^{\mu\nu} = 0$, we get that

$$\frac{\dot{\rho}}{\rho} = -3(1+w)\frac{\dot{a}}{a} \ , \tag{2.11}$$

which gives

$$\rho = \rho_0 a^{-3(1+w)} \ . \tag{2.12}$$

The values w can take is dependent on which energy conditions one chooses the fluid to abide. There are three values of w that are of particular interest, they correspond to fluids describing dust (noninteracting and non-relativistic matter), radiation and vacuum energy.

For dust there is no pressure, i.e. $p = 0$. This means that $\rho = \rho_0 a^{-3}$, which is expected since a^{-3} is the factor for diluting the number density in three dimensions. For radiation we know from kinetic gas theory that $p = \frac{1}{3}\rho$, thus from Eq.(2.12) we get that $\rho = \rho_0 a^{-4}$, which also is expected since we get an extra factor of a due to red shift coming from the expansion of the universe. For the vacuum energy we know that the vacuum energy-momentum tensor is

$$T^{\mathrm{vacuum}}_{\mu\nu} = -\frac{\Lambda g_{\mu\nu}}{8\pi G} \ , \tag{2.13}$$

which means that $p = -\rho = \frac{\Lambda}{8\pi G}$.

Friedmann equations

In order to find the time dependence of $a(t)$, we need to apply the Einstein field equations to the FRW-metric. These equations are the **Friedmann equations**

$$\left(\frac{\dot{a}}{a}\right)^2 = \frac{8\pi G}{3}\rho - \frac{k}{a^2} \tag{2.14}$$

and

$$\frac{\ddot{a}}{a} = -\frac{4\pi G}{3}(\rho + 3p) \ . \tag{2.15}$$

We can write the equations in a more convenient form by introducing the useful parameter

$$\Omega \equiv \frac{8\pi G}{3H^2}\rho \equiv \frac{\rho}{\rho_{crit}} \ , \tag{2.16}$$

which is called the **density parameter**, where ρ_{crit} is the **critical density**. Eq.(2.14) will then be

$$\Omega - 1 = \frac{k}{H^2 a^2} \equiv -\frac{\Omega_k}{a^2} \ . \tag{2.17}$$

We can now do the following characterizations

$$\begin{array}{lllllll} \rho < \rho_{crit} & \Leftrightarrow & \Omega < 1 & \Leftrightarrow & k < 0 & \Leftrightarrow & \text{Open} \\ \rho = \rho_{crit} & \Leftrightarrow & \Omega = 1 & \Leftrightarrow & k = 0 & \Leftrightarrow & \text{Flat} \\ \rho > \rho_{crit} & \Leftrightarrow & \Omega > 1 & \Leftrightarrow & k > 0 & \Leftrightarrow & \text{Closed} \end{array}$$

This means that if we experimentally determine the density parameter Ω, we can find out which geometry our universe has. I have implicitly used that the energy density ρ is the sum of all the energy density contributions in our universe, which there are multiple of. From baryons we have the contribution Ω_b, from cold dark matter (CDM) we have the contribution Ω_c, from the vacuum energy we have the contribution Ω_Λ and from the curvature we have the contribution Ω_K. Summing over all of these energy density contributions makes Eq.(2.14) take an even simpler form

$$\sum_i \Omega_i = 1 \ . \tag{2.18}$$

Using Eq.(2.12) we rewrite Eq.(2.18) using the currently observed energy densities

$$1 = \frac{H_0^2}{H^2} \sum_i \frac{\Omega_i(t_0)}{a^{3(1+w_i)}} \ . \tag{2.19}$$

Using that our universe is more or less flat makes the time dependence of $a(t)$ a lot simpler to calculate. Assuming we have a dominant energy density contribution with energy density $\rho \propto a^{-n}$, means we only have to look at the equation

$$\left(\frac{\dot{a}}{a}\right)^2 \propto a^{-n} \ , \tag{2.20}$$

which has the solution

$$a(t) \propto t^{2/n} \ . \tag{2.21}$$

If $\rho \propto$ const, then the solution is

$$a(t) = e^{Ht} \ . \tag{2.22}$$

2.2 The cosmological concordance model

The best model of our universe is the ΛCDM model. This model is composed of CDM, baryons, radiation and a cosmological constant Λ. The Friedmann equation for ΛCDM is therefore

$$\frac{H^2}{H_0^2} = \Omega_\Lambda + \frac{\Omega_c}{a^3} + \frac{\Omega_b}{a^3} + \frac{\Omega_r}{a^4} \ . \tag{2.23}$$

Table 2.1: Density parameters for ΛCDM model from Table 2 in *Planck 2018 results. VI. Cosmological parameters* [1] at 68% confidence level.

Parameter	Value
$\Omega_b h^2$	0.02237 ± 0.00015
$\Omega_c h^2$	0.1200 ± 0.0012
Ω_Λ	0.6847 ± 0.0073
Ω_K	$-0.011^{+0.013}_{-0.012}$

The current values of the density parameters are found in Table 2.1. We see that today, 69% of the energy density in our universe is made up of the cosmological constant (often referred to as dark energy), 26% is made up of CDM and 5% baryons, while curvature and radiation is negligible. We can calculate the age of the universe using that

$$\frac{da}{dt}\frac{1}{a} = H \Rightarrow dt = \frac{da}{aH} = \frac{da}{aH_0\sqrt{\Omega_\Lambda + \frac{\Omega_c}{a^3} + \frac{\Omega_b}{a^3} + \frac{\Omega_r}{a^4}}} \,. \tag{2.24}$$

Integrating from $t = 0$ to today and using the values in Table 2.1 gives us that the age of the universe is

$$t_0 = \frac{1}{H_0}\int_0^1 da \frac{a}{\sqrt{\Omega_\Lambda a^4 + \Omega_m a + \Omega_r + \Omega_K a^2}} \simeq 13.797 \pm 0.023 \text{ Gyr}, \tag{2.25}$$

where the matter contribution (CDM and baryons) is $\Omega_m = \Omega_c + \Omega_b$.

Chapter 3

Thermodynamics in an expanding universe

In this chapter I will review the physics needed to describe particles in a thermal bath which exists in an expanding universe. For a more comprehensive review of the topic I will cover here, see chapter 3 and 5 of E. Kolb & M. Turner's *The Early Universe* [4]. I will introduce concepts such as equilibrium number and energy densities, and I will show their relativistic and non-relativistic limits. I will show how entropy is applied to cosmology and lastly, I will introduce the Boltzmann equation.

3.1 Thermal equilibrium

For most of the universe's early history, its constituents were in kinetic or local thermal equilibrium. The phase-space distribution for such particle species is given by Fermi-Dirac (FD) distribution if the species is fermionic; or Bose-Einstein (BE) distribution if the species is bosonic

$$f_i(\vec{p}) = [\exp((E_i - \mu_i)/T) \pm 1]^{-1} \ , \tag{3.1}$$

where $+1$ gives the Fermi-Dirac distribution and -1 gives the Bose-Einstein distribution. $\vec{p}$ is the three momentum, the energy is $E_i = \sqrt{\vec{p}^2 + m_i^2}$, where m_i is the mass of the species i, μ_i is the chemical-potential and T is the temperature. If $\exp((E_i - \mu_i)/T) \gg 1$ we can use the Maxwell-Boltzmann distribution

$$f_i^{\mathrm{MB}} \equiv \exp[-(E_i - \mu_i)/T] \ . \tag{3.2}$$

It is worth noting that we are using physical momenta and that none of this section takes into account the expansion of the universe, in fact all of this also holds in Minkowski space. This is because we are considering local equilibrium. Given a

distribution function we can, independently of thermal equilibrium, calculate the number density n, energy density ρ and pressure p of a weakly interacting gas composed of particles with g_i internal degrees of freedom

$$n_i = g_i \int \frac{d^3p}{(2\pi)^3} f_i(\vec{p}) \ , \tag{3.3}$$

$$\rho_i = g_i \int \frac{d^3p}{(2\pi)^3} E_i(\vec{p}) f_i(\vec{p}) \ , \tag{3.4}$$

$$p_i = g_i \int \frac{d^3p}{(2\pi)^3} \frac{|\vec{p}|^2}{3E_i} f_i(\vec{p}) \ . \tag{3.5}$$

Furthermore, a species i, interacting with species j, k and l through the interaction

$$i + j \leftrightarrow k + l \ , \tag{3.6}$$

is in chemical equilibrium when

$$\mu_i + \mu_j = \mu_k + \mu_l \ . \tag{3.7}$$

If we can describe the gas using the Maxwell-Boltzmann distribution, chemical equilibrium means physically that the number densities hold the following equality

$$\frac{n_i n_j}{n_k n_l} = \text{const.} \tag{3.8}$$

Relativistic and non-relativistic limits

The relativistic and non-relativistic limits of the number density, energy density and pressure are of particular interest, since more often than not, the species we will look at is either relativistic or non-relativistic. We start by changing variable from p to E using $E^2 = p^2 + m^2$

$$n = \frac{g}{2\pi^2} \int_m^\infty dE \frac{(E^2 - m^2)^{1/2}}{\exp[(E-\mu)/T] \pm 1} E \ , \tag{3.9}$$

$$\rho = \frac{g}{2\pi^2} \int_m^\infty dE \frac{(E^2 - m^2)^{1/2}}{\exp[(E-\mu)/T] \pm 1} E^2 \ , \tag{3.10}$$

$$p = \frac{g}{2\pi^2} \int_m^\infty dE \frac{(E^2 - m^2)^{3/2}}{\exp[(E-\mu)/T] \pm 1} \ . \tag{3.11}$$

If $T \gg m, \mu$, the species will be relativistic. Performing the integrals (3.9) - (3.11), as done in [9], gives us

$$n = \begin{cases} (\zeta(3)/\pi^2) g T^3 & \text{Bosonic} \ , \\ (3/4)(\zeta(3)/\pi^2) g T^3 & \text{Fermionic} \ , \end{cases} \tag{3.12}$$

$$\rho = \begin{cases} (\pi^2/30) g T^4 & \text{Bosonic} \ , \\ (7/8)(\pi^2/30) g T^4 & \text{Fermionic} \ , \end{cases} \tag{3.13}$$

$$p = \rho/3 \ , \tag{3.14}$$

where $\zeta(3) \simeq 1.20206$ is the Riemann zeta function evaluated at 3. The non-relativistic limit ($m \gg T$) gives us

$$n = g \left(\frac{mT}{2\pi} \right)^{3/2} \exp[-(m-\mu)/T] \ , \tag{3.15}$$

$$\rho = mn \ , \tag{3.16}$$

$$p = nT \ll \rho \ . \tag{3.17}$$

We can see that the values for a non-relativistic species will be exponentially smaller than those of a relativistic species. It is therefore convenient and a good approximation to set the energy density of a collection of species to be

$$\rho(T) = \frac{\pi^2}{30} g_{\text{eff}} T^4 \ , \tag{3.18}$$

where T is the temperature of the heat bath and g_{eff} is the total number of effective relativistic degrees of freedom, defined by

$$g_{\text{eff}} = \sum_{i=\text{Bosons}} g_i \left(\frac{T_i}{T} \right)^4 + \frac{7}{8} \sum_{i=\text{Fermions}} g_i \left(\frac{T_i}{T} \right)^4 \ , \tag{3.19}$$

where we see the factor 7/8 comes from Eq.(3.13), which takes the difference between Fermi-Dirac- and Bose-Einstein statistics into consideration. T_i is the temperature of species i, which differ from T if the species has decoupled. The Hubble rate during radiation dominated era can now be written in terms of the temperature of the heath bath using the Friedmann equation, assuming we sum over all the particles species

$$H(T) = \frac{1}{m_P} \sqrt{\frac{8\pi}{3} \rho(T)} = \frac{1}{m_P} \sqrt{\frac{4}{45} \pi^3 g_{\text{eff}}} T^2 \simeq \sqrt{g_{\text{eff}}} \frac{1.66 T^2}{m_P} \ , \tag{3.20}$$

where $m_P = 1.220 \times 10^{19}$ GeV is the Planck mass.

Entropy

A particle species will be in thermal equilibrium and thus a constituent of the heat bath if the interaction rate of particles with the heat bath is sufficiently large ($\Gamma \gtrsim H$). If that is the case, we can apply the first- and second law of thermodynamics to a comoving volume $V = a^3$ to get

$$d(\rho v) = T dS - p dV \ , \tag{3.21}$$

where ρ and p are the energy density and pressure of the heat bath in thermal equilibrium. Using the fact that

$$\frac{\partial^2 S}{\partial T \partial V} = \frac{\partial^2 S}{\partial V \partial T} \ , \tag{3.22}$$

we relate the energy density and the pressure by

$$dp = \frac{\rho + p}{T} dT \ . \tag{3.23}$$

Using Eq.(3.23) in Eq.(3.21) we get

$$dS = d\left[\frac{(\rho + p)V}{T} + \text{const}\right] \ , \tag{3.24}$$

which means that the entropy per comoving volume (up to an additive constant) is given by

$$S = \frac{(\rho + p)a^3}{T} \ . \tag{3.25}$$

This means that we can use Eq.(3.23) to get the rate at which the entropy changes

$$\frac{dS}{dt} = \frac{1}{T}\left[\left(\frac{d}{dt}(a^3\rho) + p\frac{d}{dt}a^3\right) + \frac{dp}{dT}a^3\frac{dT}{dt} - \frac{\rho + p}{T}a^3\frac{dT}{dt}\right] = 0 \ , \tag{3.26}$$

since the term inside the first parenthesis is zero due to $\nabla_\mu T^{\mu\nu} = 0$. This means that entropy per comoving volume is conserved in thermal equilibrium. The entropy density

$$s = \frac{S}{V} = \frac{\rho + p}{T} \ , \tag{3.27}$$

is a useful quantity. For $T \gg m$, where relativistic species dominate, this becomes

$$s(T) = \frac{2\pi^2}{45} h_{\text{eff}} T^3 \ , \tag{3.28}$$

where

$$h_{\text{eff}} \equiv \sum_{i=\text{bosons}} g_i \left(\frac{T_i}{T}\right)^3 + \frac{7}{8} \sum_{i=\text{fermions}} g_i \left(\frac{T_i}{T}\right)^3 \ , \tag{3.29}$$

where we again see the factor 7/8 coming from Eq.(3.13) and Eq.(3.14). This can be used to relate the temperature to the scale-factor when the universe expands adiabatically, meaning the comoving entropy density is conserved in time

$$\frac{d}{dt}(sa^3) = 0 \Rightarrow S = h_{\text{eff}} T^3 a^3 = \text{const.} \tag{3.30}$$

which means

$$T \propto (h_{\text{eff}})^{-1/3} a^{-1} \ . \tag{3.31}$$

We can now relate the time to the temperature of the heath bath using Eq.(3.30) (which amounts to $ds/dt = -3Hs$) and Eq.(3.28)

$$\frac{ds}{dt} = \frac{ds}{dT}\frac{dT}{dt} = \left(\frac{1}{T} + \frac{1}{3h_{\text{eff}}}\frac{dh_{\text{eff}}}{dT}\right) 3s\frac{dT}{dt} \ , \tag{3.32}$$

which means

$$\frac{dT}{dt} = -\overline{H}(T)T \ , \tag{3.33}$$

where

$$\overline{H}(T) \equiv \frac{H}{1 + \frac{1}{3}\frac{T}{h_{\text{eff}}}\frac{dh_{\text{eff}}}{dT}} \ . \tag{3.34}$$

3.2 Boltzmann Equation

There have been multiple important events where some constituents of the visible sector heat bath have departed from thermal equilibrium. Most notably, neutrino decoupling, primordial nucleosynthesis and decoupling of the background radiation, thereby creating the cosmic microwave background (CMB). There are also some important hypothesized events such as inflation, baryogenesis and decoupling of dark matter (DM). These events can be seen in the evolution of the number densities of the particles in the heath bath. In order to study the evolution of a particle species distribution function and thus its number density, I use the Boltzmann equation, which in its most general form can be written as

$$\hat{\mathbf{L}}[f] = \mathbf{C}[f] \ , \tag{3.35}$$

where $\hat{L}$ is the covariant Liouville operator and $\mathbf{C}$ is the collision operator. The Liouville operator is simply given by the variation of f with respect to an affine parameter λ along a geodesic

$$\hat{\mathbf{L}}[f] = \frac{dx^i}{d\lambda}\frac{\partial f}{\partial x^i} + \frac{dp^i}{d\lambda}\frac{\partial f}{\partial p^i} = p^i\frac{\partial f}{\partial x^i} - \Gamma^i_{\rho\sigma}p^\rho p^\sigma\frac{\partial f}{\partial p^i} \ , \tag{3.36}$$

where I have chosen that the affine parameter is the eigentime in the last equality (i.e. $\lambda = \tau$). The sum is only over spatial momenta p_i since particles are considered on-shell, and thus p^0 is not an independent variable. The sum is also only over spatial coordinated x^i because I will not consider a system where f has an explicit time-dependence. For the FRW-metric, the Liouville operator becomes

$$\hat{\mathbf{L}}[f] = E(\vec{p})\left(\partial_t - H\vec{p}\cdot\nabla_{\vec{p}}\right) f(\vec{p}) \ . \tag{3.37}$$

In order to get the evolution of the number density one has to integrate over the momentum space. This means that by use of integration by parts, the Boltzmann equation for the number density can be written in the following form

$$\dot{n} + 3Hn = g\int \mathbf{C}[f]\frac{d^3p}{(2\pi)^3E} \ . \tag{3.38}$$

Furthermore, it is useful to write the write the Boltzmann equation in terms of the dimensionless variable

$$Y \equiv \frac{n}{s} \ , \tag{3.39}$$

which is the number density per comoving volume. By taking the derivative of Y with respect to time, one finds that

$$\dot{Y}s = \dot{n} + 3Hn \ . \tag{3.40}$$

We can now see that the left hand side of Eq.(3.46) tells us about the rate at which the comoving number density changes, since the term $3Hn$ is the contribution from the expansion of the universe. The right-hand side tells us about the contribution to the change of the comoving number density by creations and annihilations of ψ. It can also be useful to use the dimensionless variable

$$x \equiv \frac{m}{T} \ , \tag{3.41}$$

as the independent variable since the interaction term will usually depend on the temperature rather than time. This means that comoving number density changes with respect to x as

$$\frac{dY}{dx} = \frac{dY}{dt}\frac{dt}{dT}\frac{dT}{dx} = \frac{1}{\overline{H}(T)}\frac{\dot{Y}}{x} \ . \tag{3.42}$$

Collision term

The collision term can be calculated using quantum field theory. For a general process of incoming particles $I = \{a, b, ...\}$ and outgoing particles $O = \{\psi, k, l, ...\}$, the collision term for one of the particles species, let's say ψ, is given by

$$\begin{aligned} g_\psi \int \mathbf{C}[f]\frac{d^3p_\psi}{(2\pi)^3 E_\psi} = \int & d\Pi_a d\Pi_b ... d\Pi_\psi d\Pi_k d\Pi_l ... \\ & \times [f_a f_b ...(1 \pm f_\psi)(1 \pm f_k)...|\mathcal{M}|^2_{I\to J} \\ & - f_\psi f_k ...(1 \pm f_a)(1 \pm f_b)...|\mathcal{M}|^2_{J\to I}] \\ & \times (2\pi)^4 \delta^4(\sum_{i\in I} p_i - \sum_{j\in O} p_j) \ , \end{aligned} \tag{3.43}$$

where the Lorentz invariant measure is

$$d\Pi_i = \frac{d^3p_i}{(2\pi)^3 2E_i} \ . \tag{3.44}$$

The factors $(1 \pm f_i)$ are quantum-statistical factors where (+) applies to bosons and are called Bose-enhancement factors, while (-) applies to fermions and are called Fermi-blocking factors. $|\mathcal{M}|^2$ is the matrix element squared summed (**not averaged**) over

the initial and final internal degrees of freedom. CP invariance is often assumed, and it implies that

$$|\mathcal{M}|^2_{I\to J} = |\mathcal{M}|^2_{J\to I} = |\mathcal{M}|^2 \ . \tag{3.45}$$

In instances where quantum statistics are negligible, e.g. when the particles are non-relativistic, one uses Maxwell-Boltzmann distribution, i.e. we can use Eq.(3.2) where E_i is the energy in the rest frame of the gas and use that the Fermi-blocking/Bose-enhancement factors equal unity $1 \pm f \simeq 1$. In the cases where quantum statistics cannot be neglected, e.g. freeze-in, one has to use the Bose-Einstein distribution for bosons and the Fermi-Dirac distribution for fermions, given by Eq.(3.1), as well as including the Fermi-blocking/Bose-enhancement factors. The Boltzmann equation takes the following form when we assume that the particles are described by Maxwell-Boltzmann distributions

$$\dot{n_\psi} + 3Hn_\psi = \int d\Pi_a d\Pi_b ... d\Pi_\psi d\Pi_k d\Pi_l ... [f_a f_b ... - f_\psi f_k f_l ...](2\pi)^4 \delta^4(\sum_{i\in I} p_i - \sum_{j\in O} p_j)|\mathcal{M}|^2 \ , \tag{3.46}$$

which is absolutely crucial in DM calculations, as we will see in section 4.4. This form of the Boltzmann equation will be used when discussing freeze-out since the Maxwell-Boltzmann approximation holds when the particles are non-relativistic. In the case of freeze-in, this is no longer always the case and as we will see in chapter 8, Eq.(3.46) will not give the correct result. Instead we have to revert to including the quantum-statistical factors and using the Fermi-Dirac and Bose-Einstein distributions. I will come back to this in section 5.2 with a much more detailed discussion.

Part II

Dark Matter

Chapter 4

Dark matter: Evidence, detection and Freeze-out

One of the biggest mysteries in modern physics is dark matter. The matter constituent that accounts for roughly 85% of the known matter in the universe. However, the only evidence we have of it is through its gravitational pull. The Planck collaboration has through its study of the CMB found that the DM relic abundance is $\Omega_c h^2 = 0.12$. We know very little about its non-gravitational properties, but this does not mean that we do not have any candidates or production mechanisms, in fact we have many.

This is what I will introduce in this chapter. I start with a brief review of the evidence we have for DM and what constraints it sets on its particle(s). I will then in section 4.2, give some examples of dark matter candidates that are well studied. In section 4.3, I present the various detection methods used in the hunt for dark matter: direct detection, indirect detection and collider searches, together with the present constraints. I also present a brief review of the effects of self-interacting dark matter and the small-scale problems of ΛCDM. Finally, in section 4.4, I present the most popular dark matter production mechanism, namely the *Freeze-out* mechanism.

4.1 Evidence and constraints

We can infer the existence of DM on scales from Dwarf galaxies to cosmological scales, but there is very limited knowledge about the properties of the dark matter particle(s). The first observation of dark matter was in 1933 by Fritz Zwicky when he studied the Coma Cluster. He found that the mass needed to explain the radial velocity dispersion of stars was much more than the observed mass [10]. This led him to coin the excess matter as *dunkle Materie* ("Dark Matter"). The same discrepancy was also found in other clusters [11]. The dark matter paradigm has only been strengthened by evidence

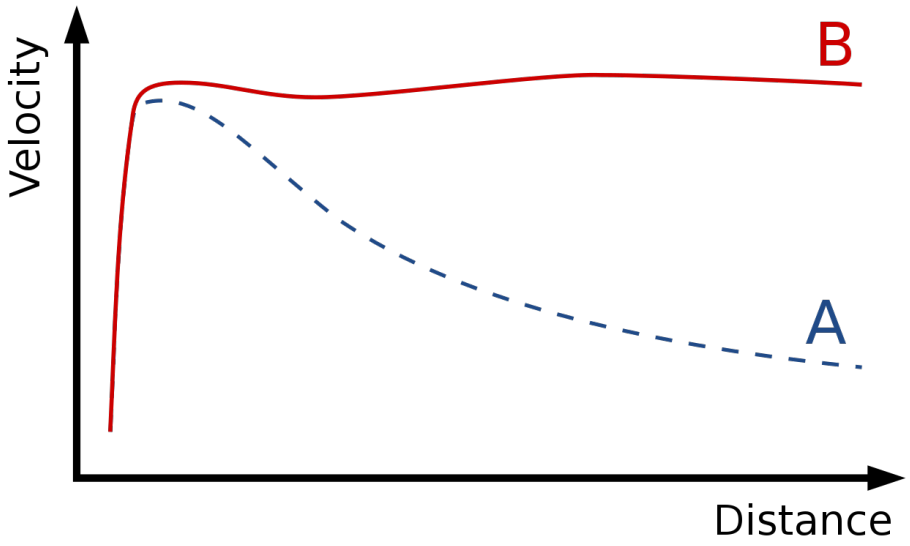

Figure 4.1: Schematic drawing of the expected rotation curve of a typical spiral galaxy where **A** is the curve predicted from the observed matter, the observed rotation curve is **B** which can be explained by DM. Image taken from wikimedia.org/wiki/File:GalacticRotation2.svg.

coming from:

- **Rotation curves of spiral galaxies:** The work of Vera Rubin and Kent Ford, which was done decades after Zwicky's first observation, found one of the most striking evidence of DM. They looked at the rotation curves for spiral galaxies [12, 13]. This is the orbital velocities of stars as a function of their radial velocity. The orbital velocity of a star at a distance r from the centre of a galaxy using Newtonian gravity is given by

$$v_{\mathrm{c}}(r) = \sqrt{\frac{GM(r)}{r}} \,, \tag{4.1}$$

  where $M(r)$ is the enclosed mass. This means that at distances larger than the galactic disc, which is where the majority of visible mass is, the orbital velocity should fall as $v_{\mathrm{c}} \propto r^{-\frac{1}{2}}$. This is not what is observed, instead they found that the velocity of the stars in the region outside of the galactic disc stayed constant. This indicates that the mass must increase outside of the galactic disc, which means that some other matter component is needed. This is illustrated in figure 4.1. It is worth noting that modified theories of gravity can also explain this [14]. However, modified models of gravity cannot explain all the observation with a single number. This is one of the strengths of the ΛCDM. Nowadays, rotation curves are considered more as historical evidence because the cosmological evidence is much cleaner and more robust.

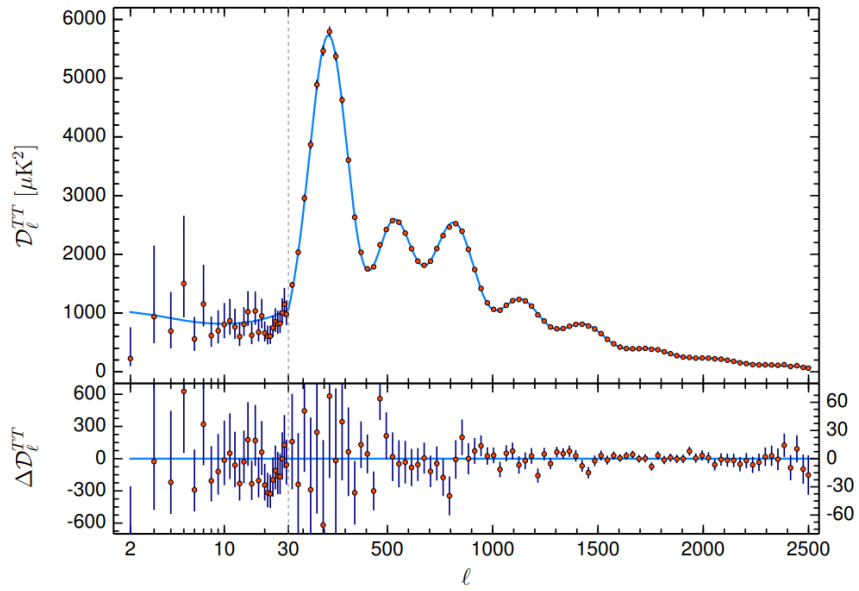

Figure 4.2: CMB Power spectra as measured by *Planck 2018 results. VI. Cosmological parameters*. Figure taken from [1].

- **Anisotropies in the Cosmic microwave background (CMB):** The CMB was accidentally discovered by Arno Penzias and Robert Wilson in 1964 [15] as they worked with the Holmdel Horn Antenna, which earned them the 1978 Nobel prize in physics. The relic radiation is one of the most important observations in cosmology, and an important source of evidence for dark matter. The structure of the CMB power spectra, see figure 4.2, is dependent on the total matter to radiation ratio: the pressure due to the photons pushes baryonic matter out of gravitational wells, which erases anisotropies in the spectra, whereas the gravitational effect from baryons and DM will increase the anisotropies. This results in acoustic oscillations, where the oscillations are dependent on the matter content of the universe, thus dependent on the DM density. It is these anisotropies that the famous Wilkinson Microwave Anisotropy Probe (WMAP) [16] and Planck observatory [1] studied. They confirmed that the universe has a 26% content of dark matter, and the current quoted value for the DM relic density is given by the Planck collaboration, which is $\Omega_c h^2 = 0.1200 \pm 0.0012$.

- **Gravitational lensing:** From general relativity we know that any matter distribution bends light along its path. A distribution of matter which bends the light coming from a distant source to an observer is called a *gravitational lens*. When the distortion is easily visible, e.g. Einstein rings, we call the lensing *strong lensing*. The lensing is much smaller in the case of dark matter, which is why we call this lensing *weak lensing*. The only way this can be detected, is by using statistical methods to analyse a large number of sources. The way the

Figure 4.3: Composite image of the Bullet cluster where the background image shows the visible spectrum of light stemming from the Magellan and Hubble Space Telescope images. The pink overlay shows the X-ray emission of the colliding clusters, which was recorded by the Chandra Telescope. The blue overlay shows the mass distribution of the clusters calculated from gravitational lens effects. Image taken from chandra.harvard.edu.

lensing shows up is in a coherent weak distortion pattern on the faint and distant galaxies. A typical galaxy cluster usually has a virial region which covers 10^3 galaxies [17]. The intrinsic ellipticities of individual galaxies cannot be inferred, but by looking at a few galaxies one should find that the intrinsic ellipticities should average to zero. This means that the observed ellipticity is caused by the gravitational lensing, which results in a shear that is used to reconstruct the mass distribution, particularly the dark matter distribution. This has been done for the **Bullet cluster** (1E0657-558) by D. Clowe et al. [18] which is shown in figure 4.3. This cluster was formed by the collision of two large clusters of galaxies. The pink region shows hot gas which contains most of the baryonic matter, while the blue region shows where one finds most matter due to gravitational lensing. From this observation we can see that most of the matter in the cluster is dark. Another observation from this is that dark matter cannot interact strongly with itself. The baryonic matter is slowed down by drag; this we can see does not happen with the DM since the blue areas are beyond the pink areas. Finally, this evidence cannot be explained by modified theories of gravity if hot gas is assumed to be the most massive component in the clusters; dark matter is required.

- **Structure formation in the early universe:** One of the strongest evidences

for the existence of cold dark matter comes from the fact that large scale structure formation has happened. Since dark matter only interacts through gravity, it will collapse into complex networks of halos a lot earlier than ordinary matter will. This is because the pressure from interactions delays structure formation in ordinary matter, which means DM has to be non-baryonic. It is important that dark matter is non-relativistic (cold), because if it was relativistic, such as the case for neutrinos, they will not collapse into halos. If the dark matter halos did not exist, we would have that the epoch of galaxy formation would occur later than is observed [19]. Furthermore, N-body simulations using cold DM, such as M. Boylan-Kolchin et al. with the Millennium-II [20], appear to agree with observations. They find the well-known cosmic web of filaments and voids, which is essential in the formation of galaxy groups, clusters, and superclusters. However, they find a higher abundance of small halos than is observed, this is the well-known *missing satellite problem*, which I will discuss in section 4.3.4.

Even though there is, as we have seen, a lot of evidence and knowledge about the gravitational effects of DM, we still haven't found any definite evidence coming from detection experiments; this will be discussed in section 4.3. From the evidence we have and from knowledge of cosmological processes we have some strong constraints on its properties. We know it is some long lived non-baryonic matter component, since if it was baryonic, it would not collapse into halos fast enough to describe the observed structure of the universe. Its abundance is about five times as large as the abundance of ordinary matter. The best measurement of the relic density was done by the Planck collaboration, they found the abundance to the staggering accuracy $\Omega_{\mathrm{c}}h^2 = 0.1200 \pm 0.0012$ [1]. We know that it cannot be luminous, which means that its coupling to U_{em} and $SU(3)_{\mathrm{c}}$ must be extremely small. It must also be cold to account for structure formation in the early universe. There are many hypothesized particles that have all these features, I will now outline some of them.

4.2 Dark matter candidates

Even though we have no knowledge about what particle(s) DM is, this has not stopped physicists from theorising what the particle(s) can be. For a particle species to be a good DM candidate, it has to fit the constraints set on the features of DM by observations. A good way to check if a particle species is a good candidate is to apply the 10-point test presented in Ref. [21], which tells us that a particle can be considered a good DM candidate if it satisfies the following ten points:

1. It gives the appropriate relic density.
2. It is cold.

3. It is neutral.
4. It is consistent with Big Bang nucleosynthesis (BBN).
5. It leaves stellar evolution unchanged.
6. It is compatible with constraints on self-interactions.
7. It is consistent with direct DM searches.
8. It is compatible with gamma-ray constraints.
9. It is compatible with other astrophysical bounds.
10. It can be probed experimentally.

I will now discuss some candidates that satisfy these ten points.

The **Axion** [22] is one of the prime candidates that satisfies these points. It was hypothesized in 1977 to solve the strong CP problem in QCD, which it does by the Peccei–Quinn mechanism. If its mass is above $m_e/10^{11}$ where m_e is the electron mass, then the misalignment mechanism can generate a population of cold axions which can account for the observed dark matter [23, 24].

Another dark matter candidate is the **sterile neutrino** [25]. The SM neutrinos are in principle a very natural DM candidate, but due to their low mass and coupling to the other particles, they cannot account for the observed dark matter. Sterile neutrinos on the other hand can [26]. They are also well motivated, by the fact that all other fermions have been observed with both left and right handed chirality, and they would provide a very simple explanation for the low masses of the SM neutrinos and the neutrino oscillations via the seesaw mechanism.

Supersymmetric particles such as the neutralinos and the gravitino are also viable DM candidates. The lightest neutralino as the lightest supersymmetric particle (LSP) in the Minimal Supersymmetric Standard Model (MSSM) assuming R-parity, is one of the most studied DM candidates; it is what is called a weakly interacting massive particle (WIMP) [27]. I will explain further down how WIMPs are DM candidates. The gravitino, which is the supersymmetric partner to the graviton in supergravity theories, can also be a viable DM candidate if certain conditions hold, it is what is called a Feebly Interacting Massive Particle (FIMP), which also will be explained further down. For constraints on light gravitinos see Ref. [28] and for a minimal model of gravitino DM see Ref. [29].

A viable DM candidate that is not some form of elementary particle is primordial black holes. They may have been produced by various mechanisms during the early universe. Due to Hawking radiation we know that they have to have been bigger than 10^{15} g. For a review of primordial black holes as dark matter see Ref. [30].

WIMPs such as neutralinos, which are believed to have couplings and masses that are reminiscent to that of the weak scale, have been by far the most popular DM candidates. The fact that a WIMP with an electroweak mass and coupling gives the correct relic abundance is the celebrated *WIMP miracle*. It is worth noting that by increasing the mass and decreasing the coupling one can obtain the correct abundance as well. It is believed that WIMPs have been thermally created in the early universe and *freeze out* when they become non-relativistic, this mechanism will be explained in section 4.4.

The last candidate I will discuss is FIMPs. They have such feeble couplings that, unlike WIMPs, they were never in thermal equilibrium with the visible sector. The DM abundance will then be generated by the *freeze-in* mechanism. This will be discussed in section 5. Examples of other FIMP candidates are a scalar or a vector particle with couplings in the range $O(10^{-7})$ or less, depending on its mass [31], the gravitino and sterile neutrinos, which have become a popular FIMP candidate since the Dodelson-Widrow mechanism [32] has been ruled out as the production process [33, 34].

4.3 Detection methods

To test for non-gravitational properties of DM, we have to utilize different search avenues. Some detection methods that are used are shown in figure 4.4. Direct detection looks at, for instance, the scattering of DM with a nucleus here on earth. Indirect detection looks at the decay/annihilation products coming from areas with high density of DM. While collider searches, such as at the LHC, search for either missing transverse energies or measure decay widths of particles that could couple to DM. A rather recent addition to these search avenues is to look at the effects of self-interactions [35]. I will outline these search avenues below.

4.3.1 Direct detection

The DM flux on the earth is of the order 10^5 $(100\ \mathrm{GeV}/m_\chi)\,\mathrm{cm}^{-2}\,\mathrm{s}^{-1}$ [37], if the Milky Way's DM halo is composed of WIMPs. Even though the coupling between the SM and WIMP is small, the size of the flux means that there will be a potentially measurable number of WIMPs scattering off nuclei, which subsequently translates to detection of light, charge, or heat, produced from the collision. The big problem one faces with this method is the fact that the energies deposited at each collision and the interaction rate will be very small. This means that one must be very wary of the background radiation. Therefore, the experiments are conducted underground, usually in mines or tunnels in mountains to shield from cosmic rays. What we want to measure is the rate of nuclear recoil events, or rather the differential recoil rate which often is expressed in units of events/(unit mass of detector)/(keV of recoil energy)/day, usually called the

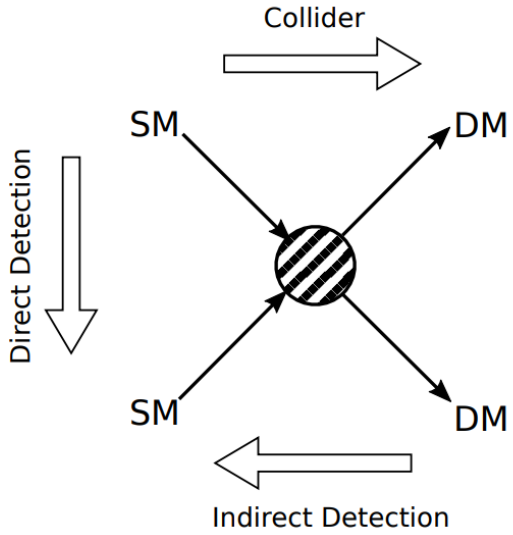

Figure 4.4: Schematic illustration of some of the detection methods used to look for dark matter. Figure taken from [36].

differential rate unit (dru) [7]

$$\frac{dR}{dE_R} = \sum_T C_T \frac{\rho_\chi^0}{m_T m_\chi} \int_{v>v_{\min}} \frac{d\sigma_{\chi T}}{dE_R} \frac{f(\mathbf{v},t)}{v} d^3v \ , \tag{4.2}$$

where E_R is the recoil energy. The sum runs over each target nuclide in the detector, C_T is the mass fraction of a nuclear species T in the detector, hence the number of targets T per unit mass of the detector is C_T/m_T. $\mathbf{v}$ is the DM velocity relative to the detector and $v = |\mathbf{v}|$. The local DM density is ρ_0^χ, and $f(\mathbf{v},t)$ is the three-dimensional DM velocity distribution with respect to Earth. These quantities depend on which dark halo model is used. $v_{\min} = \sqrt{m_T E_R / 2\mu_{\chi T}^2}$ is the minimum velocity a DM particle must have in order to give to a target T a recoil energy E_R, where $\mu_{\chi T} = m_\chi m_T/(m_\chi + m_T)$ is the reduced DM–target mass. Lastly, $\frac{d\sigma_{\chi T}}{dE_R}$ is the differential scattering cross section of a DM particle scattering of a target nucleus, this quantity is highly model dependent. These discussions usually assume that the DM is a WIMP, but as was shown in [38], direct detection can be a viable detection method for FIMPs if the mediator between the visible sector and dark sector is of mass less than a few MeV. This is because the elastic FIMP-nuclei collision will proceed through the t-channel, which means that the FIMP-nuclei cross-section can be enhanced enough to compensate for the low coupling. It is important to note that the small coupling of FIMPs makes direct detection experiments extremely difficult unless the mediator is light. Since WIMPs must be non-relativistic, the limit $v \to 0$ applies when calculating cross sections (unless the mediator is light, then the v dependence is important). The WIMP-nucleus cross section can be decomposed into two contributions: the spin-independent (SI) cross section, which dominates if the WIMP-nucleus interactions are

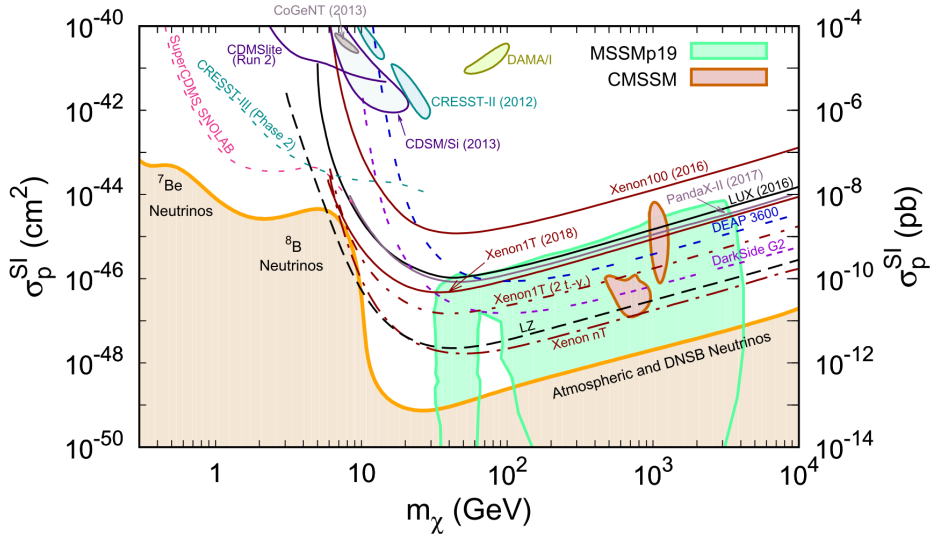

Figure 4.5: Current and future limits of the direct detection SI cross section as a function of the WIMP mass. The area faded in orange is the irreducible neutrino background. For more info regarding the experiments in the plots, refer to [2] and the articles therein.

scalar or vector, and spin-dependent (SD) cross section, which becomes important if the interaction is pseudo-scalar or axial vector

$$\frac{d\sigma_{\chi T}}{dE_R} = \left(\frac{d\sigma_{\chi T}}{dE_R}\right)_{\text{SI}} + \left(\frac{d\sigma_{\chi T}}{dE_R}\right)_{\text{SD}} \quad . \tag{4.3}$$

In practice this means $\sigma_0 F^2(E_R) \simeq \sigma^{SI} F^2_{SI}(E_R) + \sigma^{SD} F^2_{SD}(E_R)$, where σ^{SI} and σ^{SD} are the cross sections given at zero momentum transfer. The spin-independent contribution in enhanced by the square of the number of nucleons in the target nuclei (A^2), while the spin-dependent contribution is dependent on the nuclear angular momentum [37]. The momentum dependence is in the form factors F_{SI} and F_{SD}; they account for the coherence loss, which for heavy nucleons or WIMPs leads to a suppression of the event rate. The spin-independent form factor can qualitatively be understood to be the Fourier transformation of the nucleon density [37]

$$F^2_{\text{SI}}(q) = \left(\frac{3j_1(qR_1)}{qR_1}\right)^2 + \exp[-q^2 s^2] \ , \tag{4.4}$$

where $q = \sqrt{2m_T E_R}$ is the momentum transfer, j_n is the spherical Bessel functions, $s \simeq 1$ fm gives a measure of the nuclear skin thickness and $R_1 = \sqrt{R^2 - 5s^2}$ where $R \simeq 1.2A^{1/2}$ fm. The form factor is normalized by $F^2_{\text{SI}}(0) = 1$. For the spin-dependent contribution, the form factor is parameterised by parameters that are determined experimentally. In general, one has to take into account both the spin-independent and spin-dependent contributions, but in the case of heavy targets ($A > 20$) the spin-independent contribution will dominate. Most experiments use heavy targets, but there

exist experiments that are sensitive to the SD WIMP coupling as well, where they use targets with a large nuclear angular momentum [37]. The results coming from direct detection experiments have not been conclusive. A model independent experiment which has reported a DM signal is the DAMA/LIBRA experiment [39]. They use scintillating crystals to detect light signals from DM-nucleus scattering. However, these results are in strong tension with the null results coming from XENON1T [40], LUX [41] and the PandaX-II experiment [42]. In the low mass range detectors such as superCDMS [43] and SENSEI [44] use arrays of semiconductors to search for electron recoils produced by inelastic scattering of WIMPs. A plot of current and future limits for the spin independent cross section as a function of the WIMP mass for direct detection experiments are shown in figure 4.5. The null results coming from these searches have made other DM paradigms garner more interest, and FIMPs naturally explains the null result due to their small coupling.

4.3.2 Indirect detection

Indirect detection experiments look for DM annihilation or decay products, mainly photons, electrons, positrons, antiprotons, and antideuterons. Out of all the annihilation products, photons and neutrinos are the easiest to look for. This is because they travel through space undisturbed, which gives clear spectral signatures. For γ-rays, the differential DM-induced flux averaged over the opening angle $\Delta\psi$ of the detector is given by [45]

$$\frac{d\Phi_\gamma}{dE_\gamma}(E_\gamma,\psi) = \underbrace{\frac{1}{2}\frac{\langle\sigma v\rangle}{4\pi m_\chi^2}\sum_f \mathrm{Br}_f \frac{dN_\gamma^f}{dE_\gamma}}_{P} \times \underbrace{\int_{\Delta\psi}\frac{d\Omega}{\Delta\psi}\int_{\mathrm{l.o.s.}} dl(\psi)\rho^2(\mathbf{r})}_{J} , \tag{4.5}$$

where N_γ^f is the number of photons per annihilation for a channel f, ψ is the direction of the gamma-ray flux and the $\rho(\mathbf{r})$ is the DM distribution, which is integrated over the line of sight (l.o.s.) l. We can see that the differential flux factorizes into a particle physics factor P which is determined by the particle properties and an astrophysical factor J which accounts for the dark matter distribution along the line of sight. A striking signature coming from DM-annihilation into two-body final states containing a photon, this would make monochromatic γ-ray lines. The problem with these processes is that they are loop suppressed, which makes these lines very hard to look for, but there are examples where a strong line exists [46]. The only products coming from annihilation of WIMPs at three-level are pairs of quarks, leptons, gauge bosons, and Higgs. This means that we have to measure *secondary photons* which comes from further decays and hadronization. The resulting energy spectrum will be continuous and can be calculated using programs such as *Pythia* [47]. These energy spectra can then be used to look for new physics. For a comprehensive review see [48] or [49]. Photons coming from internal bremsstrahlung may add a very sharp cutoff in the energy spectrum at $E_\gamma = m_\chi$ or bump-like features at $E_\gamma \lesssim m_\chi$ [45].

From Eq.(4.5) we see that the best places to look at are where the factor J is big. The Milky Way Galactic Centre is therefore a good place to look at. Here there is found an excess of gamma rays in the GeV energy range [50, 51]. Multiple explanations have been put forwards, from astrophysical processes [52–54], to DM annihilation's, e.g. the data is consistent with a DM candidate of mass less than 100 GeV annihilating into quarks [49]. A popular explanation is that the excess is a result of a population of faint, unresolved point sources. As with all photon detection experiments background radiation is a challenge, which means that one has to have good modelling of the background. Dwarf galaxies has a smaller J factor, but with highly sensitive detectors they are also a good place to look. These searches strongly constrain the DM explanation of the Galactic centre [55, 56]. Another important observation is the 3.55 keV emission line from X-ray images taken by the XMM-Newton telescope [57, 58] of 73 galaxy clusters [59]. Even though this line is highly controversial, the DM interpretation is not ruled out.

As mentioned above, indirect detection experiments can also look for decay products other than photons. The AMS-02 experiment aboard the international space station reports an excess of the ratio of antiproton to proton fluxes [60]. This can be explained by DM annihilations, see e.g. Ref. [61], but this data can also be accounted for by systematic errors and secondary astrophysical processes [62]. Another important observation is the excess of the high-energy positron abundance (energy range of 1.5-100 GeV) found by the PAMELA experiment [63], and later confirmed by FERMI [64] and AMS-02 [65]. Even though astrophysical explanations such as pulsars [66] and supernovae remnants [67] can explain this observation, DM annihilations have not been excluded and can be involved [68].

4.3.3 Collider searches

To get observable signatures at colliders, the SM and DM interaction strength has to be sufficiently strong, which is why WIMPs are the DM candidates that have been searched the most for. There are two main methods colliders search for DM: missing transverse energy searches and precise measurement of specific SM branching ratios or decay widths. Weakly interacting and neutral particles, such as neutrinos and DM, escape from the collider detectors immediately without interacting. In order to infer the presence of such particles, one must look at the resulting imbalance in the total momentum. This is done by looking at the missing transverse energy, which is defined as

$$\not{E}_{\mathrm{T}} = \left| \sum_f \vec{p}_{\mathrm{T}} \right| \tag{4.6}$$

where $\vec{p}_{\mathrm{T}}$ is the transverse momentum, and the sum is over all visible final states, this is shown in figure 4.6. The $\not{E}$ signal is then studied carefully, since the $\not{E}$ signal is very sensitive to particle misidentification, particle momentum mismeasurements, and

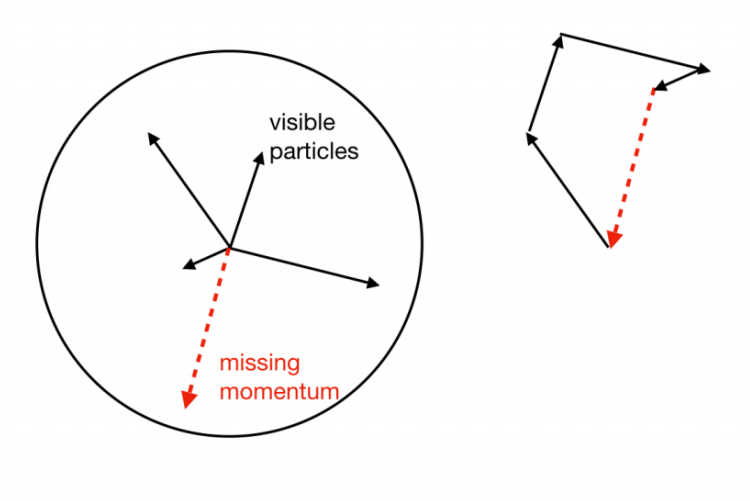

Figure 4.6: Schematic drawing of the transverse plane of the detector. Black arrows represent visible particles and the red arrow represent the missing momentum due to invisible particles. Figure taken from [36].

cosmic-ray particles, which can result in artificial $\not{E}$ [36, 69].

Another way of looking for DM in colliders is by precisely measuring the decay widths of gauge bosons or the SM Higgs boson. If the DM mass is less than half of the Z boson mass, then we can place limits on its mass and coupling from the Z boson decay width. The same can be done with Higgs branching ratios if the DM mass is less than half of the Higgs mass. There are multiple ways of looking for invisible Higgs boson decays. One can directly search for them by looking at the production modes shown in figure 4.7. i.e. Vector boson fusion (VBF) via $qq \to qqH$, production in association with a massive vector boson ($qq \to VH$, where $V = Z, W$) and gluon fusion accompanied by jet from initial state radiation. Recently, a combination of searches for invisible Higgs decays at the LHC have found that BR($h \to$ inv) < 0.11 [70].

Using effective field theory is one way to get model independent constraints on DM properties. An example would be a vector mediator with mass $m_V = \Lambda^2/(g_\chi g_q)$ whose low energy operator reduces to $\frac{1}{\Lambda^2}\bar{\chi}\gamma^\mu\chi\bar{q}\gamma_\mu q$, which couples q to χ with coupling g_q and g_χ respectively. A problem with this method is that it assumes a large mediator mass, there has therefore been a lot of focus on simplified models with mediators connecting the dark sector to the SM. In these models it is important to consider the mediator propagator, since this can affect kinematical characteristics of the interaction, unlike the effective field theory method where the mediator is integrated out. The mediator might also decay into final states other than two DM particles. Thirdly, the existence of such a mediator can change the constraints set by colliders and/or cosmological observations [31].

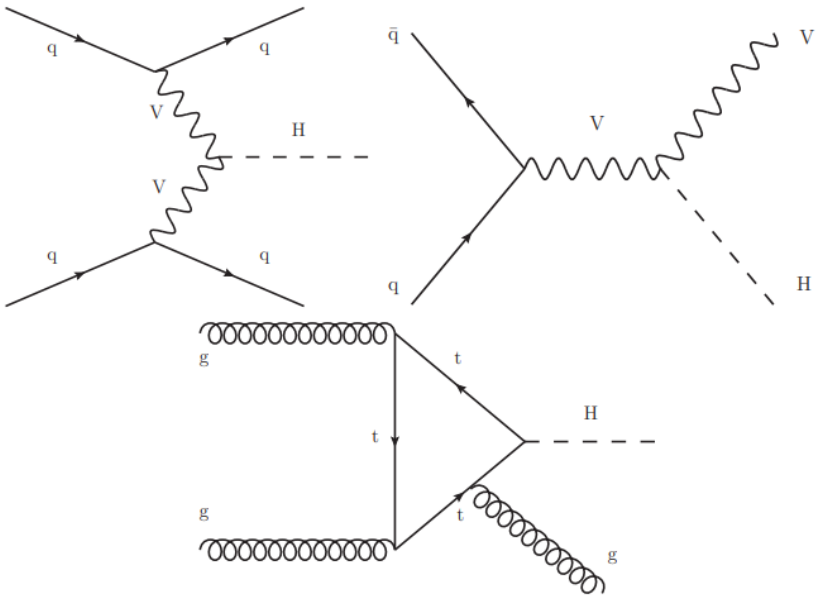

Figure 4.7: Feynman diagrams for the three production processes targeted in searches for invisible Higgs boson decays. (Upper left) Vector boson fusion: $qq \to qqH$, (upper right) VH: $q\bar{q} \to VH$, and (bottom) gluon fusion: $gg \to gH$ [71].

4.3.4 Self-interacting dark matter

The study of self-interacting DM (SIDM) is a vast subject. I will only scratch the surface of this topic in this section. For a more comprehensive review see Ref. [35]. The ΛCDM model which models DM as a cold collisionless fluid has been remarkably successful at large scales [1], but at smaller scales the model is less tested and certain inconsistencies exist [72]. A modification of ΛCDM that can fix these inconsistencies is SIDM. There is no phenomenological reason as to why DM self-interactions cannot become as strong as the interaction between nucleons [73], which along with the fact that SIDM can have an impact on structure formation has increased the interest in SIDM. The *small-scale problems* [72–74] of ΛCDM which are talked most about in the literature are the "core-cusp" [75], "too big to fail" [76], "diversity" [77], and the "missing satellite" [78] problems. The **core-cusp problem** is the fact that the expected DM density profiles of dwarf galaxies coming from cosmological N-body simulations follows a steep power-law-like behaviour in the inner part of the galaxy, i.e., *cuspy* profile, while a constant distribution is observed in some objects, called *cores* [75, 79–81], see the right panel of figure 4.8. This means that the expected orbital velocity close to the centre of the galaxy is less than is expected in the rotation curves of dwarf galaxies, see the left panel of figure 4.8. The **too big to fail** problem is that cosmological simulations of ΛCDM predicts that the majority of DM sub-halos around the Milky Way are too dense to host its brightest satellites [76, 85, 86]. The **diversity** problem comes from the observation that there is a big diversity in the shape

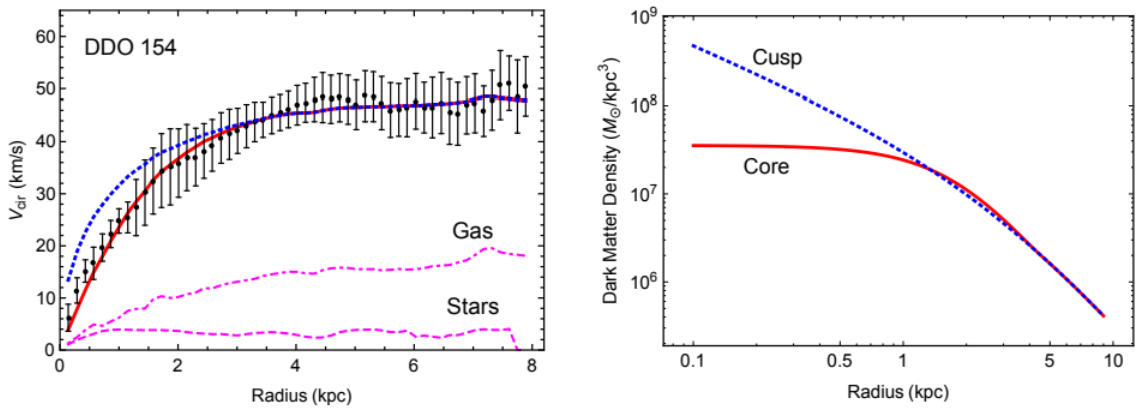

Figure 4.8: Black data points show the observed rotation curve of dwarf galaxy DDO 154 [82], The Navarro–Frenk–White (NFW) profile is the dotted blue, and cored profile is solid red. The stellar (gas) contributions are indicated by pink (dot-)dashed lines. Right: The NFW profile versus the density profile generated using analytical SIDM halo model developed in [83, 84]. Image taken from [74].

of rotation curves of dwarf galaxies, which is at odds with the rotation curves predicted by ΛCDM [77, 87]. The **missing satellite** problem is, as mentioned earlier, the fact that numerical simulations predict a bigger number of small Milky way satellites than is observed [78, 88]. It has been proposed that carefully addressing for effects of baryonic physics can solve these problems [89, 90], however they are unlikely to resolve these problems with standard WIMPs. The next possibility is then that the ΛCDM must be modified, such modifications include decaying [91], warm [92, 93] and SIDM [74]. In the case of SIDM, the fact that the mean free path for the DM particles is a lot smaller will only alter the evolution where the density inhomogeneities are large. This means that the large-scale features are unchanged. The small-scale problems, however, can be alleviated if $0.1 \lesssim \sigma/m \lesssim 10$ cm^2/g [94, 95], where σ is the self-scattering cross section and m is the DM particle mass. From looking at "bullet clusters collisions" one gets the constraint $\sigma/m < 1.25$ cm^2/g at 68% CL [96], while the most recent cluster collision observations give the constraint $\sigma/m < 0.47$ cm^2/g at 95% CL, although this result has been questioned recently [97, 98]. The reason SIDM solves the "core-cusp" and "too big to fail" problem is due to the heat transfer that happens because of the self-scattering of DM particles. Such energy transport will lead to a core collapse for the DM halo and it also changes the subhalo abundance [99]. The "missing satellite" problem can also be alleviated by SIDM [100] and by including warm or decaying DM [91–93].

4.4 Freeze-out

I will now review the most studied DM production mechanism, *freeze-out*. It is worth noting that it is not just WIMPs that freeze-out. The standard model neutrinos experienced freeze-out when the temperature $T \gtrsim$ few MeV [4], but at this temperature the neutrinos were still relativistic, which is why they are called a *hot relic*.

This mechanism is based on the assumption that DM reaches thermal equilibrium with the visible sector at early times. I will look at the simplest case where there is no asymmetry between particles and anti-particles. In this case one can solve for the abundance by looking at the creation and annihilation processes between DM and SM. I start by looking at the specific $(2 \to 2)$ channel $\chi\bar{\chi} \leftrightarrow X\bar{X}$ of a particle χ which represents the DM particle, with a SM particle X. It will be clear why decay processes $(1 \to 2)$ are negligible in later discussions. The assumptions we make are [101]

- Phase-space distributions are approximated by Maxwell-Boltzmann distributions, which is a good approximation for $T \lesssim 3m_\chi$. This means that quantum statistical factors can be neglected.
- The WIMPs are in thermal equilibrium.
- The WIMPs remain in kinetic equilibrium after decoupling.
- The initial chemical potential is negligible.

Since χ is assumed to be in thermal equilibrium with X until it is non-relativistic, we can approximate f_χ by using the Maxwell-Boltzmann distribution. Due to energy conservation and the principle of detailed balance, we can rewrite the Standard model terms $f_X f_{\bar{X}}$ in terms of the equilibrium terms of f_χ and $f_{\bar{\chi}}$

$$f_X f_{\bar{X}} = \exp[-(E_X + E_{\bar{X}})/T] = \exp[-(E_\chi + E_{\bar{\chi}})/T] = f_\chi^{\text{eq}} f_{\bar{\chi}}^{\text{eq}} \ . \tag{4.7}$$

The Bose-Enhancement and Fermi-blocking factors can be neglected when $T \ll E_i$, meaning that $1 \pm f_X \sim 1$. Since we have only one channel, the right hand side of the Boltzmann equation for the number density, Eq.(3.46), becomes

$$\begin{aligned} g_\chi \int \mathbf{C}[f_\chi] \frac{d^3p_\chi}{(2\pi)^3} = -\int & [f_\chi f_{\bar{\chi}} - (f_\chi^{\text{eq}})(f_{\bar{\chi}}^{\text{eq}})] \\ & (2\pi)^4 \delta(p_\chi + p_{\bar{\chi}} - p_X - p_{\bar{X}}) |\mathcal{M}|^2 \\ & \frac{d^3p_\chi}{(2\pi)^3 2E_\chi} \frac{d^3p_{\bar{\chi}}}{(2\pi)^3 2E_{\bar{\chi}}} \frac{d^3p_X}{(2\pi)^3 2E_X} \frac{d^3p_{\bar{X}}}{(2\pi)^3 2E_{\bar{X}}} \ , \end{aligned} \tag{4.8}$$

We should note that there should not appear additional factors of $\frac{1}{2}$ in the case where χ and $\bar{\chi}$ are identical: a factor $\frac{1}{2}$ appears to avoid double counting but is cancelled

due to the fact that two particles disappear in each annihilation. We only need the integrated $\mathbf{C}[f_\chi]$, which is why I have not given expression for $\mathbf{C}[f_\chi]$. We can now use the usual definition of the cross section on the final state integrals [102, p.106]

$$4F\sigma_{\chi\bar{\chi}\to X\bar{X}} = \int \overline{|\mathcal{M}|}^2 (2\pi)^4 \delta(p_\chi + p_{\bar{\chi}} - p_X - p_{\bar{X}}) \frac{d^3p_X}{(2\pi)^3 2E_X} \frac{d^3p_{\bar{X}}}{(2\pi)^3 2E_{\bar{X}}} \ , \tag{4.9}$$

where $F = \sqrt{(p_\chi \cdot p_{\bar{\chi}})^2 - m_\chi^2 m_{\bar{\chi}}^2}$ and $\overline{|\mathcal{M}|}^2$ denotes the usual spin-averaged matrix element

$$\overline{|\mathcal{M}|}^2 = \frac{|\mathcal{M}|^2}{g_\chi g_{\bar{\chi}}} \ . \tag{4.10}$$

It is now clear how to include all channels; one replaces $\sigma_{\chi\bar{\chi}\to X\bar{X}}$ by

$$\sigma = \sum_{\text{all}f} \sigma_{\chi\bar{\chi}\to f} \ . \tag{4.11}$$

This means that we get the following Boltzmann equation for the number density

$$\dot{n}_\chi + 3Hn_\chi = -\langle \sigma v_{\text{Møl}} \rangle (n_\chi^2 - (n_\chi^{\text{eq}})^2) \ , \tag{4.12}$$

where we use the Maxwell-Boltzmann distribution [101]

$$n_\chi^{\text{eq}} = g_\chi m_\chi^2 T K_2(m_\chi/T)/(2\pi^2) \ , \tag{4.13}$$

where K_i is the modified Bessel function of the second kind of order i, defined by

$$K_n(z) = \frac{\sqrt{\pi}}{(n-\frac{1}{2})!} \left(\frac{1}{2}z\right)^n \int_1^\infty (x^2-1)^{n-1/2} e^{-xz} dx \ . \tag{4.14}$$

The thermally averaged cross section times velocity is

$$\langle \sigma v_{\text{Møl}} \rangle = \frac{\int \sigma v_{\text{Møl}} e^{-E_\chi/T} e^{-E_{\bar{\chi}}/T} d^3p_\chi d^3p_{\bar{\chi}}}{\int e^{-E_\chi/T} e^{-E_{\bar{\chi}}/T} d^3p_\chi d^3p_{\bar{\chi}}} \ , \tag{4.15}$$

where the Møller velocity is $v_{\text{Møl}} \equiv F/E_\chi E_{\bar{\chi}}$, E_χ and $E_{\bar{\chi}}$ are the energies of the colliding particles in the cosmic rest frame. In the case where there are other particles close in mass to χ, they will be present at the time when χ freeze-out and will contribute to the abundance. This is called co-annihilations [103] and the Boltzmann-equation will have the same form as Eq.(4.12), but with $n_\chi \to n = n_\chi + \sum_i n_i$ where i is the particle-species close in mass to χ that also freeze-out, such that $m_i < m_j$, when $i < j$. This is the relevant quantity because the heavier particles will eventually decay into χ.

In order to find the expression for $\langle \sigma v_{\text{Møl}} \rangle$ I will be following the standard treatment, as established by Gondolo & Gelmini [101]. Note that a similar approach will be used for the full distributions in section 5.2. We begin by writing the momentum-space volume element as

$$d^3p_\chi d^3p_{\bar{\chi}} = 4\pi |\vec{p_\chi}| dE_\chi 4\pi |\vec{p_{\bar{\chi}}}| dE_{\bar{\chi}} \frac{1}{2} d\cos\theta \ , \tag{4.16}$$

where θ is the angle between $\vec{p_\chi}$ and $\vec{p_{\bar{\chi}}}$. Now we change variables from E_χ, $E_{\bar{\chi}}$, θ to E_+, E_-, s given by

$$E_+ = E_\chi + E_{\bar{\chi}} \ , \quad E_- = E_\chi - E_{\bar{\chi}} \ , \quad s = 2m_\chi^2 + 2E_\chi \ .E_{\bar{\chi}} - 2|\vec{p_\chi}||\vec{p_{\bar{\chi}}}|\cos\theta. \tag{4.17}$$

The volume element becomes

$$d^3p_\chi d^3p_{\bar{\chi}} = 2\pi^2 E_\chi E_{\bar{\chi}} dE_+ dE_- ds \ , \tag{4.18}$$

with integration regions

$$|E_-| \leq \sqrt{1 - \frac{4m_\chi^2}{s}}\sqrt{E_+^2 - s} \ , \quad E_+ \geq \sqrt{s} \ , \quad s \geq 4m_\chi^2 \ . \tag{4.19}$$

We can now rewrite the numerator in Eq.(4.15) as follows

$$\begin{aligned}\int \sigma v_{\text{Møl}} e^{-E_\chi/T} e^{-E_{\bar{\chi}}/T} d^3p_\chi d^3p_{\bar{\chi}} &= 2\pi^2 \int dE_+ dE_- ds \ \sigma v_{\text{Møl}} E_\chi E_{\bar{\chi}} e^{-E_+/T} \\ &= 4\pi^2 \int ds \ \sigma F \sqrt{1 - \frac{4m_\chi^2}{s}} \int dE_+ e^{-E_+/T} \sqrt{E_+^2 - s} \\ &= 2\pi^2 T \int ds \ \sigma (s - 4m_\chi^2)\sqrt{s} K_1(\sqrt{s}/T) \ ,\end{aligned} \tag{4.20}$$

where it is used that in the CMS frame $\sigma F = \sigma v_{\text{Møl}} E_\chi E_{\bar{\chi}}$ is solely a function of s, and that $F = \frac{1}{2}\sqrt{s(s - 4m_\chi^2)}$. Similarly, we get the result

$$\int e^{-E_\chi/T} e^{-E_{\bar{\chi}}/T} d^3p_\chi d^3p_{\bar{\chi}} = \left[4\pi m_\chi^2 T K_2(m_\chi/T)\right]^2 . \tag{4.21}$$

The thermal average is then cast in terms of only one integral which must be evaluated

$$\langle \sigma v_{\text{Møl}} \rangle = \frac{1}{8m_\chi^4 T K_2^2(m_\chi/T)} \int_{4m_\chi^2}^{\infty} ds \ \sigma (s - 4m_\chi^2)\sqrt{s} K_1(\sqrt{s}/T) \tag{4.22}$$

Recasting Eq.(4.12) in comoving coordinates using Eq.(3.42) gives

$$\frac{x}{Y_\chi^{\text{eq}}} \frac{dY_\chi}{dx} = -\frac{\Gamma}{\overline{H}} \left[\left(\frac{Y_\chi}{Y_\chi^{\text{eq}}} \right)^2 - 1 \right] \ , \tag{4.23}$$

where $Y_\chi^{\text{eq}} = n_\chi^{\text{eq}}/s$ and $\Gamma \equiv n_\chi^{\text{eq}} \langle \sigma v_{\text{Møl}} \rangle$ is the interaction rate between χ and X. The DM relic abundance is then calculated to be[1]

$$\Omega_c h^2 = \frac{m_\chi Y_\chi^0 s_0 h^2}{\rho_c} \ , \tag{4.24}$$

where s_0 is the entropy density today.

[1]If χ is not its own antiparticle, then $\Omega h^2 = \frac{\rho_\chi + \rho_{\bar{\chi}}}{\rho_c}$. If the particle species has negligible chemical potential then $\Omega h^2 = 2\Omega_\chi h^2$, since $Y_\chi = Y_{\bar{\chi}}$.

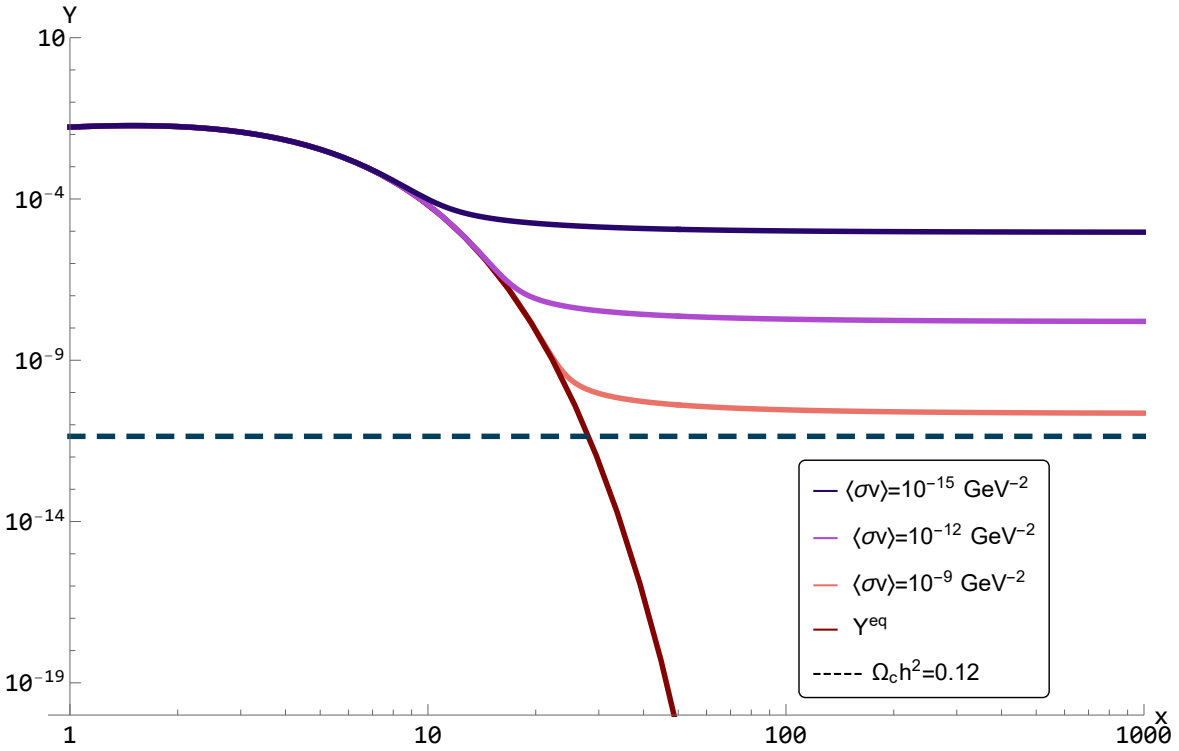

Figure 4.9: The solution of Eq.(4.23), with three different values of the thermally averaged cross section: $\langle\sigma v\rangle = 1\times10^{-15}$ GeV^{-2}, 1×10^{-12} GeV^{-2} and 1×10^{-9} GeV^{-2} corresponding to the blue, purple and red curves. The brown line is the equilibrium comoving number density, while the dashed line corresponds to the number density giving $\Omega_c h^2 = 0.12$.

In figure 4.9 the abundance Y_χ is plotted as a function of $x = m_\chi/T$. We can see that initially (small x) there is equilibrium between the WIMP and the particle species X. At this time the interaction rate is dominated by the Hubble rate ($\Gamma \gg H(T)$). If some DM particles are created (annihilated) at this time, we will see that Y_χ increases (decreases). This means that the value inside the parenthesis of Eq.(4.23) is positive (negative), hence the number density follows the equilibrium number density, as is expected when the hidden sector and the visible sector is in thermal equilibrium. As the scale factor increases, the temperature decreases. When the temperature becomes less than the WIMP mass, the equilibrium number density becomes exponentially suppressed, $n^{\text{eq}} \propto \exp(-x)$ for $x \ll 1$. When the interaction rate becomes less than the Hubble rate ($\Gamma \simeq H$), WIMPs will not be able to annihilate anymore and freeze-out, i.e., the comoving number density becomes constant, since when $\Gamma \to 0$, $\frac{dY}{dT} \to 0$. This can be seen to happen when $x \sim 10 - 30$ in figure 4.9. We can also see that the final comoving number density decreases with an increase of $\langle\sigma v\rangle$. This is because a larger value of $\langle\sigma v\rangle$ means that the comoving number density follows the equilibrium number density for a longer time and the Boltzmann suppression gives us a lower final number density. Solving for the final relic abundance one finds that the thermally

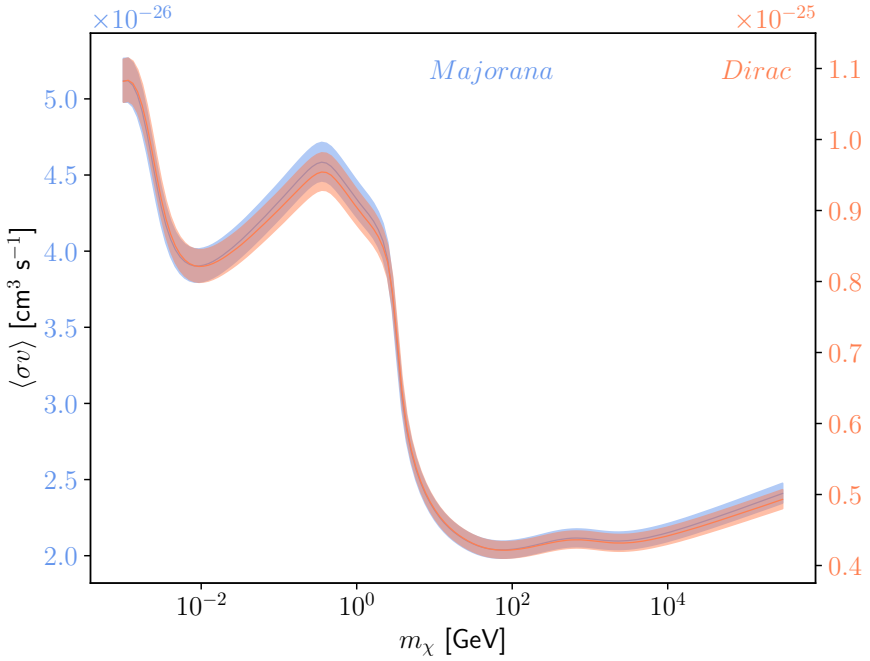

Figure 4.10: The value of constant thermally averaged cross section $\langle\sigma v\rangle$ that gives the correct relic density for a Majorana (blue) or Dirac (red) DM particles (shaded areas in- dicate the effect of varying $\Omega_c h^2$ within 3σ [1]). This plot and the plot in figure 4.11 were produced using DarkSUSY [7]; they reproduce what is shown in Ref. [104].

averaged cross section that corresponds to the observed relic abundance ($\Omega_c h^2 = 0.12$) is $\langle\sigma v\rangle \sim 10^{-26}\text{cm}^3\text{s}^{-1}$ [4].

For non-relativistic gases, the thermally averaged cross section can be expanded in terms of powers of x^{-1}. This can be done by noting that $s = 4m_\chi^2 + m^2v^2$ and expanding σv in terms of v^2 [4]. Taking the thermal average gives [101]

$$\langle\sigma v\rangle = \langle a + bv^2 + cv^4 + ...\rangle \tag{4.25}$$

$$= a + \frac{3}{2}bx^{-1} + \frac{16}{8}cx^{-2} + ... \tag{4.26}$$

For non-relativistic particles the higher order terms can be neglected. If we have a s-wave annihilation, then $a \neq 0$, meaning that the thermally averaged cross section is to first order given by $\langle\sigma v\rangle = a$. The $\langle\sigma v\rangle$ that gives the correct relic abundance is plotted in figure 4.10. In the case of p-wave annihilations then $a = 0$, meaning that to first order $\sigma v_{\text{Møl}} = bv^2_{\text{Møl}}$. The value of b that gives correct relic density is plotted in figure 4.11. An important observation is that the thermally averaged cross section for a typical weak scale cross section with weak scale mass can be roughly approximated as

$$\langle\sigma v\rangle \sim \frac{\alpha^2}{m_\chi^2}\ , \tag{4.27}$$

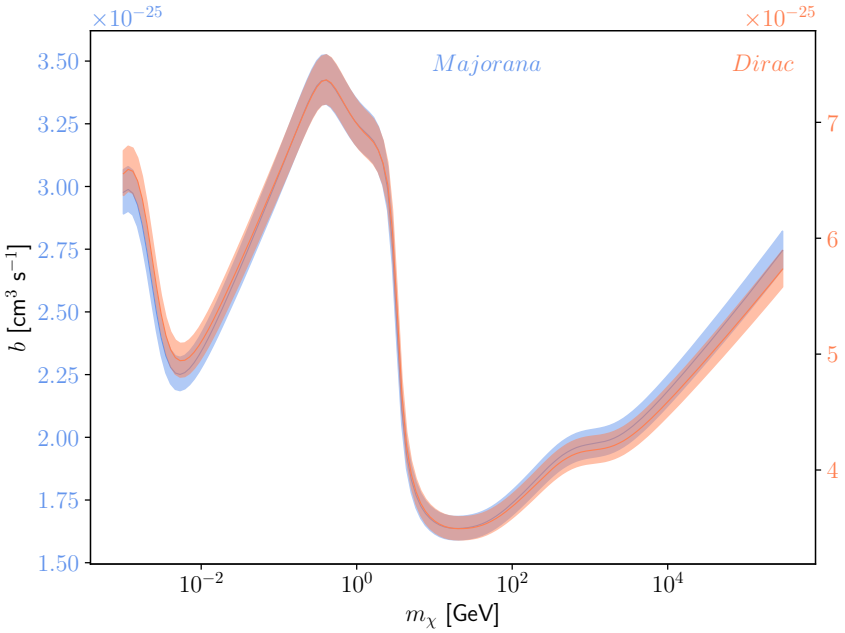

Figure 4.11: The value of b in the p-wave annihilation cross section σv_{lab}^2 that gives the correct relic abundance.

where $\alpha \sim 0.01$ is a coupling of the order of the weak scale. The WIMP mass that gives the correct relic density has to be a weak scale mass, $m_\chi \sim 250$ GeV. This observation is as mentioned before, the well-known *WIMP miracle* [3] and is one of the reasons why the WIMP paradigm and thermal freeze-out is popular. A precise treatment has been done by Ref. [105], which found that the correct relic density is given by the following thermally averaged cross sections

$$\langle \sigma v \rangle \simeq \begin{cases} 5 \cdot 10^{-26}\ \text{cm}^3\text{s}^{-1} & (100\ \text{MeV} \lesssim m_\chi \lesssim 5\ \text{GeV}), \\ 2.2 \cdot 10^{-26}\ \text{cm}^3\text{s}^{-1} & (10\ \text{GeV} \lesssim m_\chi \lesssim 10\ \text{TeV}). \end{cases} \tag{4.28}$$

Even though this observation fits well with respect to naturalness and the hierarchy problem, which indicates that there might be more new physics at the electroweak scale. It is important to note that different masses and cross sections give correct $\langle \sigma v \rangle$, this means that the fact that a weak scale cross section and mass gives the correct relic abundance might be by sheer coincidence. After decades of searches for WIMPs with no convincing results, many are starting to look at other production mechanisms such as *freeze-in*, which will be discussed in the next chapter.

Chapter 5

Freeze-In

In Chapter 4, I discussed how the freeze-out mechanism can be used to explain the production of WIMPs in the early universe. The null results from detection experiments looking for WIMPs in the last decades have made other production mechanisms, such as freeze-in, more popular. In this chapter I will start with a general discussion about the Freeze-in mechanism which was introduced in [5]. I will then in section 5.2, give expressions for the Boltzmann-equation for Freeze-in, where I deviate from the approach that is usually taken. Instead of giving the collision operation in terms of the creation cross section, I will give it in terms of the annihilation cross section, which is a more suitable way of expressing the Boltzmann equation when implementing freeze-in in a model-independent way. This has been implemented in DarkSUSY which is introduced Appendix A.

5.1 The mechanism

The freeze-out mechanism bases itself on the key assumption that the dark sector and the visible sector initially were in thermal equilibrium. We know from the anisotropies in the CMB that the visible sector was in thermal equilibrium [1], but this does not necessarily encompass the dark sector particles. It is this fact that the freeze-in mechanism exploits. It uses that if the coupling, λ, between the visible sector and DM particles is very small then the dark sector and the visible sector never thermalise. Another key assumption in freeze-in is that the initial DM abundance is negligible. This can happen in cases when inflation happens to only thermalise the visual sector. This means that the DM phase space distribution initially was $f_\chi \sim 0$, which in turn means that the initial DM abundance is negligible. The DM abundance is then produced by decays or annihilations of visible sector bath particles [5]. These DM particles are, as mention in the previous chapter, called *Feebly Interacting Massive Particles*. If the FIMP χ abundance is produced from decays, then the production is active until

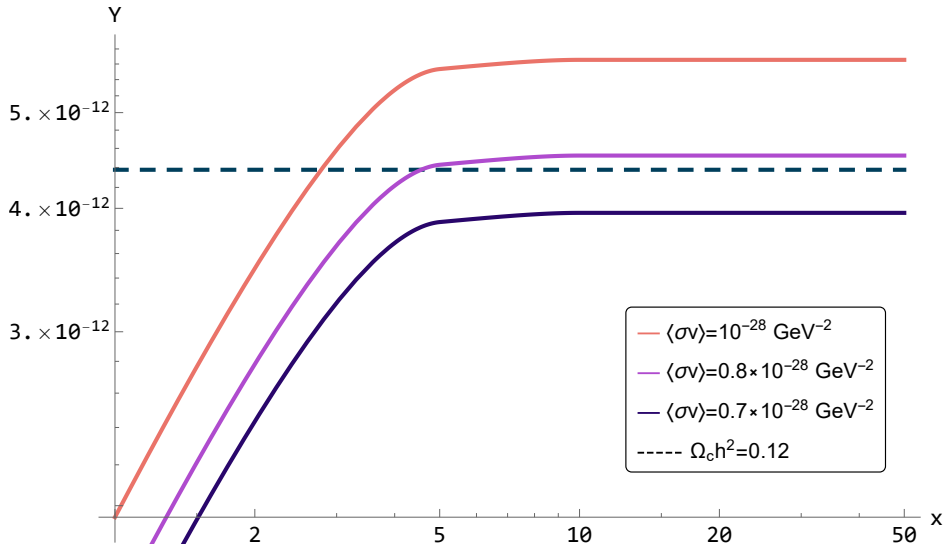

Figure 5.1: The DM abundance Y produced from $2 \to 2$ scatterings, assuming a four-point scalar interaction as a function $x = m_\chi/T$. Three different values of the thermally averaged cross section are displayed: $\langle \sigma v \rangle = 1 \times 10^{-28}$ GeV^{-2} (red), 0.8×10^{-28} GeV^{-2} (purple), and 0.7×10^{-28} GeV^{-2}. The dashed line corresponds to the number density giving $\Omega_c h^2 = 0.12$.

the expansion of the universe overtakes the reaction rate, i.e. the number density for the bath particles that contribute to the freeze-in yield becomes Boltzmann-suppressed (similar to the freeze-out mechanism). If the abundance is produced from annihilations of bath particles, it is the number density of high energy particles that can contribute to the production that will become Boltzmann-suppressed (there will still be relativistic bath particles, but they do not contribute to the production). The size of the coupling determining if the visible and the dark sector thermalises is model dependent, but the coupling λ will typically have to be of the order of magnitude $\lambda \simeq \mathcal{O}(10^{-7})$ or less. For a scalar coupled to the visible sector by the term $\mathcal{L} \supset \frac{1}{4}\lambda\chi^2 h^2$, one finds that the thermal equilibrium condition is [106]

$$\frac{\Gamma_{hh\to\chi\chi}}{H} \sim \frac{\lambda^2 10^{16}\text{GeV}}{T} > 1 \ , \tag{5.1}$$

which means that for the DM particles and visible sector to not be in thermal equilibrium before electroweak phase transition ($T \simeq 163$ GeV), the coupling has to be smaller than $\lambda < 10^{-7}$. The comoving number density for the FIMPs becomes constant and is said to *freeze-in*. This can be seen in figure 5.1, where the FIMP abundance is produced from $2 \to 2$ scatterings, where a four-point scalar interaction is assumed. Initially we see that $Y_\chi = 0$, but FIMPs are constantly produced until $x \sim 5$ when the abundance freezes-in.

For a qualitative discussion I will for the rest of this section use an approximated solution for the comoving number density. The full treatment using the Boltzmann

equation will be done in section 5.2. For a renormalizable interaction which I will assume is a quartic scalar interaction, the FIMP will be produced by decays or collisions of bath particles at a rate proportional to λ^2.

If we suppose that the abundance is produced from decays of a bath particle σ, then the abundance at a temperature T can be approximated by multiplying the decay rate $\Gamma_{\sigma\to\chi\chi}$ with the time it takes to populate the FIMP abundance [5]

$$Y_\chi(T) \sim t\Gamma_{\sigma\to\chi\chi} \sim \lambda^2 \frac{m_P}{T} \ . \tag{5.2}$$

where the time it takes is a Hubble doubling time, which is the time it takes for the universe to double its size. This is found from the time-temperature relation for a radiation dominated universe $H = \frac{1}{2t} \simeq \frac{1.66}{m_P}\sqrt{g_{\text{eff}}}T^2$, which means that $t \sim \frac{m_P}{T^2}$. We can see that this process is IR dominated, and since these processes are renormalizable, the dominant production will always be IR dominated [31]. For temperatures below the mass of the heaviest particle in the process ($T < \max[m_\chi, m_{\text{SM}}]$, let us assume the FIMP is heaviest) the process will be Boltzmann-suppressed. This means that the FIMP abundance will be

$$Y_\chi \sim \lambda^2 \frac{m_P}{m_\chi} \ , \tag{5.3}$$

since the dominant contribution happens as $T \sim m_\chi$. Using Eq.(4.24) we see that

$$\Omega_c h^2 \sim \lambda^2 10^{27} \ , \tag{5.4}$$

which means that in order to get the correct relic abundance, $\Omega_c h^2 = 0.12$, the coupling have to be $\lambda \sim 10^{-14}$, note that this is only a very rough estimate. We can see from Eq.(5.3) that increasing the interaction rate in the freeze-in scenario will have the opposite effect to that of the freeze-out scenario. Increasing the coupling will give a larger final abundance, while in the freeze-out case the abundance will become smaller; this can be seen in both figure 5.1 and figure 5.2. The features of figure 5.2 is worth stressing, for very low couplings we see that we are in the freeze-in regime, where the relic-abundance will increase with an increase in the coupling. When the coupling increases enough that thermal equilibrium will be reached, the abundance will flatten out because annihilations of DM particles in equilibrium takes place. Finally, when the coupling is large enough, we can assume that thermal equilibrium was achieved long before decoupling, meaning that we have entered the usual freeze-out regime. Even though freeze-in and freeze-out have these opposite features, they still have similarities. Both production methods can make predictions solely from some few parameters, such as FIMP coupling(s) and mass(es). Both scenarios can have that the particle(s) that are produced may not be the lightest particle in the dark sector, which means that they may decay into the actual DM particles. As mentioned before, renormalizable interactions will be IR dominated, which means that freeze-in won't be sensitive to the reheating temperature. This is not the case for non-renormalizable operators (this is the so-called *ultraviolet freeze-in* [107]); they will on the other hand be sensitive to the reheating temperature set by inflation. This is an important distinction from freeze-out where all traces of initial conditions are erased due to thermal equilibrium.

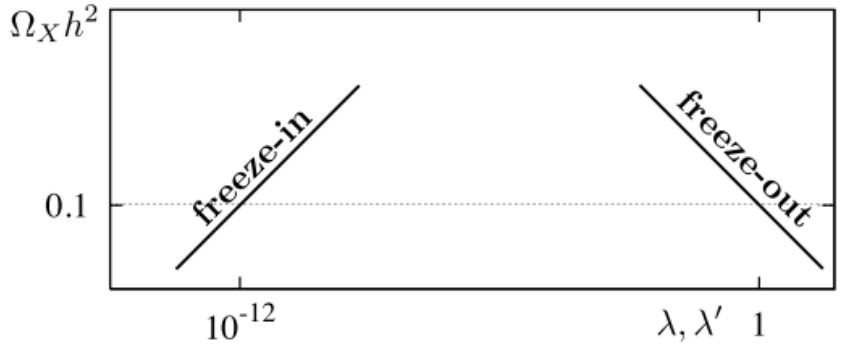

Figure 5.2: Schematic representation of the FIMP relic abundance as a function of the coupling between DM and the visible sector. Image taken from [5].

5.2 Freeze-in Boltzmann Equation

In this section I will develop the Boltzmann equation for the freeze-in scenario, where the dominant contribution of FIMPs comes from decay of an on-shell bath particle $(1 \to 2)$ or from $(2 \to 2)$ annihilations of bath particles. Using Eq.(3.43) we get that the most general form of the Boltzmann-equation for the process $a+b+... \leftrightarrow \chi+k+l...$ is

$$\begin{aligned}\dot{n}_\chi + 3Hn_\chi = \int d\Pi_a d\Pi_b ... d\Pi_\chi d\Pi_k d\Pi_l ... \times [f_a f_b ... (1 \pm f_\chi)(1 \pm f_k) ... |\mathcal{M}|^2_{I\to J} \\ - f_\chi f_k ... (1 \pm f_a)(1 \pm f_b) ... |\mathcal{M}|^2_{J\to I}] \times (2\pi)^4 \delta^4 (\sum_{i\in I} p_i - \sum_{j\in O} p_j) \ .\end{aligned} \tag{5.5}$$

We can easily apply this to the freeze-in scenario, which is characterized by the following two independent requirements on the DM distribution

- $f_\chi \ll 1$. Due to the small DM abundance, which means that $1 \pm f_\chi \sim 1$.
- $f_\chi \ll f_i$, where i is any visual sector bath particle. This is due to the fact that the DM abundance stays sub-thermal. The effects of DM annihilations, which is described by the second term in Eq.(5.5), is therefore negligible.

The Boltzmann-equation describing the freeze-in process $a + b + ... \to \chi + k + l...$ is therefore

$$\begin{aligned}\dot{n}_\chi + 3Hn_\chi = \int d\Pi_a d\Pi_b ... d\Pi_\chi d\Pi_k d\Pi_l ... \times [f_a f_b ... (1 \pm f_k)(1 \pm f_l) ... |\mathcal{M}|^2_{I\to J}] \\ \times (2\pi)^4 \delta^4 (\sum_{i\in I} p_i - \sum_{j\in O} p_j) \ .\end{aligned} \tag{5.6}$$

The processes I am interested in is the $2 \to 2$ and $1 \to 2$ processes, which I will solve for below. In order to keep the discussion in this section general, I allow for the particles to have arbitrary mass and spin. I want to emphasise that I will express the DM production of two FIMPs χ from two heat bath (SM) particles s, in terms of the annihilation of a *would-be* thermal population of FIMPs. I will show that this equivalence holds both when assuming Maxwell-Boltzmann distributions for the thermal bath particles, as I did in the freeze-out case (see Eq.(4.7) and the discussion above it), and when the quantum-statistical effects in the phase-space distributions of the involved particles are included.

5.2.1 $2 \to 2$ Processes

I will focus on the $2 \to 2$ processes in this thesis, mainly because the $2 \to 2$ process can be seen to reduce to the $1 \to 2$ process when the mediator is on-shell (see Appendix B). The process $s + \bar{s} \to \chi + \bar{\chi}$ has the following Boltzmann equation, seen from Eq.(5.6)

$$\dot{n}_\chi + 3Hn_\chi = \int d\Pi_a d\Pi_{\bar{s}} d\Pi_\chi d\Pi_{\bar{\chi}} \; f_s f_{\bar{s}} |\mathcal{M}|^2_{s\bar{s}\to\chi\bar{\chi}} (2\pi)^4 \delta^4(p_s + p_{\bar{s}} - p_\chi - p_{\bar{\chi}}) \; . \tag{5.7}$$

The conventional approach is to rewrite the equation in terms of $\sigma_{s\bar{s}\to\chi\bar{\chi}}$ and get the thermal average cross section by integrating over the phase space of the initial states [5, 31, 108, 109]. This approach has the advantage of being very intuitive, but one has to calculate the thermally averaged cross sections for all the processes and calculate the number density for all the particles in the heat bath. I have therefore chosen to take a different approach, one that is more similar to the one used in freeze-out. I use a mathematical trick to rewrite the phase space distribution functions for s and $\bar{s}$ in terms of an equilibrium phase space distributions for χ and $\bar{\chi}$. We will see that for FIMPs, this distribution will be the Maxwell-Boltzmann distribution. However, this has nothing to do with the *actual* distribution function for the FIMPs. This trick was done for the case of Maxwell-Boltzmann distributions in Eq.(4.7). The same trick can be used on both Bose-Einstein distributions and Fermi-Dirac distributions, as I will show below. This has the advantages of reducing to one thermally averaged cross section when Maxwell-Boltzmann distributions are used, and we can use that the annihilation cross section sometimes can be conveniently rewritten in terms the off-shell partial decay width of a known SM particle, meaning that higher-order corrections can more easily be included. For particles in thermal equilibrium one has to, as mentioned in section 3.2, use Bose-Einstein distributions for bosons and Fermi-Dirac distributions for fermions when the distribution cannot be approximated using the Maxwell-Boltzmann distribution, i.e. when the inequality $e^{E_i/T} \gg 1$ does not hold. These are given in the rest frame of the gas by Eq.(3.1). These distributions can be put in the Lorentz invariant form [110], which for a particle species s is given by

$$f_s(p) = \frac{1}{e^{\frac{u \cdot p_s}{T}} - \varepsilon_s} \; . \tag{5.8}$$

where $\varepsilon_s = 1$ for bosons, $\varepsilon_s = -1$ for fermions and $\varepsilon_s = 0$ gives the Maxwell-Boltzmann distribution. u_μ is the 4-velocity of our reference frame relative to the gas reference frame (in the gas reference frame we have $u = (1, 0, 0, 0)^T$, which returns the usual representation of the distributions). I have used that $\mu = 0$ since we have full equilibrium. If we only have kinetic equilibrium, one has to substitute $u \cdot p_s$ with $u \cdot p_s - \mu_s$. It is easily seen that

$$f_s = (1 + \varepsilon_s f_s) e^{-\frac{u \cdot p_s}{T}} \ . \tag{5.9}$$

This means that for a $2 \to 2$ process $a + b \to c + d$ we get

$$f_a f_b (1 + \varepsilon_c f_c)(1 + \varepsilon_d f_d) = f_c f_d (1 + \varepsilon_a f_a)(1 + \varepsilon_b f_b) \ , \tag{5.10}$$

where we have used that $p_a + p_b = p_c + p_d$ (if we only assume kinetic equilibrium one gets a factor $\exp[\frac{\mu_a + \mu_b - \mu_c - \mu_d}{T}]$ on the right-hand side). It is easily seen how this generalises to arbitrary processes, but I will only use the $2 \to 2$ case. For FIMPs we can use that by momentum conservation we get

$$f_s f_{\bar{s}} = f_\chi^{\rm MB} f_{\bar{\chi}}^{\rm MB} (1 + \varepsilon_s f_s)(1 + \varepsilon_s f_{\bar{s}}) \ . \tag{5.11}$$

where I introduce that

$$f_\chi^{\rm MB}(p_\chi) \equiv e^{-\frac{u \cdot p_\chi}{T}} \ . \tag{5.12}$$

I want to stress that this result does not make any assumption of the *actual* phase space distribution of the FIMPs, other than the already assumed assumption $f_\chi \ll 1$. Finally, I use CP invariance on the scattering amplitude squared and summed over both initial and final state degrees of freedom to get: $|\mathcal{M}|^2 \equiv |\mathcal{M}_{s\bar{s} \to \chi\bar{\chi}}|^2 = |\mathcal{M}_{\chi\bar{\chi} \to s\bar{s}}|^2$. The $2 \to 2$ Boltzmann-equation will then take the following form:

$$\begin{aligned} \dot{n}_\chi + 3Hn_\chi = \int d\Pi_s d\Pi_{\bar{s}} d\Pi_\chi d\Pi_{\bar{\chi}} \ f_\chi^{\rm MB} f_{\bar{\chi}}^{\rm MB} (1 + \varepsilon_s f_s)(1 + \varepsilon_s f_{\bar{s}}) |\mathcal{M}|^2_{\chi\bar{\chi} \to s\bar{s}} \\ \times (2\pi)^4 \delta^4(p_s + p_{\bar{s}} - p_\chi - p_{\bar{\chi}}) \ , \end{aligned} \tag{5.13}$$

which has the feature that the production term now takes the form the form of an annihilation term with an auxiliary DM phase-space density described by a Maxwell-Boltzmann distribution. This means that I can rewrite Eq.(5.7) to get

$$\dot{n}_\chi + 3Hn_\chi = \langle \sigma v_{\rm M\o l} \rangle n_\chi^{\rm MB} n_{\bar{\chi}}^{\rm MB} \ , \tag{5.14}$$

where $n_\chi^{\rm MB}$ is given by Eq.(4.13),

$$\langle \sigma v_{\rm M\o l} \rangle_{\chi\bar{\chi} \to s\bar{s}} = \frac{\int d^3p_\chi d^3p_{\bar{\chi}} \sigma_{\chi\bar{\chi} \to s\bar{s}}(p_\chi, p_{\bar{\chi}}) v_{\rm M\o l} f_\chi^{\rm MB} f_{\bar{\chi}}^{\rm MB}}{\int d^3p_\chi d^3p_{\bar{\chi}} f_\chi^{\rm MB} f_{\bar{\chi}}^{\rm MB}} \tag{5.15}$$

and $\sigma(p_\chi, p_{\bar{\chi}})$ is the in-medium annihilation cross section in the cosmic rest frame, since it takes into account the effect of quantum statistics of the final state defined by

$$\sigma_{\chi\bar{\chi} \to s\bar{s}}(p_\chi, p_{\bar{\chi}}) \equiv \frac{1}{4F(p_\chi, p_{\bar{\chi}})} \int d\Pi_s d\Pi_{\bar{s}} \overline{|\mathcal{M}|}^2 (1 + \varepsilon_s f_s)(1 + \varepsilon_s f_{\bar{s}})(2\pi)^4 \delta^4(p_\chi + p_{\bar{\chi}} - p_s - p_{\bar{s}}) \ . \tag{5.16}$$

Comparing Eq.(5.14) to Eq.(4.12) we see that the form of the DM production terms are identical, but there are some important physical distinctions. In the freeze-out case $f_\chi^{\rm MB}$ would describe the *actual* DM equilibrium distribution and as I mentioned in section 4.4, we can neglect the quantum statistical factors, this is not the case for freeze-in. However, the form of Eq.(5.14) is still very useful. The fact that it takes the same form as the freeze-out case is beneficial both in terms of implementing numerical solutions and when estimating higher-order corrections to the annihilation cross sections. We can now easily include all the initial states, this is the same as replacing $\sigma_{\chi\bar{\chi}\to s\bar{s}}$ with

$$\sigma(p_\chi, p_{\bar{\chi}}) = \sum_{i,j} \sigma_{\chi\bar{\chi}\to s_i\bar{s}_j} \ . \tag{5.17}$$

The present-day FIMP abundance is thus

$$Y_{2\to 2} = \frac{g_\chi^2 m_\chi^4}{4\pi^4} \int_{T_0}^{T_R} \frac{dT}{\overline{H}s(T)T} T^2 \sum_{i,j} \langle \sigma v_{\rm Møl} \rangle_{\chi\bar{\chi}\to s_i\bar{s}_j} K_2(m_\chi/T)^2 \ , \tag{5.18}$$

where T_R is the *reheating temperature* after inflation, T_0 is the present-day temperature. Note that if we can set $\varepsilon = 0$ for all species, then Eq.(5.15) becomes Eq.(4.22). If the quantum effects of a particle s and/or $\bar{s}$ are not negligible, then we have to evaluate Eq.(5.16) and use it in Eq.(5.15). In order to do this, I will do follow what Giorgio Arcadi et al. [111] has done for Bose-Einstein distributions in their relativistic treatment of real scalar dark matter. I will include Fermi-Dirac distributions and use it for the freeze-in scenario. Since the phase-space integrals in Eq.(5.15) are most easily calculated in the centre-of-mass (CMS) frame, we will Lorentz transform the momenta from the cosmic rest frame to the CMS frame. This has the additional feature that the cross section has to be calculated in the CMS frame, which is the standard frame cross sections are stated in, in particle physics. I introduce the useful 4-vectors

$$p = \frac{p_\chi + p_{\bar{\chi}}}{2}, \quad k = \frac{p_\chi - p_{\bar{\chi}}}{2} \ , \tag{5.19}$$

where $p = (\sqrt{s}/2, 0, 0, 0)$ is in the CMS frame and $\sqrt{s}$ is the CMS energy. Due to the isotropy of space, we know that the relation to the cosmic rest frame must be possible to state in terms of a single boost parameter, which we will see is the rapidity η or the Lorentz factor γ. The 4-momentum p in the cosmic rest frame can be expressed in terms of the CMS frame by the Lorentz transformation $\Lambda(p)$

$$p = \Lambda(p) \begin{pmatrix} \sqrt{s}/2 \\ 0 \\ 0 \\ 0 \end{pmatrix} \ . \tag{5.20}$$

By parameterising p in terms of the rapidity η and the angular coordinates θ, ϕ, we find

$$\begin{aligned} p^0 &= E\cosh\eta \ , \\ p^1 &= E\sinh\eta\sin\theta\sin\phi \ , \\ p^2 &= E\sinh\eta\sin\theta\cos\phi \ , \\ p^3 &= E\sinh\eta\cos\theta \ . \end{aligned} \tag{5.21}$$

Using the convention $p = (p^0, p^3, p^2, p^1)^T$, we find that $\Lambda(p)$ and $\Lambda^{-1}(p)$ is

$$\Lambda(p) = \begin{pmatrix} 1 & 0 & 0 & 0 \\ 0 & 1 & 0 & 0 \\ 0 & 0 & \cos\phi & -\sin\phi \\ 0 & 0 & \sin\phi & \cos\phi \end{pmatrix} \begin{pmatrix} 1 & 0 & 0 & 0 \\ 0 & \cos\theta & -\sin\theta & 0 \\ 0 & \sin\theta & \cos\theta & 0 \\ 0 & 0 & 0 & 1 \end{pmatrix} \begin{pmatrix} \cosh\eta & \sinh\eta & 0 & 0 \\ \sinh\eta & \cosh\eta & 0 & 0 \\ 0 & 0 & 0 & 0 \\ 0 & 0 & 0 & 0 \end{pmatrix} , \tag{5.22}$$

$$\Lambda^{-1}(p) = \begin{pmatrix} \cosh\eta & -\sinh\eta & 0 & 0 \\ -\sinh\eta & \cosh\eta & 0 & 0 \\ 0 & 0 & 0 & 0 \\ 0 & 0 & 0 & 0 \end{pmatrix} \begin{pmatrix} 1 & 0 & 0 & 0 \\ 0 & \cos\theta & \sin\theta & 0 \\ 0 & -\sin\theta & \cos\theta & 0 \\ 0 & 0 & 0 & 1 \end{pmatrix} \begin{pmatrix} 1 & 0 & 0 & 0 \\ 0 & 1 & 0 & 0 \\ 0 & 0 & \cos\phi & \sin\phi \\ 0 & 0 & -\sin\phi & \cos\phi \end{pmatrix} . \tag{5.23}$$

Since the Lorentz invariant integration measure is

$$\frac{d^3\mathbf{p}_\chi}{2E_\chi}\frac{d^3\mathbf{p}_{\bar\chi}}{2E_{\bar\chi}} = d^4p_\chi d^4p_{\bar\chi}\delta(p_\chi^2 - m_\chi^2)\delta(p_{\bar\chi}^2 - m_\chi^2)\theta(p_\chi^0)\theta(p_{\bar\chi}^0) \ , \tag{5.24}$$

where I have used that $m_\chi = m_{\bar\chi}$ and that $\theta(x)$ is the Heaviside step function. We can change the measure to d^4p and d^4k easily since the Jacobian is 2^4 due to the fact that the change of variable is simply a shift. Therefore

$$d^4p_\chi d^4p_{\bar\chi}\delta(p_\chi^2 - m_\chi^2)\delta(p_{\bar\chi}^2 - m_\chi^2) = 2^4 d^4p d^4k\delta((p+k)^2 - m_\chi^2)\delta((p-k)^2 - m_\chi^2) \ . \tag{5.25}$$

Since the measure is Lorentz invariant, we can calculate it in any frame. From Eq.(5.21) we find

$$d^4p = \frac{\sinh^2\eta\ s}{2^5} d\eta\ ds\ d\Omega_p \ , \tag{5.26}$$

where $d\Omega_p = d\cos\theta\ d\phi$ are the angles in p-space. The k measure can be written as

$$d^4k = |\mathbf{k}|^2 dk_0\ d|\mathbf{k}|\ d\Omega_k \ , \tag{5.27}$$

which we can integrate in the CMS frame to get

$$\int dk_0\ d\mathbf{k}||\mathbf{k}|^2\delta((p+k)^2 - m_\chi^2)\delta((p-k)^2 - m_{\bar\chi}^2) = \frac{\sqrt{s - 4m_\chi^2}}{8\sqrt{s}} \ , \tag{5.28}$$

where the δ functions enforces $k^0 = 0$ and $|\mathbf{k}| = \frac{1}{2}\sqrt{s - 4m_\chi^2}$. This means that for any function $g(p_\chi, p_{\bar\chi})$ we have

$$\int d\Pi_\chi d\Pi_{\bar\chi} g(p_\chi, p_{\bar\chi}) = \frac{1}{16(2\pi)^6}\int_{4m_\chi^2}^\infty ds\sqrt{s(s-4m_\chi^2)}\int_0^\infty d\eta\sinh^2\eta\int d\Omega_p d\Omega_k g(p_\chi, p_{\bar\chi}) \ . \tag{5.29}$$

I change variable from the rapidity η to the Lorentz factor $\gamma = \cosh\eta$, which means that

$$\int d\Pi_\chi d\Pi_{\bar{\chi}} g(p_\chi, p_{\bar{\chi}}) = \frac{1}{16(2\pi)^6}\int_{4m_\chi^2}^\infty ds\sqrt{s(s-4m_\chi^2)}\int_1^\infty d\gamma\sqrt{\gamma^2-1}\int d\Omega_p d\Omega_k g(p_\chi, p_{\bar{\chi}})\,. \tag{5.30}$$

In the different distribution functions we need $u\cdot p_i$ in the CMS frame, this is

$$u\cdot p_i = p_i^0\cosh\eta + p_i^3\sinh\eta\,. \tag{5.31}$$

The distributions for χ becomes

$$f_\chi^{\rm MB} f_{\bar{\chi}}^{\rm MB} = e^{-\frac{\sqrt{s}\cosh\eta}{T}} = e^{-\frac{\sqrt{s}\gamma}{T}}\,. \tag{5.32}$$

For the Bose-enhancement and Fermi-blocking factors we find

$$\begin{aligned} G(\gamma, s, \cos\theta) &= (1+\varepsilon_s f_s(u\cdot p_s))(1+\varepsilon_s f_{\bar{s}}(u\cdot p_{\bar{s}})) \qquad (5.33)\\ &= \left(1+\varepsilon_s^2 e^{-\frac{\sqrt{s}}{T}\gamma} - \varepsilon_s\left(e^{-\frac{1}{T}\left[\left(\sqrt{\mathbf{p_s}^2+m_s^2}\right)\gamma + |\mathbf{p_s}|\cos\theta\sqrt{\gamma^2-1}\right]} + e^{-\frac{1}{T}\left[\left(\sqrt{s}-\sqrt{\mathbf{p_s}^2+m_s^2}\right)\gamma - |\mathbf{p_s}|\cos\theta\sqrt{\gamma^2-1}\right]}\right)\right)^{-1}, \end{aligned}$$

where I have included the ε_s^2 factor, since letting $\varepsilon_s \to 0$ gives $G(\gamma, s, \cos\theta) = 1$. Putting everything together we get

$$\langle\sigma v_{\rm M\o l}\rangle_{\chi\bar{\chi}\to s\bar{s}} = \frac{1}{8m_\chi^4 T K_2^2(m_\chi/T)}\int_{4m_\chi^2}^\infty ds\sqrt{s}(s-4m_\chi^2)\frac{\sqrt{s}}{T}\int_1^\infty d\gamma\sqrt{\gamma^2-1}e^{-\frac{\sqrt{s}}{T}\gamma}\sigma^{\rm CM}(s,\gamma)\,, \tag{5.34}$$

with

$$\begin{aligned} \sigma^{\rm CM}(s,\gamma) &= \frac{1}{4F(p_\chi, p_{\bar{\chi}})}\int d\Pi_s d\Pi_{\bar{s}}(2\pi)^4\delta^4(p_\chi + p_{\bar{\chi}} - p_s - p_{\bar{s}})\overline{|\mathcal{M}|}^2 G(s,\gamma,\cos\theta) \qquad (5.35)\\ &= \frac{N_s^{-1}}{16\pi s}\frac{|\mathbf{p_s}|}{\sqrt{s-4m_\chi^2}}\int_{-1}^1 d\cos\theta_{\rm CM}|\mathcal{M}|^2(s,\cos\theta_{\rm CM})G(\gamma,s,\cos\theta_{\rm CM})\,, \end{aligned}$$

where $\theta_{\rm CM}$ is the CMS angle and I have introduced the factor $N_s = 2$ (1) for self-conjugate (not self-conjugate) SM particles s, since the integrals have been performed over all possible momentum configurations. We can now easily see that by letting $\varepsilon_s \to 0$, we recover the well known Maxwell-Boltzmann case; since $G(s,\gamma,\cos\theta_{\rm CM}) = 1$ Eq.(5.34) reduces to the result given by Eq.(4.22), which we now can appreciate is due to the fact that the cross section $\sigma^{\rm CM}_{\varepsilon\to 0}$ is only a function of s. For a general process where both s-channel, t-channel and u-channel processes must be included, this is not possible and Eq.(5.35) must be calculated in full. The exception is if the scattering amplitude is only s-dependent: $|\mathcal{M}|^2(s,t) = |\mathcal{M}|^2(s)$. If that is the case, we can use that

$$\begin{aligned} \sigma^{\rm CM}(s,\gamma) &= \frac{N_s^{-1}}{8\pi s}\frac{|\mathbf{p_s}|}{\sqrt{s-4m_\chi^2}}|\mathcal{M}|^2(s)\int_{-1}^1 d\cos\theta_{\rm CM}\frac{G(\gamma,s,\cos\theta_{\rm CM})}{2} \qquad (5.36)\\ &= \sigma^{\rm CM}_{\varepsilon_s\to 0}(s)\overline{G}(\gamma,s) \end{aligned}$$

where $\sigma^{\rm CM}(s)$ is the usual cross section calculated in the CMS frame and

$$\overline{G}(s,\gamma) \equiv \int_{-1}^{1} d\cos\theta_{\rm CM} \frac{G(\gamma, s, \cos\theta_{\rm CM})}{2} \ . \tag{5.37}$$

This integral can be solved analytically by using that

$$\int dx (e^{a+bx} \mp 1)^{-1} (e^{c-bx} \mp 1)^{-1} = \frac{\log(1 \mp e^{a+bx}) - \log(e^c \mp e^{bx})}{b(e^{a+c} - 1)} + C \tag{5.38}$$

Using Eq.(5.31) on the expressions for $f_s(u \cdot p_s)$ and $f_{\bar{s}}(u \cdot p_{\bar{s}})$, I find that

$$\bar{G} = \frac{\exp[a_s + a_{\bar{s}}]}{b(\exp[a_s + a_{\bar{s}}] - 1)} \log\left[\frac{1 - \varepsilon_s \exp[a_s + b]}{1 - \varepsilon_s \exp[a_s - b]} \cdot \frac{1 - \varepsilon_s \exp[-(a_{\bar{s}} + b)]}{1 - \varepsilon_s \exp[-(a_{\bar{s}} - b)]}\right] \tag{5.39}$$

where

$$a_s \equiv \frac{\gamma}{2\sqrt{s}T}(s + m_s^2 - m_{\bar{s}}^2) \ , \qquad a_{\bar{s}} \equiv \frac{\gamma}{2\sqrt{s}T}(s + m_{\bar{s}}^2 - m_s^2) \ ,$$

$$b \equiv \frac{|p_s|\sqrt{\gamma^2 - 1}}{T} = \frac{\sqrt{\gamma^2 - 1}}{T} \frac{\sqrt{s - (m_s - m_{\bar{s}})^2}\sqrt{s - (m_s + m_{\bar{s}})^2}}{2\sqrt{s}} \ . \tag{5.40}$$

Eq(5.34) and Eq(5.33, 5.35, 5.36) are one of the central results which I will be using. It is worth stressing that these results only use the requirements set by freeze-in. The equations therefore hold independently of whether either of the particles are self-conjugate or not. It does also not put any constraints on the masses, other than $m_\chi = m_{\bar{\chi}}$. It is worth noting that Eq.(5.33) becomes slightly simpler with $m_s = m_{\bar{s}}$. The in-medium effects due to quantum statistics reside in the G-factor introduced in Eq.(5.33), setting $G = 1$ will make it such that the integral over γ in Eq.(5.34) can be performed analytically, leading to the familiar result given by Eq.(4.22). The fact that the Boltzmann-equation can be written on the form in Eq.(5.14) which stresses the analogy to the production term for freeze-out, and at the same time takes into account both relativistic effects and the quantum statistical factors, is clearly advantageous. Both from a numerical implementation point of view, but also - as we will see in section 8 - allows for a treatment of DM production from the thermal heat bath through an off-shell Higgs resonance, which more easily takes into account higher-order correction than is achieved with the standard formulation.

5.2.2 $1 \to 2$ Processes

For completeness I will also include the case where heavy thermal sector bath particles decay into FIMPs, i.e. the process $a \to \chi\bar{\chi}$, where a is the thermal sector bath particle. This process is seen to correspond to the $2 \to 2$ process where the particle a is an almost on-shell mediator, see appendix B. Even though the process has been accounted for

in the discussion above, I will show explicitly what the abundance for such a process is. I begin by looking at the Boltzmann equation describing the process, which from Eq.(5.6) is seen to be

$$\dot{n}_\chi + 3Hn_\chi = \int d\Pi_a d\Pi_\chi d\Pi_{\bar{\chi}} f_a |\mathcal{M}|^2_{a\to\chi\bar{\chi}} (2\pi)^4 \delta^4(p_a - p_\chi - p_{\bar{\chi}}) \ . \tag{5.41}$$

We can use that the decay rate for a is

$$\Gamma_{a\to\chi\bar{\chi}} = \frac{N_\chi^{-1}}{2m_a} \int \overline{|\mathcal{M}_{a\to\chi\chi}|}^2 (2\pi)^4 \delta^4(p_a - p_\chi - p_{\bar{\chi}}) d\Pi_\chi d\Pi_\chi \ , \tag{5.42}$$

where $N_\chi = 1$ if $\chi \neq \bar{\chi}$ and $N_\chi = 2$ if $\chi = \bar{\chi}$. I want to note that I have not used inverse-decays in this section, although that would also give the correct result just as it does for the $2 \to 2$ case. The Boltzmann equation now becomes

$$\dot{n}_\chi + 3Hn_\chi = 2m_a g_a N_\chi \Gamma_{a\to\chi\bar{\chi}} \int d\Pi_a f_a \ . \tag{5.43}$$

We can perform this integral in the same manner as we did in the $2 \to 2$ case. We have

$$\frac{d^3\mathbf{p}}{2E_a} = \delta^2(E^2 - m_a^2) \sinh^2\eta \ E_a^3 \ dE_a \ d\eta \ d\Omega \ , \tag{5.44}$$

we find

$$\dot{n}_\chi + 3Hn_\chi = \frac{m_a^3 g_a N_\chi}{2\pi} \Gamma_{a\to\chi\bar{\chi}} \int_1^\infty dx \frac{\sqrt{x^2-1}}{e^{\frac{m_a}{T}x} - \varepsilon_a} \ . \tag{5.45}$$

For the Maxwell-Boltzmann case ($\varepsilon_a = 0$), we see that we get the known result [5]

$$\dot{n}_\chi + 3Hn_\chi = \frac{m_a^2 T g_a N_\chi}{2\pi} \Gamma_{a\to\chi\bar{\chi}} K_1(m_a/T) \ . \tag{5.46}$$

Which means that the $1 \to 2$ abundance is given by

$$Y_{1\to2} = \frac{g_a}{2\pi^2} m_a^2 N_\chi \Gamma_{a\to\chi\bar{\chi}} \int_{T_0}^{T_R} \frac{dT}{\overline{H}s(T)} K_1(m_a/T) \ . \tag{5.47}$$

We see that we can easily include the quantum effects for Y, i.e. using Fermi-Dirac or Bose-Einstein distribution for Y, by doing the replacement

$$K_1(m_a/T) \to \frac{m_a}{T} \int_1^\infty dx \frac{\sqrt{x^2-1}}{e^{\frac{m_a}{T}} - \varepsilon_a} \ . \tag{5.48}$$

The fact that the $1 \to 2$ matches the $2 \to 2$ process when the Narrow-Width approximation is used on the mediator when quantum statistics is neglected is discussed in appendix B. There is no need to use the trick used in the previous section, since Eq.(5.45) is simple enough to solve numerically and the same higher-order correction calculations have to be calculated in both methods.

To summarize, since the $1 \to 2$ process corresponds to the $2 \to 2$ process in the special case where we have an s-channel resonance, I will use the abundance calculated using the $2 \to 2$ process going forward. The $2 \to 2$ process is fully described by the Boltzmann equation given by Eq.(5.14), including in-medium effects, which will be very beneficial when I will apply it to the scalar-singlet model in section 8. I will now introduce finite temperature effects and how this affects phase transitions.

Part III

Thermal and Higher Order Effects

Chapter 6

Finite Temperature Effects

One of the attractive features with freeze-out is that for renormalisable couplings, freeze-out generally occurs when $m_\chi/T \simeq 10, ..., 30$, see figure 4.9. This means that for a WIMP mass $m_\chi \sim 200\,\text{GeV}$, freeze-out happens when $T \simeq 20...7\,\text{GeV}$. This is well after electroweak symmetry breaking (EWSB) which occurs when $T = T_{\text{EW}} \approx 163\,\text{GeV}$. Since the visible sector and DM were in thermal equilibrium until it decouples, the abundance is independent of the thermal history of the early universe and the effect from the electroweak phase transition (EWPT) on the abundance is thus erased. This is why freeze-out calculations only use cross sections calculated assuming broken electroweak (EW) symmetry, unless multi-TeV DM masses are assumed. For freeze-in, the yield produced via a Yukawa interaction is usually dominated in the epoch $m/T \sim 2-5$, where m is the relevant mass scale in the DM production process [5], see figure 5.1. For freeze-it it is no longer the case that the abundance is independent of the thermal history of the early universe since the visible sector and DM is not in thermal equilibrium. For a freeze-in mass scale of $m \sim 200\,\text{GeV}$, this gives the corresponding freeze-in temperature $T \sim 100...40\,\text{GeV}$, which is why we want to include the fact that electroweak symmetry is unbroken when $T \gtrsim 163\,\text{GeV}$ and the contribution to the DM abundance coming from thermal effects before EWSB. This will be seen to have a significant effect on the relic abundance.

In this section I will give a review on how to include finite temperature effects in field theory. The application of these effects will be discussed in section 8. For a more thorough review see Ref. [112]. I will start by going through the zero-temperature description, with an emphasis on applying it to the SM and the calculation of the effective Higgs potential. I will then in section 6.2, show how the thermal contributions are added and how they modify the effective Higgs potential. Finally, I will show how this affects phase transitions, mainly focusing on the electroweak phase transition (EWPT), but I will also describe the QCD phase transition.

6.1 Zero-Temperature Description

When we want to look at phase transitions in quantum field theories, it is the effective potential V_{eff} we have to study. The effective potential for a theory with a scalar field ϕ is defined in terms of the *effective action*. To define the effective action, I have to briefly review generating functionals. A theory described by the Lagrangian density $\mathcal{L}\{\phi(x)\}$ have the following generating functional (using the path integral representation)

$$Z[j] \equiv \int d\phi \exp(i(S[\phi] + \phi j)) \tag{6.1}$$

where $S[\phi] = \int d^4x \mathcal{L}\{\phi(x)\}$ is the usual action and $\phi j \equiv \int d^4x \phi(x) j(x)$. The connected generating functional $W[j]$ is then defined by

$$Z[j] \equiv \exp(iW[j]) \ . \tag{6.2}$$

We can now define the effective action by Legendre transforming $W[j]$ in terms of

$$\bar{\phi}(x) \equiv \frac{\delta W[j]}{\delta j(x)} \tag{6.3}$$

which is

$$\Gamma[\bar{\phi}] = W[j] - \int d^4x \bar{\phi}(x) j(x) \ . \tag{6.4}$$

The effective action can be expanded in terms of powers of $\bar{\phi}$

$$\Gamma[\bar{\phi}] = \sum_{n=0}^{\infty} \frac{1}{n!} \int d^4x_1 ... d^4x_n \phi(\bar{x}_1) ... \phi(\bar{x}_n) \Gamma^{(n)}(x_1, ..., x_n) \ . \tag{6.5}$$

where $i\Gamma^{(n)}$ are the one-particle irreducible (1PI) Green's functions

$$i\Gamma^{(n)}(x_1, ..., x_n) \equiv \frac{i\delta^n \Gamma[\bar{\phi}]}{\delta\bar{\phi}(x_1) ... \delta\bar{\phi}(x_n)} = \langle \phi(x_1) ... \phi(x_n) \rangle_{1PI} \tag{6.6}$$

For a transnational invariant theory, we can use that

$$\bar{\phi} = \phi_c \tag{6.7}$$

since $\bar{\phi}$ is constant. ϕ_c is now seen as the classical background field. The effective potential can now be defined

$$\Gamma[\phi_c] = -\int d^4x V_{\text{eff}}(\phi_c) \ , \tag{6.8}$$

which can be written in terms of the 1PI Green's functions

$$V_{\text{eff}}(\phi_c) = -\sum_{n=0}^{\infty} \frac{1}{n!} \phi_c^n \Gamma^{(n)}(p_i = 0) \tag{6.9}$$

where $\Gamma^{(n)}(p_1, ..., p_n)$ is the Fourier transformed $\Gamma^{(n)}(x)$. For more details regarding $\Gamma[\phi_c]$ and ϕ_c refer to Ref. [102, p. 364] or Ref. [113, p. 733].

I want to find the effective potential for the SM of electroweak interactions. This will be found by using the spin-zero $SU(2)$ doublet of the SM, which is

$$\Phi = \begin{pmatrix} \chi_1 + i\chi_2 \\ \frac{\phi_c + h + i\chi_3}{\sqrt{2}} \end{pmatrix} , \tag{6.10}$$

where h is the real Higgs field, ϕ_c is the real constant background and χ_a $(a = 1, 2, 3)$ are the three Goldstone bosons. The potential for the SM is

$$V_0 = -m^2 \Phi^\dagger \Phi + |\Phi^\dagger \Phi|^2 \tag{6.11}$$

which in terms of the background field is

$$V_0(\phi_c) = -\frac{m^2}{2}\phi_c^2 + \frac{\lambda}{4}\phi_c^4 \ . \tag{6.12}$$

The vacuum expectation value (vev) is found by minimizing V_0

$$v_0^2 = \frac{m^2}{\lambda} \ , \tag{6.13}$$

where both λ and m^2 are positive. The mass of the Higgs at tree-level is thus

$$m_h^2(\phi_c) = \frac{d^2 V_0(\phi_c)}{d\phi_c^2} = 3\lambda\phi_c^2 - m^2 \ , \tag{6.14}$$

which corresponds to the well-known result $m_h^2(v) = 2\lambda v^2 = 2m^2$. The other particles contributing to the one-loop effective potential are the $W^\pm$ and Z gauge bosons, the Goldstone bosons, and the top quark (the contribution from the leptons and the other quarks is negligible due to their small Yukawa couplings). Their tree-level masses are

$$\begin{aligned} m_W^2(\phi_c) &= \frac{g^2}{4}\phi_c^2 \ , \\ m_Z^2(\phi_c) &= \frac{g^2 + g'^2}{4}\phi_c^2 \ , \\ m_\chi^2(\phi_c) &= \lambda\phi_c - m^2 \ , \\ m_t^2(\phi_c) &= \frac{y_t^2}{2}\phi_c^2 \ , \end{aligned} \tag{6.15}$$

where g and g' are the $SU(2)$ and $U(1)_Y$ couplings, respectively, and y_t is the Yukawa coupling for the top quark. The one-loop contribution to the tree-level potential is the sum of all the 1PI diagrams with one loop and zero external momenta. This have to be calculated for both the scalar (real and complex), fermion and gauge boson case. I will give the argument for the one-loop contribution coming from real scalars, but the

arguments for the fermion and gauge boson case are very similar and I refer the reader to see Ref. [112] for these calculations.

The potential for a model with one self-interacting real scalar field is given by

$$V_0(\phi) = \frac{m^2}{2}\phi^2 + \frac{\lambda}{4!}\phi^4 \ . \tag{6.16}$$

The Lagrangian describing this model is then just $\mathcal{L} = \partial^\mu\phi\partial_\mu\phi - V_0(\phi)$. Since we have no three-scalar interactions all the diagrams contributing to the one-loop correction to V_0 will contain one loop with n vertices on the loop, each vertex will contribute two external legs. n goes from 1 to ∞ and all the diagrams must be summed. For the diagram with n vertices, we will have n propagators between the vertices, which contribute the factor $\frac{i^n}{(p^2-m^2+i\epsilon)^n}$. We need the factor ϕ_c^{2n} due to the $2n$ external lines and for each vertex we need the factor $-i\lambda/2$, where the $1/2$ factor is due to the fact that exchanging the external lines gives the same diagram. The last part we need is symmetry factors, we get a factor $1/n$ because of the discrete rotational symmetry ($\mathbb{Z}_n$) and a factor $1/2$ because of the $\mathbb{Z}_2$ reflection symmetry. Finally, we put everything together and integrate over the loop momentum:

$$\begin{aligned} V_1(\phi_c) &= i\sum_{n=1}^{\infty}\int\frac{d^4p}{(2\pi)^4}\frac{1}{2n}\left[\frac{\lambda\phi_c^2/2}{p^2-m^2+i\epsilon}\right]^n \\ &= -\frac{i}{2}\int\frac{d^4p}{(2\pi)^4}\log\left[1-\frac{\lambda\phi_c^2/2}{p^2-m^2+i\epsilon}\right] \end{aligned} \tag{6.17}$$

where the factor i comes from Eq.(6.6). Wick rotating gives

$$V_1(\phi_c) = \frac{1}{2}\int\frac{d^4p_E}{(2\pi)^4}\log\left[1-\frac{\lambda\phi_c^2/2}{p_E^2+m^2+i\epsilon}\right] \ . \tag{6.18}$$

Using that the shifted mass is

$$m^2(\phi_c) \equiv \frac{d^2V_0(\phi_c)}{d\phi_c^2} = m^2 + \frac{\lambda}{2}\phi_c^2 \tag{6.19}$$

means that the one-loop correction to the effective potential is

$$V_1(\phi_c) = \frac{1}{2}\int\frac{d^4p}{(2\pi)^4}\log[p^2+m^2(\phi_c)] \ , \tag{6.20}$$

where I have dropped the term that is independent of ϕ_c and dropped the index E on the Euclidean momentum.

The calculation done above is quite easily done for complex scalars, fermions, and gauge bosons. Applying the result to the SM, we find that the one-loop correction to the effective potential can be written as [112]

$$V_1(\phi_c) = \sum_{i=W,Z,h,\chi,t}\varepsilon_i n_i\ \frac{1}{2}\int\frac{d^4p_i}{(2\pi)^4}\log[p_i^2+m_i^2(\phi_c)] \ , \tag{6.21}$$

where we are working in the Landau gauge, $\varepsilon_i = 1$ (-1) if i is a boson (fermion) and n_i correspond to the total degrees of freedom for a particle species ($n_W = 6$, $n_Z = 3$, $n_h = 1$, $n_\chi = 1$ and $n_t = 12$). Using cut-off regularization to regularise the integrals together with the renormalization conditions which impose that the minimum of the potential is at $\phi_c = v$ and that the Higgs mass is given by its tree-level value, gives the effective potential[1] [114]

$$V_1(\phi_c) = \frac{1}{64\pi^2} \sum_{i=W,Z,t} \varepsilon_i n_i \left[m_i^4(\phi_c) \left(\log \frac{m_i^2(\phi_c)}{m_i^2(v_0)} - \frac{3}{2} \right) + 2 m_i^2(v_0) m_i^2(\phi_c) \right] \tag{6.22}$$

plus, terms that are independent of ϕ_c. We have now the expression for the effective potential at zero temperature to one-loop order

$$V_{\text{eff}}(\phi_c) = V_0(\phi_c) + V_1(\phi_c) \ . \tag{6.23}$$

6.2 Thermal Contributions

I will now include the finite temperature effects in the effective potential. This is done by computing the Feynman diagrams using thermal quantum field theory, for a review see Ref. [112, Sec. 2]. The effective potential at tree-level becomes the same as for the zero-temperature case, while the one-loop correction has a temperature dependence. Calculating the thermal one-loop correction to V_{eff} for the real-scalar example means that we have to use the Feynman-rules from finite temperature field theory. In the imaginary time formalism, we have that the scalar propagator is given by $i(p^2 - m^2)$ where $p^\mu = [i\omega_n, \vec{p}]$ and $\omega_n \equiv 2n\pi T$ are the Matsubara frequencies for bosons. For loops one has to use $iT \sum_{n=-\infty}^{\infty} \int \frac{d^3p}{(2\pi)^3}$ (for all the Feynman-rules, see Eq.(147) in Ref. [112]). This means that Eq(6.20) turns into

$$V_1^T(\phi_c) = \frac{T}{2} \sum_{n=-\infty}^{\infty} \int \frac{d^3p}{(2\pi)^3} \log(\omega_n^2 + \omega^2) \tag{6.24}$$

where $\omega^2 = \vec{p}^2 + m^2(\phi_c)$. The sum over n is divergent, but the divergent part is independent of ϕ_c. By discarding the ω independent terms one finds that the ϕ_c dependent part of the one-loop correction to the potential

$$V_1^T(\phi_c) = \int \frac{d^3p}{(2\pi)^3} \left[\frac{\omega}{2} + T \log(1 - e^{-\frac{\omega}{T}}) \right] \ . \tag{6.25}$$

[1] The divergence that would have occurred in Eq.(6.22) due to the Goldstone bosons (which is seen by setting $m_\chi(v) = 0$), comes from the fact that Goldstone contribution gives an infinite running of the Higgs mass between zero Euclidean momentum and $p^2 = m_h^2$. We can neglect this contribution and the Higgs contribution because the Higgs boson self-coupling is small [114].

The one-loop corrections to the SM effective potential is found by calculating the one-loop correction for fermions and bosons as well, this can be found in section 3 in Ref. [112]. Applying it to Eq.(6.21) gives us

$$V_1^T(\phi_c) = \sum_{i=W,Z,t} \varepsilon_i n_i \int \frac{d^3p_i}{(2\pi)^3} \left[\frac{\omega_i}{2} + T\log(1-\varepsilon_i e^{-\frac{\omega_i}{T}})\right] \ , \tag{6.26}$$

where $\omega_i^2 = \vec{p_i}^2 + m^2(\phi_c)$. Using the identity[2]

$$\frac{1}{2}\int \frac{d^3p}{(2\pi)^3}\omega = \frac{1}{2}\int \frac{d^4p_E}{(2\pi)^4}\log[p_E^2 + m^2(\phi_c)] \ , \tag{6.27}$$

we can rewrite Eq.(6.26) to get

$$V_1^T(\phi_c) = V_0(\phi_c) + \Delta V(\phi_c, T) \ , \tag{6.28}$$

where $V_0(\phi_c)$ is the zero-temperature one-loop correction given by Eq.(6.22) and the temperature dependent part is

$$\Delta V(\phi_c, T) = T\sum_{i=W,Z,t} \varepsilon_i n_i \int \frac{d^3p_i}{(2\pi)^3}\log\left[1-\varepsilon_i e^{-\frac{\omega_i}{T}}\right] \tag{6.29}$$

$$= \frac{T^4}{2\pi^2}\sum_{i=W,Z,t} \varepsilon_i n_i \int_0^\infty dx\ x^2 \log\left[1-\varepsilon_i e^{-\sqrt{x^2+\frac{m^2}{T^2}}}\right]$$

$$= \frac{T^4}{2\pi^2}\sum_{i=W,Z} \varepsilon_i n_i J_B(m_i^2/T^2) - \frac{T^4}{2\pi^2} n_t J_F(m_t^2/T^2), \tag{6.30}$$

where the thermal function for bosons is

$$J_B(m^2/T^2) = \int_0^\infty dx\ x^2 \log\left[1-e^{-\sqrt{x^2+\frac{m^2}{T^2}}}\right] \ , \tag{6.31}$$

and the thermal function for fermions is

$$J_F(m^2/T^2) = \int_0^\infty dx\ x^2 \log\left[1+e^{-\sqrt{x^2+\frac{m^2}{T^2}}}\right] \ . \tag{6.32}$$

The effective potential including finite temperature corrections is thus given by

$$V_{\text{eff}} = V_0(\phi_c) + V_1(\phi_c) + \Delta V(\phi_c, T) \tag{6.33}$$

For $m/T \ll 1$, J_B has the expansion:

$$J_B(m^2/T^2) = -\frac{\pi^4}{45} + \frac{\pi^2}{12}\frac{m^2}{T^2} - \frac{\pi}{6}\left(\frac{m^2}{T^2}\right)^{3/2} - \frac{1}{32}\frac{m^4}{T^4}\log\frac{m^2}{a_b T^2} \tag{6.34}$$

$$- 2\pi^{7/2}\sum_{\ell=1}^{\infty}(-1)^\ell \frac{\zeta(2\ell+1)}{(\ell+1)!}\Gamma\left(\ell+\frac{1}{2}\right)\left(\frac{m^2}{4\pi^2T^2}\right)^{\ell+2} \ ,$$

[2]Found by Wick rotating and taking the derivative with respect to ω. Then integrating over p_0 and closing the integration interval $(-\infty, \infty)$ in the complex plane picks up the pole at $p_0 = -\sqrt{\omega^2 - i\epsilon}$, which gives the residue $1/2\omega$.

where $a_b = 16\pi^2 \exp(3/2 - 2\gamma_E)$, γ_E is the Euler–Mascheroni constant, ζ is the Riemann ζ-function and Γ is the Gamma function. The corresponding high-temperature expansion for J_F is:

$$\begin{aligned} J_F(m^2/T^2) =& \frac{7\pi^4}{360} - \frac{\pi^2}{24}\frac{m^2}{T^2} - \frac{1}{32}\frac{m^4}{T^4}\log\frac{m^2}{a_f T^2} \\ & - \frac{\pi^{7/2}}{4}\sum_{\ell=1}^{\infty}(-1)^\ell \frac{\zeta(2\ell+1)}{(\ell+1)!}(1-2^{-2\ell-1})\Gamma\left(\ell+\frac{1}{2}\right)\left(\frac{m^2}{\pi^2 T^2}\right)^{\ell+2} , \end{aligned} \tag{6.35}$$

where $a_f = \pi^2 \exp(3/2 - 2\gamma_E)$. Using these expansions, we can rewrite the effective potential at high temperatures to one-loop order using Eq.(6.33):

$$V_{\rm eff}^{\rm High-T}(\phi_c, T) = D(T^2 - T_0^2)\phi_c^2 - ET\phi_c^3 + \frac{\lambda(T)}{4}\phi_c^4 , \tag{6.36}$$

with the coefficients

$$D = \frac{2m_W^2 + m_Z^2 + 2m_t^2}{8v_0^2} \simeq 1.7 \times 10^{-1} , \tag{6.37}$$

$$E = \frac{2m_W^3 + m_Z^3}{4\pi v_0^3} \simeq 9.4 \times 10^{-3} , \tag{6.38}$$

$$B = \frac{3}{64\pi^2 v_0^4}(2m_W^4 + m_Z^4 - 4m_t^4) \simeq -4.5 \times 10^{-4} , \tag{6.39}$$

$$T_0^2 = \frac{m_h^2 - 8Bv_0^2}{4D} \Rightarrow T_0 \simeq 163\,{\rm GeV} , \tag{6.40}$$

$$\lambda(T) = \lambda - \frac{3}{16\pi^2 v_0^4}\left(2m_W^4 \log\frac{m_W^2}{A_B T^2} + m_Z^4 \log\frac{m_Z^2}{A_B T^2} - 4m_t^4 \log\frac{m_t^2}{A_F T^2}\right) , \tag{6.41}$$

where $\log A_B = \log a_b - 3/2$, $\log A_F = \log a_f - 3/2$ and all the masses are at zero-temperature. The minimum of $V_{\rm eff}^{\rm High-T}$ at high temperatures is given by $\phi_c = 0$, since $T^2 > T_0^2$. This means that the complex Higgs has a thermal mass given by

$$m_H^2(T) = \left.\frac{d^2 V_{\rm eff}^{\rm High-T}}{d\phi_c^2}\right|_{\phi_c=0} = 2D(T^2 - T_0^2) , \tag{6.42}$$

which will be important to use for temperatures higher than the EWPT temperature. In the next section I will discuss the effect of low temperatures on the effective potential and use Eq.(6.36) to discuss the EWPT.

6.3 Phase transitions

In cosmology, phase transitions are essential. The temperature effects of the electroweak phase transition, which were first realized by Kirzhnits [115], but also

studied by various others [116–122], can be essential in describing the baryon asymmetry of the Universe[3], which can be generated by a strong first-order phase transition [124]. It can also, as I will show in chapter 8, be important for the DM abundance when it is generated by the freeze-in mechanism. At zero-temperature we know that the potential is minimized when $\langle\phi\rangle = v$, where $v \sim 246\,\text{GeV}$. However, the universe has not always been cold or empty, many models of reheating after inflation predict temperatures high enough to restore electroweak symmetry. This can be seen in Eq.(6.36) when the minimum is given by $\phi_c = 0$; this phenomenon is called **symmetry restoration** at high temperatures. As the universe cools down the minimum will change from $\phi_c = 0$ to $\phi_c \neq 0$. This happens at the *critical temperature* $T_c = T_{\text{EW}}$, and due to the fact that $E \neq 0$ given by Eq.(6.38), the strength of the phase transition is [112]

$$\frac{\phi_c}{T_c} = \frac{2E}{\lambda} \sim \frac{2000(\,\text{GeV}^2)}{m_h^2}\,. \tag{6.43}$$

With a Higgs mass of 125 GeV, one finds that the SM has a very weak first order phase transition since $\phi_c/T_{\text{EW}} \sim 0.1$. Baryon asymmetry needs a strong first-order phase transition, a lot of work has therefore gone into looking at models that boost the strength of the electroweak phase transition, see e.g. Ref. [125] and Ref. [124].

After the phase transition we would like to have expressions for the thermal mass and vev. The numerical and analytical high temperature expansion value for the Higgs mass is shown in figure 6.1. It is natural to try setting the mass $m_h(T)^2 = -2m_H(T)^2$, this is displayed by the red line. This however can be seen to predict a wrong zero-temperature Higgs mass; this is because the high-energy expansion no longer works at these temperatures, which can be seen from $\lambda(T)$ given by Eq.(6.41). $\lambda(T)$ diverge logarithmically as $T < m_t$. This problem can also be seen for the thermal vev, which can be seen as a function of T in figure 6.2 together with a plot of the effective potential for various temperatures. The breaking down of the high-temperature expansion of the effective potential is seen to give a vev that is too small. In order to get the correct result, I therefore settled on calculating the Higgs mass and the thermal vev numerically by minimising the effective potential and calculating:

$$m_h^2(T) = \left.\frac{d^2V_{\text{eff}}}{d\phi_c^2}\right|_{\phi_c=v(T)}\,.$$

This is the blue line in figure 6.1. I then tabulated the results and I will use these for the rest of this thesis. From the numerical calculations we find that the critical temperature for the SM is $T_{\text{EW}} \simeq 163.2\,\text{GeV}$. We will see in chapter 8 that these thermal effects can have an important effect when the DM abundance is produced by the freeze-in mechanism.

Another phase transition we are interested in is the QCD phase transition, which occurs when the universe has cooled to a temperature of roughly 154 MeV [126]. The

[3]This does not apply to the SM. It requires a very light Higgs boson (<42 GeV) and more CP violation than is observed [123].

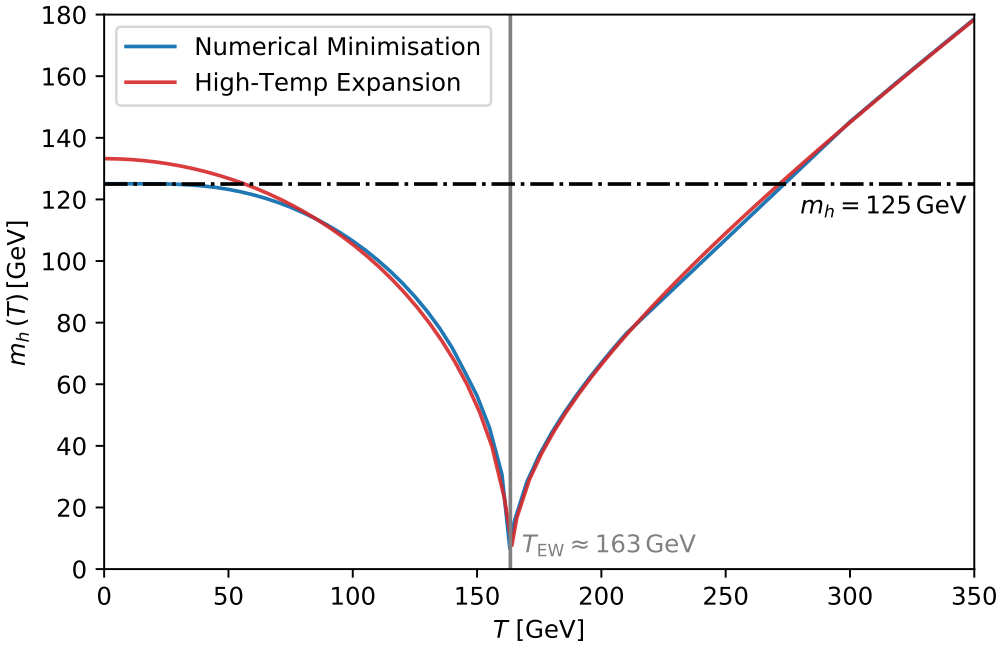

Figure 6.1: The Higgs mass as a function of temperature solved numerically solved (blue) and analytically using $m_h = \sqrt{4(T_0^2 - T^2)}$ (red). The black dash-dotted line shows the correct zero temperature Higgs mass and the grey solid line shows then $T = T_{\mathrm{EW}} \simeq 163\,\mathrm{GeV}$.

running of the strong coupling constant g_s, implies that at high temperatures g_s is small enough to treat the system, which is a quark-gluon plasma, perturbatively. However, as the temperature drops, g_s increases in strength and quarks and gluons will experience colour-confinement and hadronise, which means that the perturbative description will no longer work. In order to describe the non-perturbative effects, lattice QCD is often used. An alternative method is to use chiral perturbation theory (ChPT), which is successful in describing hadron interactions in the non-perturbative regime of the strong interaction. ChPT is an effective field theory that uses the approximate chiral symmetry of QCD (and CP-symmetry) in order to construct a Lagrangian that allows one to study the low-energy behaviour in QCD, e.g. interactions between pions, nucleons, kaons and other mesons. I will in the next chapter use results from ChPT for the off-shell decay width of the SM Higgs boson, in order to use the decay width into mesons when the QCD phase transition has happened.

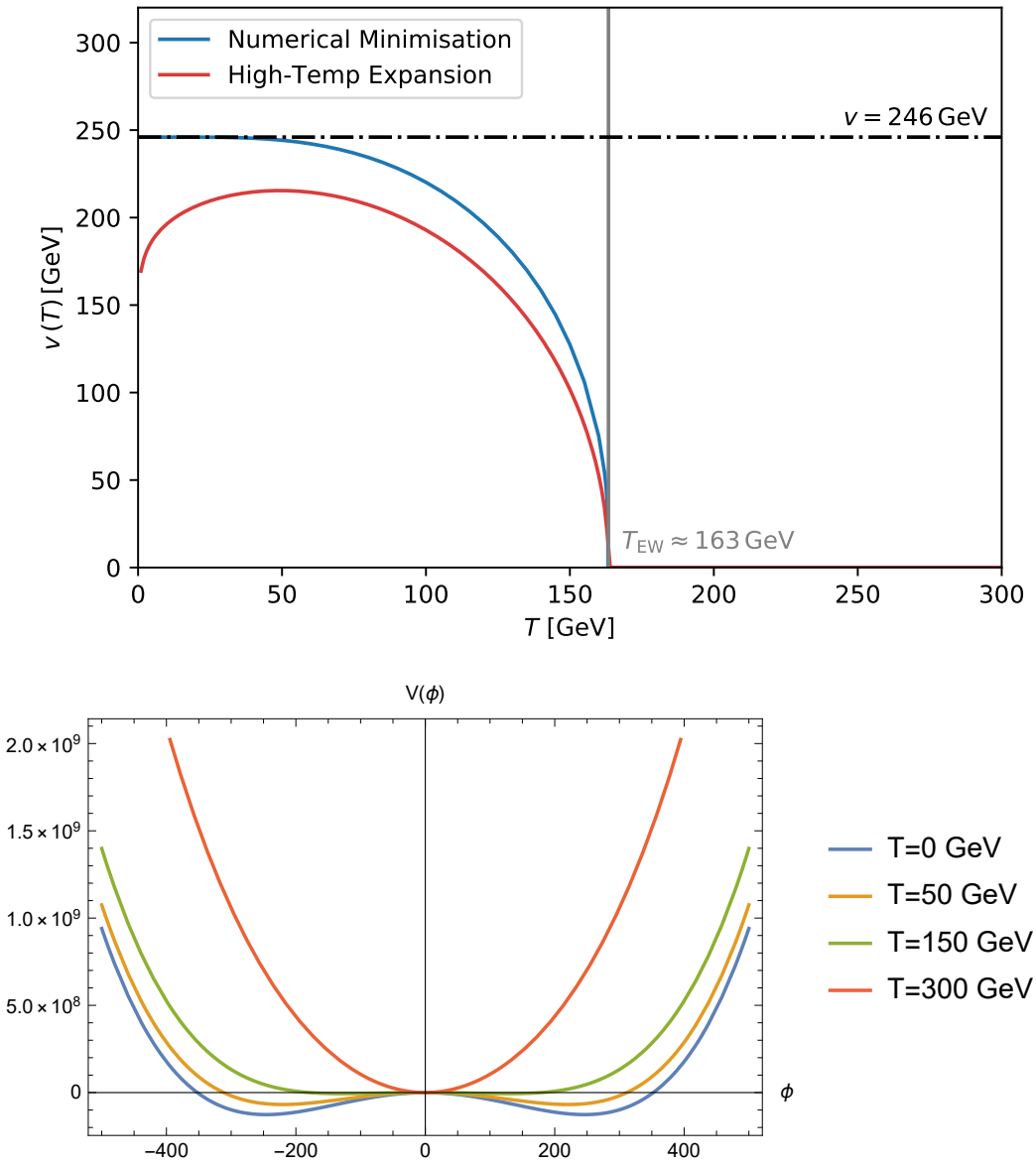

Figure 6.2: *Top panel:* The Higgs vev as a function of temperature. The red line shows the approximation in the high-temperature limit given by Eq.(6.36). The blue line shows the numerical solution to Eq.(6.33). The black dash-dotted line shows the correct zero temperature vev and the grey line marks $T = T_{\mathrm{EW}}$. *Bottom panel:* The effective potential given by Eq.(6.33) is plotted for the four temperatures $T = 0\,\mathrm{GeV}$ (blue), $50\,\mathrm{GeV}$ (orange), $150\,\mathrm{GeV}$ (green) and $300\,\mathrm{GeV}$ (red).

Chapter 7

Off-shell Higgs decays

In this thesis I will consider a model where we add to the SM a new real singlet scalar S which is stabilised by a $\mathbb{Z}_2$ symmetry. This is the so-called scalar singlet model (a.k.a. the Silveira-Zee[6] model). This model will be introduced in chapter 8. However, in this chapter I will look at a broader class of DM models which the singlet scalar model is a part of. Specifically, models where annihilations into SM final states proceed via a SM Higgs boson in the s-channel, i.e. via an off-shell Higgs boson that can decay into the various SM fermions and gauge bosons. The total annihilation cross section is then proportional to the off-shell Higgs width $\Gamma_{h^*}(\sqrt{s}) \equiv \Gamma_h(m_h = \sqrt{s})$, where $\sqrt{s}$ denotes the centre-of-mass energy. It therefore becomes essential to have an accurate calculation of this off-shell width for arbitrary values of $\sqrt{s}$ and for finite temperatures. I will therefore begin with a discussion of the relevant decay modes and their implementation for $2\,\text{GeV} \lesssim \sqrt{s} \lesssim 1\,\text{TeV}$ at zero temperature. I then consider in section 7.2 the case where $\sqrt{s} \gg v(T)$ and how to avoid unitarity violation in this limit. Finally, I will in section 7.4 consider the case when $\sqrt{s} < 2\,\text{GeV}$ and how to include the QCD phase transition.

7.1 Relevant decay modes

In the mass range $2\,\text{GeV} \lesssim \sqrt{s} \lesssim 1\,\text{TeV}$ the off-shell Higgs decay width can be calculated perturbatively. The 1 TeV limit comes from the fact that the Higgs mass in the SM must be lower than 1 TeV in order to maintain perturbative unitarity [127], while the 2 GeV limit will be explained further down. Since the Higgs couplings to the SM particles are proportional to their masses, the relevant particles for decay and production processes are the gauge bosons W and Z, the top- and bottom quarks, the τ lepton and gluons, because of the top-contribution in the loop. The tree-level decay

widths into fermions are given by [128–130]

$$\Gamma(h^* \to f\bar{f}) = \frac{N_c m_f^2 \sqrt{s}}{8\pi v^2} \left(1 - \frac{4m_f^2}{s}\right)^{3/2} , \tag{7.1}$$

where $N_c = 1$ (3) for leptons (quarks). For decays into two gauge bosons $V = W, Z$ one finds[1]

$$\Gamma(h^* \to VV) = \frac{\sqrt{s}^3}{32v^2\pi} \delta_V \sqrt{1-4x}(1 - 4x + 12x^2) \tag{7.2}$$

with $\delta_W = 2$, $\delta_Z = 1$ and $x = m_V^2/s$. The leading-order decay width into gluons is given by [129, 130]

$$\Gamma(h^* \to gg) = \frac{\alpha_s^2(\sqrt{s})\sqrt{s}^3}{72v^2\,\pi^3} \left|\frac{3}{4} \sum_q A_{1/2}^h(\tau_q)\right|^2 , \tag{7.3}$$

where $\alpha_s(\sqrt{s})$ denotes the running strong coupling, $\tau_q = s/(4m_q^2)$ and

$$A_{1/2}^h(\tau) = 2(\tau + (\tau - 1)f(\tau))\tau^{-2} , \tag{7.4}$$

with

$$f(\tau) = \begin{cases} \arcsin^2 \sqrt{\tau} & \tau \leq 1 \\ -\frac{1}{4}\left(\log \frac{1+\sqrt{1-\tau^{-1}}}{1-\sqrt{1-\tau^{-1}}} - i\pi\right)^2 & \tau > 1 , \end{cases} \tag{7.5}$$

where $A_{1/2}^h(\tau)$ approaches unity for quark masses sufficiently above half the Higgs boson mass. The decay width into photons can be written in an analogous way but gives a negligible contribution to the total decay width, since $\Gamma(h^* \to \gamma\gamma)$ is proportional to the weak coupling $\alpha(\sqrt{s})$, not $\alpha_s(\sqrt{s})$. The QCD loop-corrections have been studied thoroughly. They are known up to NLO including the dependence on all the quark masses [129], while for the heavy quarks they are known up to N^{3}LO [131–133].

In practice, higher order corrections are non-negligible. This is particularly true for the case that $\sqrt{s} \gg v$ such that the decay into gauge bosons dominates and large NLO EW corrections arise from the real emission of additional gauge bosons [130]. To capture these and other effects, we use the tabulated decay widths from HDECAY [134] with a number of modifications as discussed below.

7.2 Unitarization

The off-shell decay width can, as mentioned in the previous section, not be calculated perturbatively for $\sqrt{s} \gg 1\,\text{TeV}$. This means that the width given by HDECAY becomes

[1] This expression does not play a role for an on-shell SM Higgs mass of 125 GeV, but it does for off-shell Higgs bosons splitting into on-shell W- or Z-boson pairs.

unphysical. In order to demonstrate this, I will consider a simple model where the SM Higgs boson is coupled to a real scalar singlet via

$$\mathcal{L} \supset \frac{\lambda_{hs}}{2}|H|^2 S^2 \,. \tag{7.6}$$

This is the same interaction as in the scalar singlet model which will be discussed in the next chapter. The annihilation cross section into two SM Higgs bosons is for $\sqrt{s} \gg v$ given at tree-level by [135]

$$\sigma_{SS\to hh} v_{\rm lab} = \frac{\lambda_{hs}^2}{32\pi s}\,, \tag{7.7}$$

where I use that $v_{\rm lab} = \sqrt{s(s-4m_S^2)}/(s-2m_S^2)$. The summed annihilation cross section into all the other SM particles X is given by [128]

$$\sigma_{SS\to XX} v_{\rm lab} = \frac{\lambda_{hs}^2 v_0^2}{\sqrt{s}} \left|D_h(s)\right|^2 \Gamma_{h^*}(\sqrt{s})\,., \tag{7.8}$$

where

$$\left|D_h(s)\right|^2 \equiv \frac{1}{(s-m_h^2)^2 + m_h^2\Gamma_h^2}\,. \tag{7.9}$$

An important remark is that Eq.(7.8) is valid to leading order in λ_{hs}, but the higher order corrections to the SM couplings are fully encapsulated in $\Gamma_{h^*}(\sqrt{s})$. This becomes an important effect when $\sqrt{s} \sim 2\,\text{TeV}$, see the dotted line in figure 7.1. However, as $\sqrt{s} \to \infty$ unitarity is broken because any cross section has to fall at least as fast as $1/s$ and thus Γ_{h^*} cannot grow faster than $s^{3/2}$. The tree-level widths given in Eq.(7.1), Eq.(7.2) and Eq.(7.3) does therefore not break unitarity. Using these expressions, one finds the expected result due to the Goldstone boson equivalence theorem, i.e. at $\sqrt{s} \gg m_H$ the amplitude for the longitudinal vector-boson scattering becomes equal to the amplitude for the scattering of the Goldstone bosons. The cross section in the $\sqrt{s} \to \infty$ limit after spontaneous electroweak symmetry breaking is given by Eq.(7.7), which agrees with the cross section obtained when the electroweak symmetry is restored. This is simply the cross section between S and the complex Higgs, which is given by

$$\sigma_{SS\to HH} v_{\rm cm} = \frac{\lambda_{hs}^2}{4\pi s}\sqrt{1-\frac{4m_H(T)^2}{s}}\,, \tag{7.10}$$

where $v_{\rm cm} = \sqrt{1-\frac{4m_H(T)^2}{s}}$ and m_H is the complex Higgs mass given by Eq.(6.42). The NLO EW corrections implemented in HDECAY will however make Γ_{h^*} grow too rapidly, which just means that the higher order corrections become more important to include for large $\sqrt{s}$ in order to restore unitarity. Instead of doing these calculations, I choose a phenomenological approach to ensure that my numerical implementation never violates unitarity. I follow the approach from Ref. [136], which ensures unitarity by replacing the on-shell Higgs decay width in the propagator by the off-shell Higgs decay width

$$\left|D_h(s)\right|^2 \equiv \frac{1}{(s-m_h^2)^2 + m_h^2\Gamma_{h^*}(\sqrt{s})^2}\,. \tag{7.11}$$

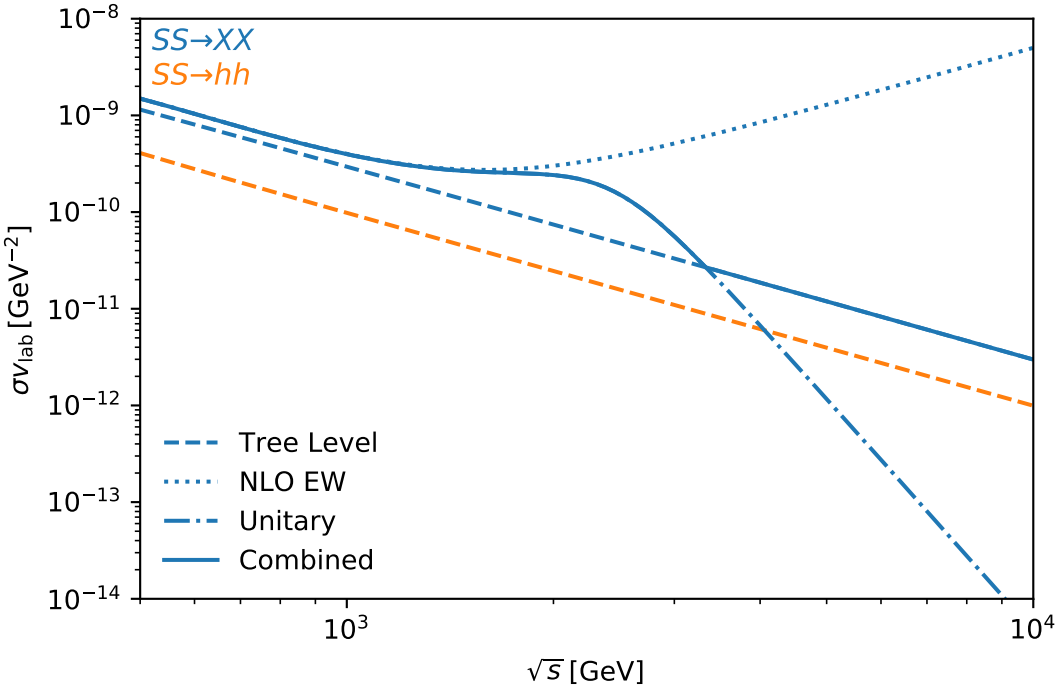

Figure 7.1: Annihilation cross section for the toy model introduced in eq. (7.6) for $\lambda_{hs} = 0.1$.

However, in the limit $\sqrt{s} \to \infty$ the cross section resulting from this description decreases faster than $1/s$, see the dash-dotted line in figure 7.1, which means that we do not get the same result as for the unbroken theory at large $\sqrt{s}$. The solution I implement is thus to combine the two in the following way

$$\sigma^{\text{total}}_{SS\to XX} = \max\left[\sigma^{\text{tree}}_{SS\to XX}, \sigma^{\text{unitary}}_{SS\to XX}\right]. \tag{7.12}$$

I believe that this description is as good as it gets without having to use the full NLO result for $T > T_{\text{EW}}$. The NLO results is non-trivial to calculate and beyond the scope of this thesis. I expect the same scaling for high energies as we have seen for the broken electroweak symmetry. However, the effects I am able to include is the NLO EW corrections for $\sqrt{s} \lesssim 2\,\text{TeV}$, there is no violation of unitarity for $\sqrt{s} \gtrsim 2\,\text{TeV}$ and lastly, the tree-level result in the unbroken theory is recovered in the limit $\sqrt{s} \to \infty$.

7.3 Finite-temperature corrections

The temperature dependence for the off-shell Higgs decay width is rather easily found. First I want to note that for temperatures above the QCD phase transition, the only

dimensionful quantity in the Standard Model is the Higgs vev, since all the masses $m_{f,V} \propto v$. It then follows immediately by dimensional analysis that the partial Higgs decay rate can be written as

$$\Gamma_{h^*}(\sqrt{s}) = vf(\sqrt{s}/v) \tag{7.13}$$

where $f(\sqrt{s}/v)$ is just the appropriate function depending on the dimensionless ratio $\sqrt{s}/v$. We can thus rescale the zero-temperature partial off-shell Higgs decay width

$$\Gamma_{h^*}(T, \sqrt{s}) = \Gamma_{h^*}\left(\sqrt{s}\frac{v_0}{v(T)}\right)\frac{v(T)}{v_0} \ . \tag{7.14}$$

We can again note that a large value of T, can give the same result as the zero temperature width with a large value of $\sqrt{s}$, this is due to the Goldstone boson equivalence theorem as discussed before. This means that even though the decay $h \to VV$ is not allowed before EWSB, it will have important effects coming from higher order corrections in the epoch right after EWSB, because the factor $\sqrt{s}v_0/v(T)$ diverges as $v(T) \to 0$. This means that the modification of the off-shell Higgs decay width described in the previous section is important to ensure unitarity close to the EWPT.

7.4 Chiral symmetry breaking

The last thermal effect I want to include is the QCD phase transition. I will use that the off-shell Higgs decay width calculated using HDECAY is no longer applicable when $\sqrt{s} < T_{\text{QCD}}$. I take that the temperature for the phase transition is $T_{\text{QCD}} \approx 154\,\text{MeV}$, which was found with Lattice QCD in Ref. [126]. For $T \gtrsim T_{\text{QCD}}$ Higgs boson decays into free quarks and gluons, but this is no longer the case when $T < T_{\text{QCD}}$, unless $\sqrt{s} \gtrsim 2\,\text{GeV}$. I follow Ref. [137] and [138], and assume that the perturbative description breaks down when $\sqrt{s} < 2\,\text{GeV}$. Once this happens, we can use chiral perturbation theory to calculate the off-shell decay width into QCD bound states. In essence, what is done is one uses the 3-flavor chiral Lagrangian in order to find the lowest order in the chiral expansion, while form factors that can be obtained from dispersion relations are used for higher order corrections. For a thorough review on how this is done I refer to Ref. [137]. The result of using ChPT for $T < T_{\text{QCD}}$ and $\sqrt{s} < 2\,\text{GeV}$ can be seen in figure 7.2. In the left panel the partial decay width of an off-shell SM Higgs boson into different final states is showed as a function of its mass at zero temperature below the $b\bar{b}$ threshold. For the mass above 2 GeV HDECAY is used to give the partial decay width to free quarks and gluons, while the tree-level result is given below $\sqrt{s} = 2\,\text{GeV}$. The contributing quarks will be the charm- and strange quarks since we are below the $b\bar{b}$ threshold. These are showed by the orange and purple lines, while the red line shows the gg contribution. The green line shows the decay rate to $\tau\tau$. As the mass becomes smaller than 2 GeV we enter the chiral perturbation theory regime if $T < T_{\text{QCD}}$. Above

T_{QCD} the Higgs still decays to free quarks and gluons, these partial decay widths are displayed as the dashed lines. The big jump in the dashed lines is because I switch to using tree-level results at 2 GeV, because there are a lot of uncertainties at these energies. The brown line indicates the total decay rate into hadrons given by the digitization of the result found in Ref. [137]. The dominant contribution until the resonance is coming from decay into pions ($\pi\pi$), while above the resonance it is the Kaon (KK) contribution that dominates. The effect by including decays to hadrons for $T < T_{\mathrm{QCD}}$ and $\sqrt{s} < 2\,\mathrm{GeV}$ can be seen in the thermally averaged cross section displayed in the right panel of figure 7.2. The solid lines show $\langle \sigma v \rangle$ when off-shell Higgs decays into hadrons for $T < T_{\mathrm{QCD}}$ and $\sqrt{s} < 2\,\mathrm{GeV}$, while the dashed lines show the result from assuming decays into free quarks and gluons. The grey line indicates the QCD phase transition, i.e. $T = T_{\mathrm{QCD}}$. The inclusion of the QCD phase transition can therefore be seen to give a smaller thermally averaged cross section for small temperatures than one would get if Higgs decays to free quarks and gluons were to be assumed. This is because for small T, we have that the decay width into hadrons drop to zero for $\sqrt{s} \sim 100\,\mathrm{MeV}$. This means that the annihilation channel would only have a non-zero contribution from the particles with energies larger than 100 MeV which would be in the tail of the distribution. Quarks and gluons will on the other hand not be Boltzmann suppressed until temperatures are much smaller, which explains the difference between the dotted and solid lines in the right-hand panel in figure 7.2. The discontinuity is not surprising since the total decay width before and after the QCD phase transition is completely independent so there is no reason that it should match at any $\sqrt{s}$, and it is conceivable that such a discontinuity can happen due to a first-order phase transition.

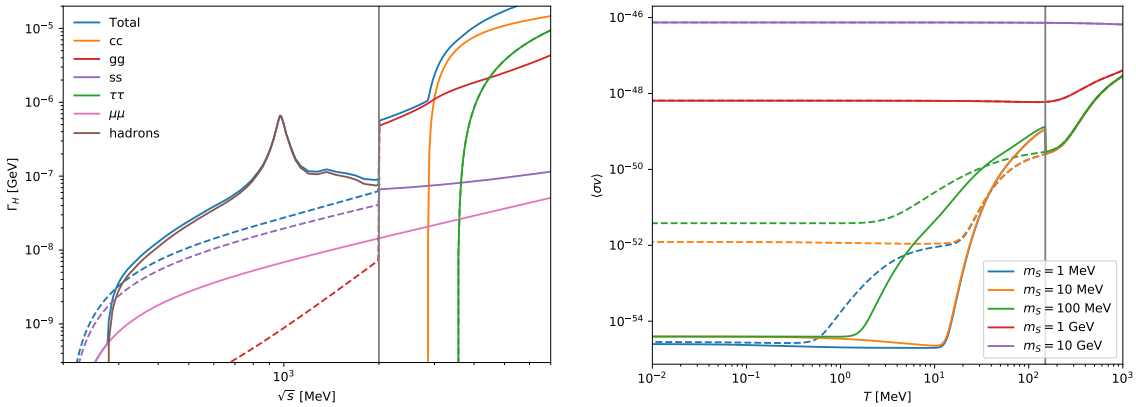

Figure 7.2: *Left panel.* Partial decay widths of an off-shell SM Higgs boson as a function of the off-shell mass, with final states as stated in the legend. For $\sqrt{s} > 2\,\text{GeV}$ I use the results from HDECAY [134] (based on the assumption of free quarks and gluons). In the chiral perturbation theory regime ($\sqrt{s} < 2\,\text{TeV}$ and $T < T_{\text{QCD}}$) the solid brown line indicate the total decay rate into hadrons (mostly pions and kaons) where I use the digitized results from Ref. [137] which have used chiral perturbation theory. Above 2 GeV the lines indicates the sum of the partial decay rates into gluons and all kinematically accessible quarks. The dotted lines show the tree-level decay rates into quarks and gluons which is used if $T > T_{\text{QCD}}$, which is the reason for the big jump. *Right panel.* Thermally averaged annihilation cross section as a function of temperature for the DM masses indicated in the legend. Solid lines display the result when the off-shell partial Higgs decay width into hadrons is used for $\sqrt{s} < 2\,\text{GeV}$ and $T < T_{\text{QCD}}$. The dashed lines are the result from assuming decay into free quarks even below the QCD phase transition (indicated by the vertical line).

Part IV

Freeze-in of a Scalar Singlet

Chapter 8

Freeze-in in the scalar singlet model

The formalism I have outlined in the previous chapters have been largely model independent. In Chapter 5 I outlined what the freeze-in mechanism is and how we can calculate the relic abundance for any model where freeze-in occurs. The finite-temperature methods introduced in chapter 6 can be applied to a variety of models, and it is easily extended to include more particles. Finally, in chapter 7 I outlined how beneficial it can be to use the off-shell Higgs decay width and how to implement it. I will now combine all these aspects and apply them to an attractive dark matter candidate, namely a scalar singlet coupled to the SM. This is one of the simplest extensions of the SM that can account for dark matter and it is called the **scalar singlet model** of Silveira and Zee [6]. I will start by introducing the model and its parameters. I will then in section 8.2 look at the case where the reheating temperature after inflation is a lot larger than the Higgs and scalar mass. I will show that the inclusion of higher order and thermal corrections in fact contribute to enhance and suppress the DM production, respectively. In section 8.3 I look at the case where the reheating temperature is smaller than the Higgs mass, which results in the abundance being produced by off-shell Higgs decays. I will here show that including the QCD phase transition and the fact that the Higgs decays into hadrons and not free quarks, in fact suppresses the DM production. I will then in section 8.4 discuss the results I have found.

8.1 The model

The scalar singlet model [6, 135, 139, 140] adds a new gauge-singlet real scalar field S to the Standard Model, which is stabilised by a $\mathbb{Z}_2$ symmetry. The most general renormalizable Lagrangian that describes this model is

$$\mathcal{L} = \mathcal{L}_{\text{SM}} + \frac{1}{2}\partial_\mu S \partial^\mu S - \frac{1}{2}\mu_S^2 S^2 - \frac{1}{2}\lambda_{hs} S^2 |H|^2 - \frac{1}{4}\lambda_s S^4 \,, \tag{8.1}$$

where H is the Standard Model Higgs doublet. The quartic self-coupling λ_s is largely irrelevant for phenomenology and will be irrelevant for my discussions. Most of the discussions regarding the scalar singlet model have assumed that the scalar is a WIMP, e.g. Ref. [135, 141, 142]. I will instead be interested in the case where λ_{hs} is small enough such that the scalar singlet never enters thermal equilibrium and its relic abundance is determined by the freeze-in mechanism.

After electroweak symmetry breaking, we can use that in unitary gauge $\sqrt{2}H^\dagger = (h, 0)$, where h is the real scalar Higgs. This means that the scalar potential takes the form [135]

$$V = \frac{\mu_S}{2}S^2 + \frac{\lambda_{hs}}{4}S^2h^2 + \frac{\lambda_s}{4}S^4 + \frac{\lambda_h}{4}(h^2 - v(T)^2)^2 \ , \tag{8.2}$$

where the real Higgs field is shifted by its vev. Since the potential must be bounded from below, we are provided with the following conditions

$$\lambda_s, \lambda_h \geq 0. \tag{8.3}$$

The desired symmetry breaking mechanism has that the electroweak gauge group is spontaneously broken, $\langle h \rangle \neq 0$, while the $\mathbb{Z}_2$ symmetry is not broken, i.e. $\langle S \rangle = 0$, since this ensures the longevity of S. This is found to be the case if and only if $\mu_s^2 + \frac{1}{2}\lambda_{hs}v^2 > 0$. The part of the potential that is dependent on S takes the form (where I have used that $h \to h + v(T)$)

$$V = \frac{1}{2}\left(\mu_S^2 + \frac{1}{2}\lambda_{hs}v(T)^2\right)S^2 + \frac{\lambda_{hs}}{2}v(T)S^2h + \frac{\lambda_{hs}}{4}S^2h^2 \ , \tag{8.4}$$

which means that the S-mass is given by

$$m_s(T) = \sqrt{\mu_S^2 + \frac{1}{2}\lambda_{hs}v(T)^2} \ . \tag{8.5}$$

The processes that contribute to the freeze-in yield are fundamentally different before and after the EWPT. In the former case, the only process that leads to the production of scalar singlets is $HH \to SS$. This regime is straight forward to solve for. The only relevant annihilation cross section is (in the CMS frame) given by Eq.(7.10).

After EWSB a multitude of SM states can contribute via processes like $XY \to h^* \to SS$. Since these processes are mediated exclusively by Higgs exchange in the s-channel, we can write the annihilation cross section as [128]

$$\sigma_{SS\to XY}v_{\text{lab}} = \frac{2\lambda_{hs}^2 v(T)^2}{\sqrt{s}}\left|D_h(s)\right|^2\Gamma_{h^*\to XY}(\sqrt{s}) \ . \tag{8.6}$$

where $|D_h(s)|$ is given by Eq.(7.9). Here $\Gamma_{h^*\to XY}(\sqrt{s})$ is the partial decay width of a Higgs with a mass $\sqrt{s}$ which was introduced in the previous chapter. This has as we know, the advantage of including higher order corrections for the SM couplings when

tables produced with HDECAY [134] as included in DarkSUSY [7] are used. The Higgs width Γ_h must include all Standard Model channels and $h \to SS$ if $m_s < m_h/2$. The contribution to the invisible Higgs decay width due to the scalar singlet is the channel $h \to SS$ [128]

$$\Gamma_{\text{inv}} = \frac{\lambda_{hs}^2 v(T)^2}{32\pi m_h} \sqrt{1 - \frac{4m_S^2}{m_h^2}} \ . \tag{8.7}$$

If the $SS \to hh$ channel is open, i.e. $m_S > m_h$, then we need to include the cross section $\sigma_{SS\to hh}$. In this case, one has to sum over the Higgs-mediated s-channel, $S-$mediated t-channel and u-channel, and the contact $SShh$ diagrams, which gives [7]

$$\sigma_{SS\to hh} v_{\text{lab}} = \frac{\lambda_{hs}^2 v_H}{32\pi(s - 2m_S^2)} \left[a_R^2 + a_I^2 + \frac{8y^2}{1-x^2} - \frac{2y(a_R - y)}{x} \log\left(\frac{1+x}{1-x}\right)^2 \right] \tag{8.8}$$

where

$$a_R \equiv 1 + 3m_h^2(s - m_h^2) \left|D_h(s)\right|^2 \ , \qquad a_I \equiv 3m_h^2 \sqrt{s} \left|D_h(s)\right|^2 \ , \tag{8.9}$$

$$y \equiv \frac{\lambda_{hs} v(T)^2}{s - 2m_h^2} \ , \qquad x \equiv \frac{2v_S v_H}{1 + v_H^2} \ , \tag{8.10}$$

$$v_S \equiv \sqrt{1 - \frac{4m_S}{s}} \ , \qquad v_H \equiv \sqrt{1 - \frac{4m_H}{s}} \ . \tag{8.11}$$

Before EWSB we have $v(T) = 0$ and thus the only process happening is $HH \to SS$. When the coupling λ_{hs} is small S never reaches thermal equilibrium with the thermal bath, e.g. if $T_R = 10^{16}$ the scalar will not reach equilibrium if $\lambda_{hs} < 10^{-7}$ [106]. This should be noted to be dependent on the reheating temperature, if T_R is small the interaction rate is suppressed, which means that the freeze-in formalism can be used for rather large portal couplings. The differential equation that determines the yield Y_S produced from freeze-in is given by Eq.(5.14) (and Eq.(3.42)). It has to be solved separately for $T > T_{\text{EW}}$ and $T < T_{\text{EW}}$, with the continuity of Y_S imposed as the boundary condition between the two regimes. For $m_S < m_h/2$ one finds that the dominant contribution to the scalar singlet yield stems from temperatures $T \sim m_h/2$ and can be interpreted as equilibrium decays of SM Higgs bosons into pairs of scalar singlets (see appendix B for the discussion of the correspondence between $1 \to 2$ and $2 \to 2$ processes in the case of an s-channel resonance). The resulting relic abundance of scalar singlets is straight-forward to calculate and the corrections from finite-temperature and quantum effects is small.

I will therefore focus on the more interesting case that the dominant contribution does not arise from Higgs decays. This happens either if $m_s > m_h/2$, where on-shell Higgs boson decays into scalar singlets are kinematically forbidden or if $m_s, T_R \ll m_h$, such that the density of Higgs bosons in the thermal plasma are exponentially suppressed for all relevant temperatures. In the latter case, the processes relevant for

the freeze-in production of scalar singlets can be written as an effective dimension-5 operator of the form

$$\mathcal{L} \supset \frac{1}{\Lambda_f} \bar{f} f S^2 \,, \tag{8.12}$$

where $\Lambda_f = m_h^2/(\lambda_{hs} m_f)$. As a result, we will see that the freeze-in yield becomes sensitive to the reheating temperature. I will therefore structure the discussion below according to whether $T_R \gg m_h$ (such that the freeze-in yield is independent of T_R) and $T_R \ll m_h$.

8.2 High reheating temperature

The case where the reheating temperature is large has been extensively studied in the freeze-out scenario [6, 128, 135, 139] and it is the most studied case for the freeze-in scenario as well [143]. However, thermal effects have been neglected and quantum statistical factors are usually also neglected (Ref. [144] calculated the relic abundance using the quantum statistical factors). I am most interested in the case where the dominant DM contribution does not arise from on-shell Higgs decays. I will thus compare the results obtained for DM masses above and below $m_h/2$. The freeze-in production is IR-dominated when $T_R \gg m_s, m_h$, meaning that the resulting abundance is independent of the reheating temperature. This follows from the observation that before the EWPT and for $T \gg m_s$ the DM production cross section (found by using unitarity on Eq.(7.10) to get $HH \to SS$) is proportional to $1/s$, such that the DM production rate is proportional to T, since $\Gamma_{HH\to SS} = \langle \sigma v \rangle n^{\text{eq}}$ and since all particles are relativistic $n^{\text{eq}} \propto T^3$ and $\langle \sigma v \rangle \propto 1/T^2$, which means that it becomes negligible compared to the Hubble expansion rate at high enough temperatures.

In figure 8.1 I show in the left panel the thermally averaged DM annihilation cross section for the scalar masses $m_S = 10\,\text{GeV}$ (orange) and $m_S = 300\,\text{GeV}$ (blue) which is given by Eq.(5.34) when quantum statistics are included, displayed by the solid lines, and by Eq.(4.22) when they are ignored, displayed by dashed lines. In the right panel the resulting change in the DM yield dY_S/dx found by Eq.(5.14) and Eq.(3.42), as a function of inverse temperature is shown. I include the result obtained by neglecting quantum statistical factors and using Maxwell-Boltzmann distribution in order to highlight the quantum statistical effects. From the behaviour of dY_S/dx we can see that the scalars are created until some temperature which is dependent on the FIMP mass. As the temperature decreases the interaction rate $\Gamma = \langle \sigma v \rangle n^{\text{eq}}$ will decrease and when $\Gamma < H$ the FIMP abundance freezes-in, i.e. $dY_S/dx \to 0$. There is as expected qualitatively different behaviour for DM masses above and below $m_h/2$. For $m_s = 10\,\text{GeV}$ production is dominated by processes involving the exchange of an on-shell Higgs boson, which can be seen from the rapid increase in dY_s/dx for the orange lines at the Higgs resonance in the right panel of figure 8.1. When $T < m_h/2$ the yield decreases rapidly, this is because the production rate decreases once the typical

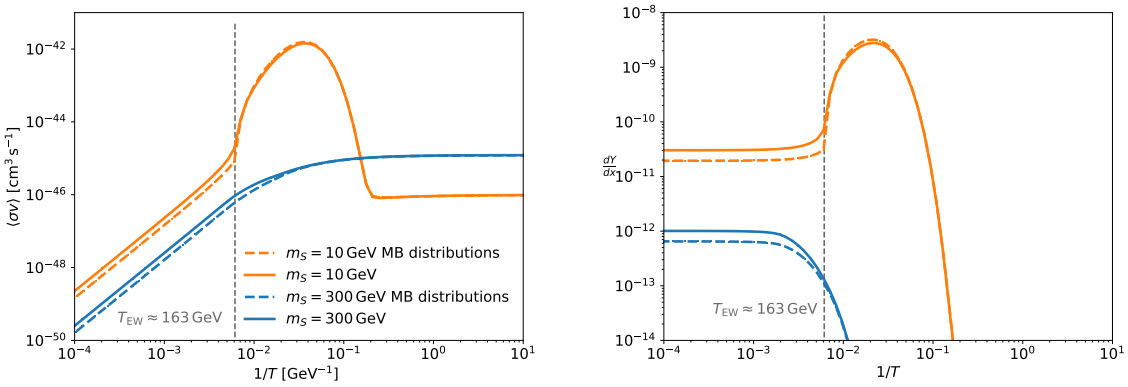

Figure 8.1: *Left panel.* Thermally averaged cross section for $m_S = 10\,\text{GeV}$ (orange) and $m_S = 300\,\text{GeV}$ (blue). Dashed lines show when quantum statistical effects are ignored, i.e. Maxwell-Boltzmann distributions are assumed, and Bose-enhancement/Fermi-blocking factors are ignored. The grey dashed line shows $T = T_{\text{EW}} \approx 163\,\text{GeV}$. *Right panel.* $\frac{dY_X}{dx}$ for $m_S = 10$ and $m_S = 300\,\text{GeV}$. The colours and styles represent the same as for the other plot.

centre-of-mass energy in the thermal bath becomes insufficient to produce on-shell Higgs bosons, i.e. when $T \sim m_h/2 \approx 62.5\,\text{GeV}$. When the temperature drops below m_S there will be an exponential suppression in n^{eq} which means $\Gamma < H$. Note that for $m_S = 10\,\text{GeV}$ there is a decrease in dY_S/dx both because production of on-shell Higgs becomes suppressed and because n^{eq}. The dominant contribution comes as expected from the Higgs resonance $T \approx m_h/2$. When $T \gg m_h/2$ the cross section is proportional to $1/s$ which means that $\langle\sigma v\rangle \propto 1/T^2$. Since I use the thermally averaged annihilation cross section in the Boltzmann-equation given by Eq.(5.14) there is no exponential suppression in $\langle\sigma v\rangle$ as $T \to 0$, instead we will have the same feature as we have seen in section 4.4. $\langle\sigma v\rangle$ can be an expanded in terms of powers of x^{-1} for non-relativistic gases, which we can assume as $T \to 0$. this means that $\langle\sigma v\rangle$ becomes constant for small temperatures, which is what we see in figure 8.1. The suppression we see in dY_S/dx comes from the distribution functions $T < m_S$. For $m_s = 300\,\text{GeV}$, the virtual Higgs boson must always be off-shell and hence the temperature dependence of the annihilation cross section becomes more trivial since the exponential suppression happens before the Higgs resonance. The relevant contributions to the DM abundance arise from both before and after the EWPT (indicated by the dashed vertical line). Finally, the quantum statistical factors can be seen to have a noticeable contribution for dY_S/dx in figure 8.1. For $T > m_h/2\,\text{GeV}$, we can see that the Bose-Enhancement factors coming from the production from W's, Z's, h's, and H's give a sizable increase in the contribution to the yield dY_S/dx. This will result in an increase in the relic abundance for $m_S > m_h/2$. However, if $m_S < m_h/2$ then the main contribution to the relic abundance will come from Higgs decays and the $2 \to 2$ process producing the on-shell Higgs is coming from $b\bar{b}$, which explains the difference between the orange solid- and dashed lines at the Higgs-resonance in figure 8.1).

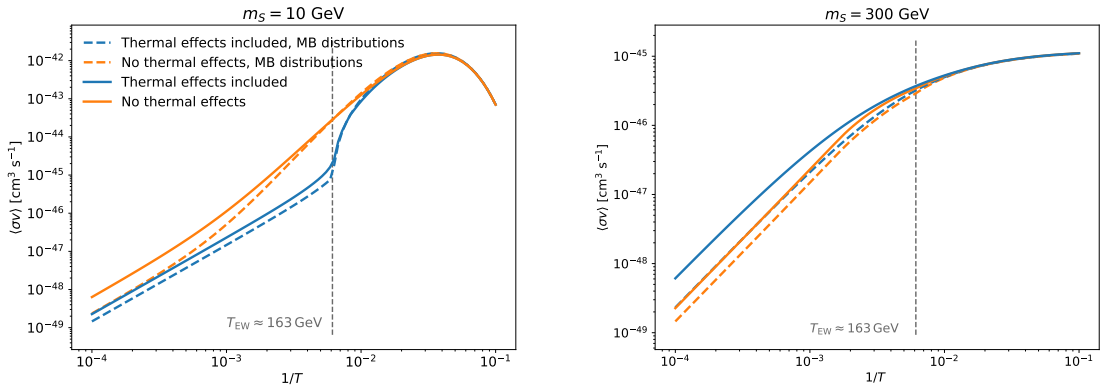

Figure 8.2: *Left panel:* Thermally averaged cross section for $m_S = 10\,\text{GeV}$ as a function of T^{-1}. The case when thermal effects are included, i.e. thermal masses and EWSB, is plotted i blue. The orange lines ignore these effects. The dashed lines show when quantum statistical effects are ignored. The grey dashed line shows $T = T_{\text{EW}} \approx 163\,\text{GeV}$. *Right panel:* Same plot as above, but with $m_S = 300\,\text{GeV}$.

The thermal effects are included by using the formalism from chapter 6 and chapter 7. The thermal complex Higgs mass is given by Eq.(6.42) which has to be used for $T > T_{\text{EW}} \approx 163\,\text{GeV}$. As the temperature falls below T_{EW} I use the numerical solution for $v(T)$ and $m_h(T)$. The off-shell Higgs decay width that is used is given by Eq.(7.14). These effects can be seen for masses m_S both above and below $m_h/2$. In order to highlight the thermal effects I show in figure 8.2 the thermally averaged cross section for $m_S = 10\,\text{GeV}$ and for $m_S = 300\,\text{GeV}$ for both the case where we include the thermal effects, displayed by the blue lines, and when we ignore them, displayed by the orange lines. The EWPT is very noticeable for $m_s = 10\,\text{GeV}$, but its contribution to the relic density is small due to the Higgs resonance. When $T \ll T_{\text{EW}}$ we see that the thermally averaged cross sections agree, this is as expected since $v(T \ll T_{\text{EW}}) = v_0$. As $T \to T_{\text{EW}}$ the thermally averaged cross section including thermal effects will become suppressed since for $T \sim T_{\text{EW}}$ we have $v(T) < v_0$ and thus all the SM masses become smaller than their zero temperature masses. The fact that we include thermal masses for both the Higgs and for all SM particles below $T < T_{\text{EW}}$ ensures that there is no discontinuity at $T = T_{\text{EW}}$. The only process when $T > T_{\text{EW}}$ is $HH \to SS$ and thus the only cross section we need is given by Eq.(7.10). If we do not include the thermal mass for the complex Higgs (i.e. $m_H(T) = 0$) we would find that for $T \gg T_{\text{EW}}$ the thermally averaged cross sections would agree. This is because of the Goldstone boson equivalence theorem. But since the thermal mass for the complex Higgs is included, we get that there is a $\sim 47\%$ difference between the thermally averaged cross sections (i.e. the difference between the blue- and red dotted lines at $T \sim 10^4\,\text{GeV}$). Finally, the inclusion of thermal effects can be seen in figure 8.2 to make the quantum statistical effects less important. This is because the thermal mass makes the complex Higgs less relativistic, which means that the quantum statistical factors will give a smaller contribution. This can be seen by comparing the difference between the solid lines and

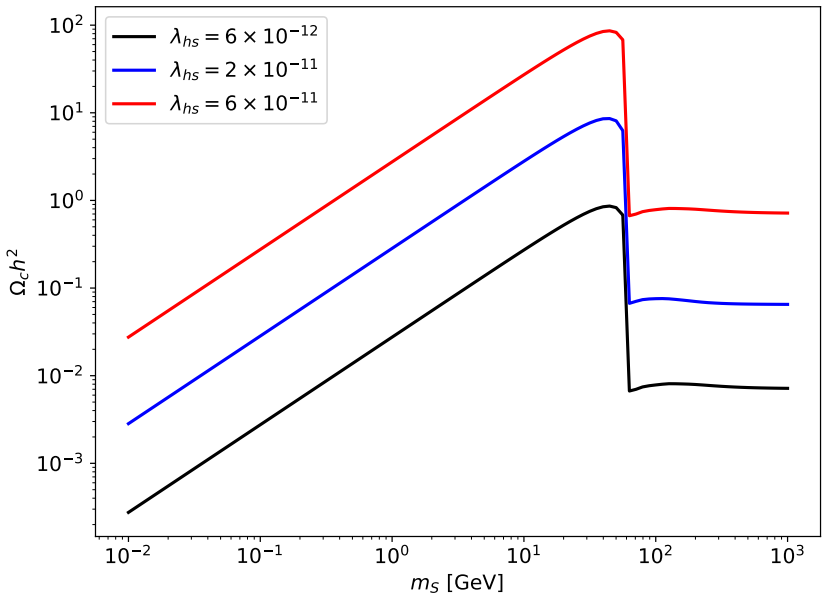

Figure 8.3: Relic abundance produced by freeze-in for three different couplings: $\lambda_{hs} = 6 \times 10^{-11}$ (red),$\lambda_{hs} = 2 \times 10^{-11}$ (blue) and $\lambda_{hs} = 6 \times 10^{-11}$ (black). Maxwell-Boltzmann distribution is assumed for all the particles and Bose-enhancement/Fermi-blocking factors are ignored. No thermal effects are included either.

the difference between the dashed lines in figure 8.2.

The observed relic density Ω_c for given values of λ_{hs} and m_S is found by integrating over the right panel of figure 8.1 and using Eq.(4.24). In figure 8.3 I display the observed relic abundance $\Omega_c h^2$ as a function of m_S for three different values of λ_{hs}. For simplicity I have assumed Maxwell-Boltzmann distributions for all particles, the result by including the full distribution will be discussed later. We see the expected result that the abundance is proportional to λ_{hs}^2, since $\langle \sigma v \rangle_{MB} \propto \lambda_{hs}^2$ in the singlet scalar model, the λ_{hs}^3 and λ_{hs}^4 terms coming from the t- and u-channel in the $SS \to hh$ cross section is negligible since the coupling for freeze-in is $\mathcal{O}(10^{-11})$. We can again see that there is qualitatively different behaviour for DM masses above and below $m_h/2$, most noticeable is the sharp drop at the Higgs resonance $m_h/2$. The fact that the relic density for m_S slightly above $m_h/2$ is significantly lower than the relic density for m_S slightly below $m_h/2$ is because in the former case, DM is solely produced by $2 \to 2$ scatterings, while in the latter case it is produced by Higgs decays. When the abundance is produced from Higgs decays we have the expected behaviour that the relic abundance is proportional to the DM mass, since the DM abundance freeze-in then $T \sim m_h/2$ and Y_S is thus independent of m_S. On the other hand, the relic abundance is roughly independent of the DM mass when it is larger than $m_h/2$. This is because the abundance freezes-in when $T \sim m_S$, which means that $Y_S \propto m_S^{-1}$.

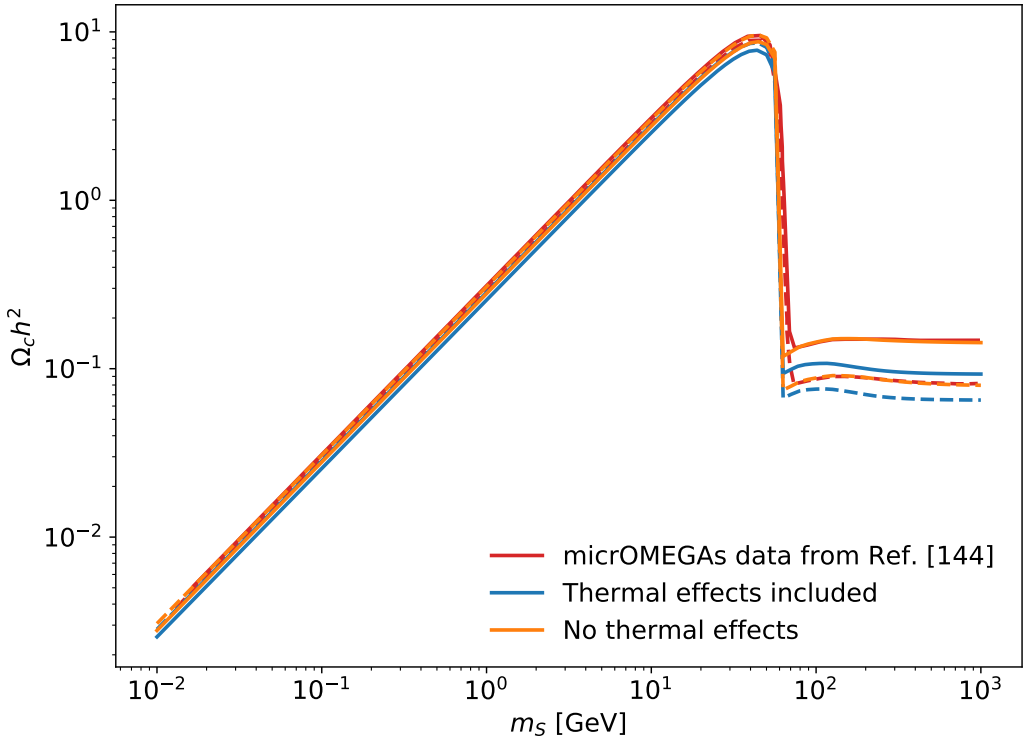

Figure 8.4: Relic density as a function of m_S. Solid lines include quantum statistical effects, dashed lines neglect these effects. The red line is the digitization of the results from Ref. [144]. In this figure I use that $\lambda_{hs} = 2 \times 10^{-11}$ and $T_R = 10^6$ GeV.

In figure 8.4 I display in the DM relic density $\Omega_c h^2$ as a function of m_S for $\lambda_{hs} = 2 \times 10^{-11}$ for the case when we include and ignore EWSB. For comparison, I show the corresponding curves obtained without quantum statistics (dashed) and the digitized result from Ref. [144] which has used micrOMEGAs. Since the production is dominated by Higgs decays for $m_S < m_h/2$ we get that there is little effect of including thermal and/or quantum statistical effects. This is because the dominant production happens when $T \sim m_h/2$, where both thermal and quantum statistical effects are small. The story is different for $m_S > m_h/2$. Including quantum statistical effects is seen to increase the relic abundance significantly. In fact, when thermal effects are neglected, there is almost a factor 2 difference between when we include the quantum statistical factors and when we do not. This effect is combated by the thermal effects in the early universe. This is as mentioned because of the Bose-enhancement factors for the W's, Z's, h's, and H's. When thermal effects are included, the quantum statistical effects increase the abundance merely by a factor ~ 1.5. This is due to the fact that including the thermal masses for the complex H will make it less relativistic and hence its quantum statistical factors will reduce. This is also a reason why the abundance is

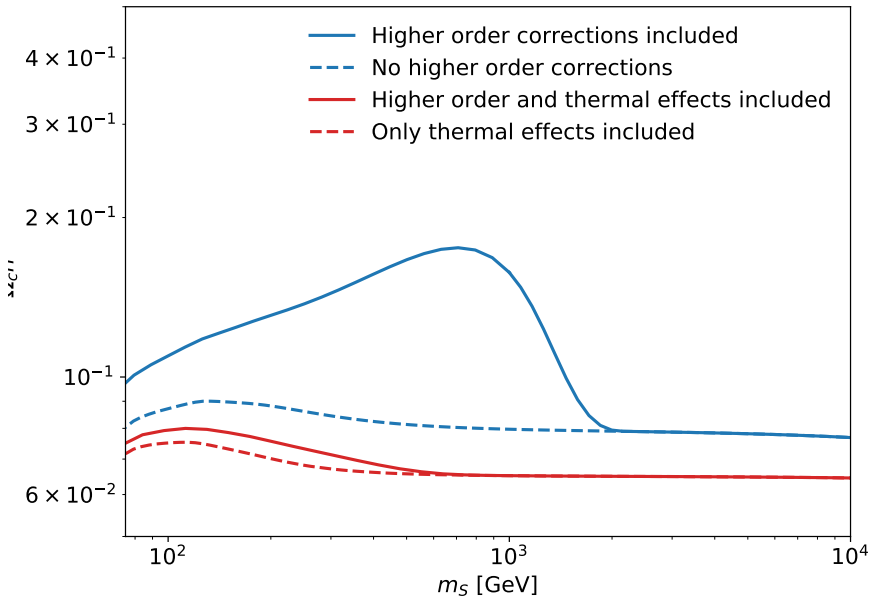

Figure 8.5: Relic density as a function of m_S, where the solid lines shows the inclusion of higher order effects using tables produced by HDECAY to get the off-shell Higgs decay widths, while the dotted line does not include NLO-corrections. The red lines include thermal effects, while the blue lines ignore these effects.

smaller when thermal effects are included, compared to when they are not, since the annihilation cross section will be smaller due to the thermal mass.

The final effect I have included for high reheating temperatures are higher order corrections to the SM couplings. This is included by using the $\Gamma_{h^*}(\sqrt{s})$ tabulated using HDECAY [134] which includes NLO-corrections. In order to not break unitarity I have used the cross section calculated using Eq.(7.12). There is a mild correction for $m_S < m_h/2$ since the dominant contribution to the abundance comes from the Higgs resonance. On the other hand, for $m_h/2 < m_S < 1.5\,\text{TeV}$ the effect can be important. The effect of the NLO-correction can be seen in figure 7.1, i.e. they start to become important as $\sqrt{s} \sim 1.5\,\text{TeV}$ when thermal effects are neglected. The higher order effects on the abundance can be seen in figure 8.5 when thermal effects are both included and neglected. There is as expected an increase in the abundance due to these corrections when thermal effects are neglected. Since $\sqrt{s}$ is integrated from $2m_S$ in the thermally averaged cross section, the effect should become important until $\sigma(SS \to XX)^{\text{unitary}} < \sigma(SS \to XX)^{\text{tree}}$ due to unitarization. This happens when $\sqrt{s} \sim 3\,\text{TeV}$ which is seen in figure 7.1. This explains the increase in the abundance until $m_S \sim 1\,\text{TeV}$, and the magnitude is expected since EWSB is neglected, which means that the s-channel Higgs exchange is used up to arbitrarily large $\sqrt{s}$. When $m_S > 1\,\text{TeV}$ the effect will start to decrease since the energies where the NLO-

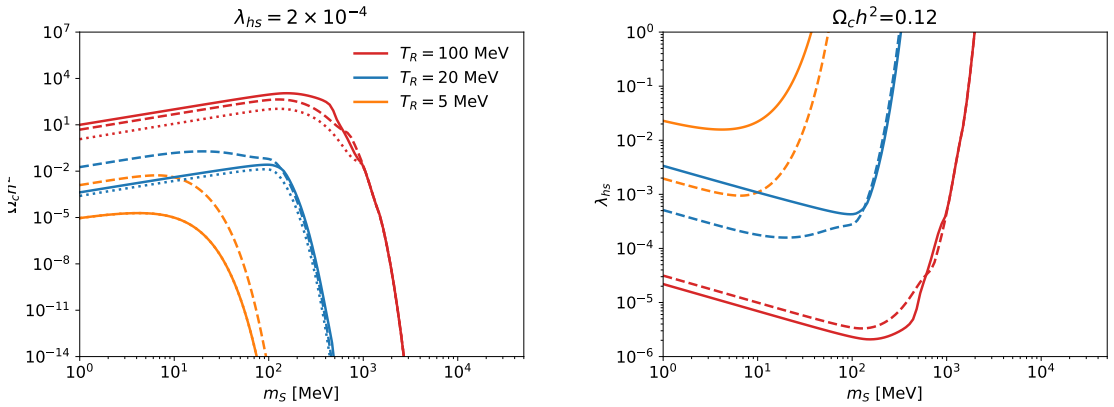

Figure 8.6: *Left panel*: The observed relic abundance $\Omega_c h^2$ produced by $2 \to 2$ scatterings, with the reheating temperatures $T_R = 5\,\text{MeV}$ (orange), $T_R = 20\,\text{MeV}$ (blue) and $T_R = 100\,\text{MeV}$ (red), where the coupling is $\lambda_{hs} = 2 \times 10^{-4}$. The solid lines show the off-shell Higgs decays into leptons and bosons, while the dashed lines have off-shell Higgs decays into free quarks, gluons, and leptons. The dotted lines show the leptonic and bosonic contribution to the relic density. *Right panel*: The coupling λ_{hs} needed to give the correct relic density ($\Omega_c h^2 = 0.12$) as a function of m_S.

corrections are important start to become kinetically forbidden. Finally, as m_S becomes large enough ($m_S > 1.5\,\text{TeV}$), the NLO-corrections are no longer kinetically available and the result is given by the tree-level result, explaining the fact that the solid and dotted lines converge. Including thermal effects is seen to make the effect of including higher order corrections a lot smaller. This is because for $T > T_{\text{EW}}$, the tree-level result is used for $HH \to SS$, which means that the higher-order corrections are not fully encapsulated. The reason why the red lines converge faster than the blue lines is because the solid red line uses the temperature dependent vev, which means that for a vev smaller than the zero temperature vev, we will have that unitarity will be broken at an energy that is a factor $v_0/v(T)$ lower than the zero temperature energy, this can be seen from Eq.(7.14).

8.3 Low reheating temperature

The last scenario I will look at is when $T_R \ll m_h$. this means that the relic abundance cannot be produced by on-shell Higgs decays. The lower bound on the reheating temperature coming from the Planck data is 4.7 MeV when the neutrino masses are allowed to vary [145]. I will therefore look at reheating temperatures from 5 MeV to 100 MeV. From figure 7.2 I expect that we will see effects coming from the QCD phase transition when the off-shell Higgs decay width into hadrons is negligible compared to the decay width into free quarks and gluons. In figure 8.6 I display in the left panel the observed relic density $\Omega_c h^2$ produced by $2 \to 2$ scatterings with the three reheating

temperatures $T_R = 5\,\text{MeV}$, $T_R = 20\,\text{MeV}$ and $T_R = 100\,\text{MeV}$, where the coupling is $\lambda_{hs} = 2 \times 10^{-4}$. In the right panel the coupling that gives the observer relic density as a function of m_S. The fact that large portal couplings should cause the dark sector to thermalize with the SM, is only true for large reheating temperatures. For small temperatures, the interaction rate is proportional to $T^2 v^2/m_h^4 \ll 1$, which means that one can consistently apply freeze-in for rather large couplings. The relic density for all three reheating temperatures becomes exponentially suppressed when $m_S \gg T_R$. This comes from the thermally averaged cross section given by Eq.(5.34), since the only particles with enough energy to produce the scalars lie on the Boltzmann-tail. From the plot of the thermally averaged cross section in figure 7.2 the abundance is seen to be dependent on the reheating temperature. This is because the scalars freeze-in when $T \sim T_R$, which means that this process is UV dominated and the relic abundance will be constant with respect to the mass (as long as $m_S < T_R$). The relic density will thus be proportional to m_S^{-1}. The dashed lines show the relic density found by assuming that the off-shell Higgs decays only into free-quarks, gluons and leptons, i.e. ignoring the effect coming from the QCD phase transition. From the right panel in figure 7.2 we expected to see that the effect of including decays to hadrons would start to become important when $T \lesssim 100\,\text{MeV}$, since that is the temperature where the dotted and solid lines start to deviate. For large scalar masses we expect to see that the effect becomes less important. For $T_R = 100\,\text{MeV}$ we see that the correction to the relic density is small. This is as expected since the dominant abundance comes from $T \sim T_R$, since dY_S/dx decreases quickly from $T \sim T_R$. This can be seen from figure 8.7 where dY_S/dx is plotted for $T_R = 100\,\text{MeV}$ and $m_S = 100\,\text{MeV}$ in the left panel and $T_R = 20\,\text{MeV}$ and $m_S = 20\,\text{MeV}$ in the right panel. It can also be seen in the right panel of figure 7.2, since the effect is small for $T = 100\,\text{MeV}$ and the Hadronic contribution and the quark contribution are both close in magnitude. For $T_R = 20\,\text{MeV}$, the density set by using the Higgs decay width to free quarks, is a factor ~ 38 larger than the abundance set by using the width to hadrons. This can be understood from the right panel in figure 8.7 since the hadronic contribution has become suppressed while the quark and gluon contribution is not. The reason to why dY_S/dx is not constant for large T, as was the case for large reheating temperatures, is because the dominant contribution comes from channels that already are exponentially suppressed, e.g. $\mu\mu$ for $T_R = 20\,\text{MeV}$, which would not be exponentially suppressed for higher temperatures. The effect of using hadrons is further enhanced for $T_R = 5\,\text{MeV}$ where the factor is ~ 128, since the hadronic contribution is negligible at these temperatures. This is to be expected from the difference between the dashed and solid lines in figure 7.2. The fact that the effect of accounting for abundance coming from hadrons instead of quarks and gluons, becomes smaller for higher scalar masses - see the red and purple lines in figure 7.2 - can also be seen in figure 8.6 since the difference between the dotted and solid lines decreases as m_S becomes large. The dotted lines in figure 8.6 show the leptonic and bosonic contribution to the abundance, the remaining contribution comes thus from hadrons (or free quarks and gluons for the dashed lines). For $T_R = 5\,\text{MeV}$ there is no contribution from hadrons, which is because for such a small reheating temperature the energies accessible do not give a contribution using $\Gamma_{h^* \to \text{hadrons}}$. On the other hand,

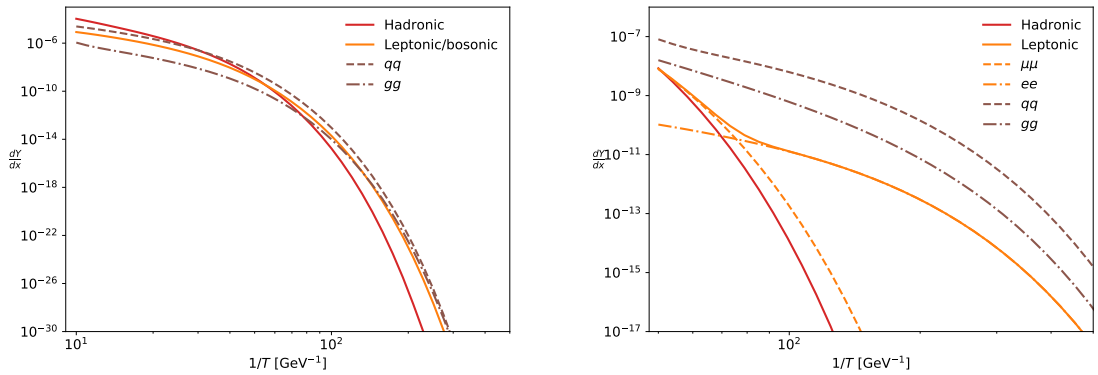

Figure 8.7: *Left panel:* $\frac{dY_S}{dx}$ as a function of $1/T$ for $T_R = 100\,\text{MeV}$ and $m_S = 100\,\text{MeV}$. The different yields are explained in the legends. *Right panel:* Same as left plot, but for $T_R = 20\,\text{MeV}$ and $m_S = 20\,\text{MeV}$.

when $T_R = 20\,\text{MeV}$ and $T_R = 100\,\text{MeV}$, the energies will give a sizable contribution from $\Gamma_{h^* \to \text{hadrons}}$. For $T_R = 100\,\text{MeV}$ the contribution from hadrons is seen to dominate, which is to be expected from the left panel in figure 8.7 since the hadronic contribution dominate when $T \sim T_R$. For $T_R = 20\,\text{MeV}$, the contribution from hadrons and leptons and bosons are about equal. This is a numerical coincidence since increasing T_R will make the hadronic contribution more important, this can be understood from the right panel in figure 8.7.

8.4 Summary and Discussion

In the previous sections I have applied the formalism I outlined in sections 5 to 7 to the scalar singlet model. An important part of this work has been to implement this formalism as well as the freeze-in Boltzmann equation derived in section 5.2 to the FORTRAN package DarkSUSY [7], for a short introduction see appendix A. Comparing the results from micrOMEGAs [144] to my results, we can see in figure 8.4 that the Boltzmann equation given by Eq.(5.7) gives as expected the same result as the standard treatment. The difference between the two descriptions is that Eq.(5.7) has been written in terms of the annihilation cross section instead of the creation cross section, as well as using momentum conservation to rewrite the distribution functions in terms of terms that look like MB distribution functions for the scalars, together with Fermi-blocking/Bose-enhancement factors for the SM states. This has two important benefits, it makes for a better numerical implementation and as was discussed in section 7, higher order effects to SM couplings are easier to implement. It is important to note that the MB distribution terms for the FIMPs are in fact not the *actual* distribution functions, they merely follow from Eq.(5.9) and by using momentum conservation. Another distinction from the standard treatment where the

production cross section is used, is the fact that the thermally averaged cross section has become dependent on quantum statistics, while in the standard treatment, thermally averaged cross sections are independent of quantum statistics. Instead they appear in the distribution functions. This new implementation works well when working with the scalar singlet model, but it remains to implement the possibility of a dark sector with multiple FIMPs and the possibility of self-interactions in this sector.

The fact that FIMPs have such small couplings to the visible sector makes the Boltzmann equation a lot easier to solve than for freeze-out. The Boltzmann equation for freeze-out is non-linear, while for freeze-in one simply needs to make one change of variables in order to get the solution by directly integrating the equation. However, FIMPs are never in thermal equilibrium with the visible sector heat bath, which means that the thermal effects that would be negligible for freeze-out, turn out to have a lasting impact on the relic abundance for freeze-in. The thermal effects I included are the electroweak phase transition, thermal masses coming from plasma effects and the QCD phase transition. For high reheating temperatures it is EWSB and thermal masses that are important. This was the first case I looked at ($T_R \gg m_h$). I found that for scalar masses below the Higgs resonance ($m_S < m_h/2$), the relic abundance is independent of the scalar mass, which means that the relic density is proportional to the scalar mass. This is expected because the abundance is dominantly produced when $T \sim m_h/2$. For $m_S > m_h/2$ the abundance freezes-in when $T \sim m_S$ which means that the relic abundance is proportional to m_S, and we thus get that the relic abundance is independent of the scalar mass. This is also as expected since the exponential suppression begins as $T > 2m_S$, which can be seen from Eq.(5.34). Another observation is the fact that the relic abundance is proportional to λ_{hs}^2, this is because $\langle \sigma v \rangle \propto \lambda_{hs}^2$ for the scalar singlet model, and since λ_{hs} is of the order $10^{-9} - 10^{-12}$ any λ_{hs}^3 and λ_{hs}^4 terms coming from the t- and u-channel in the $hh \to SS$ process are simply negligible.

A new effect included in this work is thermal effects. For temperatures well above EWSB ($T \gg T_{\text{EW}}$) the thermally averaged cross section calculated when thermal effects are included is smaller than the one obtained when thermal masses are neglected. This is expected from looking at Eq.(7.10), since increasing $m_H(T)$ will decrease the cross section. When the temperature decreases towards T_{EW} the only channel contributing to the scalar abundance is the $HH \to SS$ channel. For the case where EWSB is neglected, other channels will start to contribute, which is why the lines starts deviating in the left panel in figure 8.1. After EWSB $v(T)$ goes from zero to v_0, this ensures that there is no discontinuity at $T = T_{\text{EW}}$ and we will get the usual prescription as $T \to 0$. The most important aspect of the thermal effects comes when quantum statistical effects are included. For $m_S < m_h/2$ neither thermal nor quantum statistical effects are important, but for $m_S > m_h/2$, they are. The quantum statistical effects will increase the abundance by nearly a factor 2 when thermal effects are neglected. This is expected because the $WW \to SS$, $ZZ \to SS$ and $hh \to SS$ will have Bose-enhancement factors that increase the yield. Thermal effects will on the other hand have the opposite effect. The inclusion of thermal effects will decrease the thermally

averaged cross section for high temperatures, as can be seen in figure 8.2. This fact will as expected only become stronger when quantum statistical effects are included. This is because the thermal mass for the complex Higgs makes it less relativistic leading to smaller quantum statistical factors. The fact that the quantum statistical effect is inherently linked to thermal effects means that it is essential to include them in dark matter relic density calculations. The final effect I looked at for high reheating temperatures was higher order corrections to the SM couplings. This is an important effect if thermal effects are neglected. For $m_S < m_h/2$ this effect is negligible because the dominant contribution comes from the Higgs resonance. On the other hand, for $m_h/2 < m_S < 1.5\,\text{TeV}$ the effect is important to include, since decay into gauge bosons dominates when $\sqrt{s} \gg v$ and large NLO EW corrections arise from the real emission of additional gauge bosons. The NLO-corrections are seen in figure 7.1 to be extra important when $\sqrt{s} \simeq 1.5\,\text{TeV}$. Since s is integrated from $4m_S^2$ to ∞ in $\langle\sigma v\rangle$ given by Eq.(5.34) the NLO-corrections will become kinetically unavailable as $m_s > 1.5\,\text{TeV}$. This corresponds to $\sqrt{s} > 3\,\text{TeV}$, which is expected from figure 7.1. This explains the increase and decrease in the abundance in figure 8.5. Including the thermal effects changes this importance, at least when higher order corrections to the process $HH \to SS$ are neglected. However, the thermal effects will anyway make the higher order effects less important since a finite temperature vev is smaller than the zero temperature vev which lowers the energy where unitarity is broken by a factor $v_0/v(T)$ as expected from Eq.(7.14). Including higher order corrections to the process $HH \to SS$ remains to be done, which is expected to also increase the abundance when thermal effects are included.

The other interesting case I looked at was when the reheating temperature is less than the Higgs mass, resulting in the abundance being produced from $2 \to 2$ scatterings via an off-shell Higgs mediator. The range of reheating temperatures I found interesting was $5 - 100\,\text{MeV}$, since the lowest possible reheating temperature is $4.7\,\text{MeV}$ [145] and at $100\,\text{MeV}$ the effects from including the QCD phase transition is starting to become small. We can see that the inclusion of the QCD phase transition - the fact that free quarks no longer exist for $T < T_{\text{QCD}}$ and $\sqrt{s} < 2\,\text{GeV}$, and instead we have to use chiral perturbation theory to describe interactions with hadrons - was important. This effect is seen to become more and more important as the reheating temperature is decreased. This is because there is a very clear Boltzmann suppression since all the masses are bigger than T_{QCD}. When $T_R \simeq 100\,\text{MeV}$, the contribution coming from hadrons is seen to have changed the abundance slightly compared to when the contributions come from free quarks. This is because the hadronic contribution will give slightly larger contribution when $T \sim T_R$ which can be seen in the left panel of figure 8.7. On the other hand, when $T_R = 20\,\text{MeV}$ and $T_R = 5\,\text{MeV}$, the effect has become extremely important to include, due to the very clear Boltzmann suppression of hadrons. This suppression is seen for $T_R = 20\,\text{MeV}$ in the right-hand panel of figure 8.7 and I get that there is a factor ~ 38 difference, while for $T_R = 5\,\text{MeV}$ the factor is nearly ~ 128. The Boltzmann suppression means that the energies achievable will give a Higgs decay width into hadrons that is a lot smaller than the decay width

into quarks and gluons, resulting in a much smaller scalar abundance. The decay width into hadrons that is implemented now is the digitization of the results from Ref. [137], which means it remains to implement the analytical results for the partial Higgs decay widths into hadrons. The fact that the correct abundance for $T_R = 5\,\mathrm{MeV}$ is given when the coupling is of the order of magnitude $\lambda \sim \mathcal{O}(10^{-2})$, means that for sufficiently large couplings, laboratory searches for scalar singlets, in particular at the LHC where the centre-of-mass energy is sufficient to produce on-shell Higgs bosons will be feasible. The strategy that is the most promising to probe sub-GeV scalar singlets is invisible Higgs decays searches. The invisible partial decay width is given by Eq.(8.7) from which the invisible branching ration can be calculated as $\mathrm{BR}_{h\to\mathrm{inv}} = \Gamma_{\mathrm{inv}}/\Gamma_{\mathrm{tot}}$. Recently, a combination of searches for invisible Higgs decays at the LHC have found that $\mathrm{BR}_{h\to\mathrm{inv}} < 0.11$ [70], which corresponds to $\lambda_{hs} < 0.01$. In other words, for the small reheating temperatures considered in this analysis, some of the couplings required by the freeze-in mechanism is already excluded.

These results show that it is generally important to include thermal effects when the dominant DM contribution for freeze-in does not arise from on-shell decays. Without these effects, quantum statistical effects can give a too large contribution to the abundance, since the thermal mass will make the particles less relativistic and thus reduce this contribution. If the reheating temperature is small, then effects from the QCD phase transition will be important to include since the free quark and gluon contribution will give a too large contribution to the DM abundance. The routines used to study the scalar singlet model is explained in appendix A, and they are easily applied to other models that include a FIMP where self-interactions are negligible. The thermal effects are however model dependent and must be found for the specific model, but the formalism introduced in section 6 is easily extended to include more particles.

Chapter 9

Conclusions

For the past decades DM research has mainly focused on the WIMP paradigm. This paradigm centres around WIMPs, and if they exist, they would have been in thermal equilibrium with the visible sector heat bath in the early universe. As the temperature of the universe cooled down, WIMPs experience thermal freeze-out. The WIMP miracle and its naturalness has made WIMPs attractive DM candidates. However, the null results coming from detection experiments and the further shrinking parameter space have made it imperative to look at other DM production mechanisms. The freeze-in mechanism is a natural DM production mechanism to look at. For freeze-in to happen, the couplings have to be magnitudes smaller than for WIMPs because freeze-in requires that there is no thermal equilibrium between the dark and visible sector. This naturally explains the absence of any clear DM signal, while at the same time FIMP models can still explain the observed relic abundance and in some special cases, be detectable with upcoming high-sensitivity experiments.

In this work, I started by showing that the freeze-in Boltzmann-equation can be written in a form that is more suitable for numerical implementation and for including higher order corrections for the SM couplings. By using a mathematical trick, I rewrote the distribution functions in terms of an *auxiliary* distribution for the FIMPs, and instead of using the production cross section, I used the annihilation cross section. This means that in contrast to the standard treatment, where one has to calculate the number density for all the particles in the heat bath and the corresponding thermally averaged annihilation cross section, I only had to use the auxiliary FIMP distribution and the corresponding thermally averaged cross section. Importantly, this formalism provides an accurate prescription of the freeze-in mechanism, even though we have no actual knowledge about the actual FIMP distribution function, other than that it initially is zero and is negligible compared to the distribution functions for the bath particles. This description is analogous to the production term in the freeze-out scenario with Maxwell-Boltzmann distributions for all the bath particles. This, however, cannot always be assumed for DM particles that are created relativistically,

which is why I included the relativistic description using the full distribution functions and included quantum statistics. This description also has the added benefit that when the FIMP is produced through a Higgs portal, higher order corrections to the SM couplings can easily be included.

The fact that FIMPs never reach thermal equilibrium with the heat bath means that thermal events and effects from the early universe will leave a lasting impact on the DM relic abundance. Events such as the electroweak and QCD phase transitions were therefore important to include when doing freeze-in calculations. The model where I studied these effects was the scalar singlet model. This is one of the simplest extensions of the SM, it simply adds a new gauge-singlet real scalar field. Even though the model is simple, the effects I include made it a good model to look at. I looked at two cases; the first case was when the reheating temperature was much higher than the Higgs mass. this means that the abundance set by freeze-in will be IR-dominated, i.e. for $m_S < m_h/2$, the abundance freezes-in when $T \sim m_h/2$, because the dominating abundance comes from decays of on-shell Higgs bosons. This means that the relic abundance is independent of the scalar mass and thus the relic density scales as $\Omega_c h^2 \propto \lambda_{hs}^2 m_S$. I showed that the quantum statistical and thermal effects are mild, which is due to the fact that the abundance is predominantly produced when $T \sim m_h/2$ at which the quantum statistical and the thermal effects are mild. When $m_S > m_h/2$, on-shell $h \to SS$ is kinetically forbidden which means that the abundance is set by $2 \to 2$ scatterings and freeze-in when $T \sim m_S$. The relic abundance is thus $Y_S \propto m_S$, which means that the relic density is independent of the scalar mass. Since freeze-in happens when $T \sim m_S > m_h/2$, quantum statistical and thermal effects will be important because both W's, Z's, h's, and H's contribute to the abundance and will be more relativistic due to the high temperature. I showed that thermal effects also play an important role since the abundance is predominately produced when $T \gtrsim T_{\text{EW}}$ and since it is only the $HH \to SS$ channel that contributes to the abundance, it will be smaller than if EWSB is neglected. The thermal effects will counteract the quantum statistical effects because the thermal Higgs mass makes it less relativistic and thus reduces the size of the quantum statistical factors. Higher order effects are also seen to give a contribution when $2 \to 2$ scatterings dominate. When the scalar abundance is produced from on-shell Higgs decays, higher order effects are also mild since the dominant contribution to the abundance comes from the Higgs resonance. When thermal effects are neglected, I find that the effect becomes negligible when $m_s > 1.5\,\text{TeV}$ due to unitarization, since the tree-level result is used for $\sqrt{s} > 3\,\text{TeV}$. This happens earlier if thermal effects are included because the mass scale that enters is a factor $v_0/v(T)$ smaller. The abundance is also smaller because tree-level result is used for the process $HH \to SS$, including higher order effects for this process is expected to increase the abundance as is seen for the case when thermal effects are neglected.

The second case I looked at was a reheating temperature much smaller than the Higgs resonance ($T_R \ll m_h/2$). In this case the resulting abundance is produced

from $2 \rightarrow 2$ scatterings and is dependent on the reheating temperature, since it is predominantly produced when $T \simeq T_R$. Thermal effects can also be seen to be important when the reheating temperature is low enough such that decays from hadrons are negligible. This is because if the QCD phase transition is not included, decays from quarks will give a contribution that gives an abundance that can be a factor ~ 128 wrong. An important feature is that for low reheating temperature large coupling is needed to give the correct relic density required by the freeze-in mechanism, which means that some of the couplings considered in this analysis are already excluded.

The detailed study of this simple model shows how important it is to include thermal effects when studying DM abundances that are produced by the freeze-in mechanism. The main routines that facilitate what has been studied in this work will with be available with the next release of DarkSUSY. A lot of other models have particles that can be produced by the freeze-in mechanism. Including thermal effects for these models and studying the intricacies these effects will have on the DM abundance would be an interesting future project. Another interesting aspect to study is the intermediate region between freeze-in and freeze-out, i.e. the region between where the abundance is increasing and decreasing in figure 5.2. In this region the DM will thermalise, but too slowly to calculate the abundance assuming that the particle is a WIMP. However, this cannot yet be done with the existing routines in DarkSUSY, as it is not covered by the formalism introduced in section 5. Finally, if one includes that DM can self-interact, there are more effects such as dark freeze-out and reannihilation that would be interesting to study in terms of thermal effects and phase transitions.

Appendix A

Implementation in DarkSUSY

DarkSUSY [7] is a widely used FORTRAN package which is used to calculate properties of a variety of dark matter particles numerically. In 2018 DarkSUSY 6 [7] was released, which is a revamped version that focuses on modularity and no longer focuses solely on supersymmetric neutralino DM. By modularity I mean that the previously hard-coded Minimal Supersymmetric Standard Model (MSSM) routines are now independent of the particle physics model that is looked at and improved to look at WIMP-like particles in the early universe, DarkSUSY is thus one of the go-to packages to use for DM calculations. I have expanded DarkSUSY to also include a FIMP-like particle, whose routines will be described below. I start by a review of the structure of DarkSUSY, I will then outline the new routines and how to use them. For a more thorough review of DarkSUSY's functionalities, see Ref. [7].

DarkSUSY Structure

The structure of DarkSUSY is based on a set of routines contained in the library `ds_core` which is without any reference to a specific particle physics model, while all the particle physics information is contained in separate modules. This structure is very useful because this means that DarkSUSY can use the same routines on a variety of models. A key ingredient each particle physics module has to supply are so-called *interface functions*, which have pre-defined signatures and functionalities. If a main program that makes use of a routine in `ds_core` that has to use an interface function that is not provided by the particle physics module, then those routines will not compile, and an error will be displayed. Note that not all interface functions have to be provided by a particle physics module. The ones needed are determined when the user links the main program to these libraries, e.g. if a main program wished to calculate the relic density, $\Omega_c h^2$, of a WIMP, which is done by the routine `dsrdomega` found in `/src/rd`. The particle physics module has to provide the interface functions

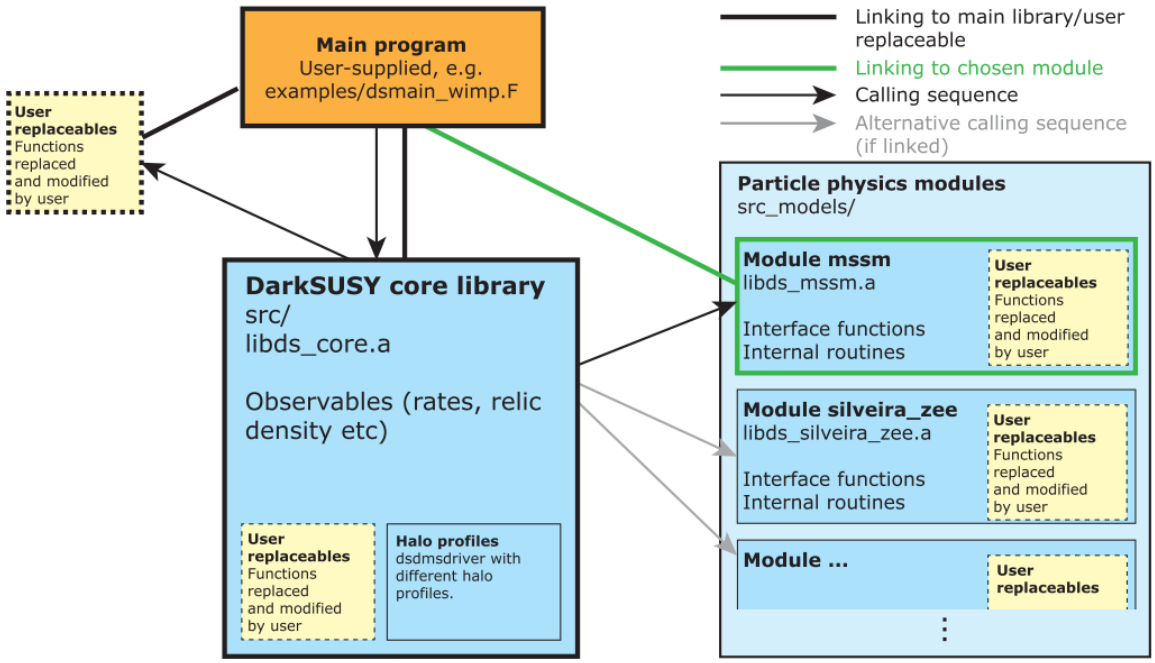

Figure A.1: Illustration of how DarkSUSY is used. Image taken from Ref. [7].

`dsanwx` and `dsrdparticles` which provides the effective invariant rate and the masses and internal degrees of freedom of the coannihilating particles and the location of possible resonances or thresholds in the effective invariant rate. Another key feature is the concept of *user replaceable functions*, which as the name indicates, are functions which the user can provide in order to replace any function in DarkSUSY. A conceptual illustration of how DarkSUSY is used is displayed in figure A.1.

I will now provide a short example on how this works in practice. Suppose you want to calculate the relic density for the scalar in the scalar singlet model where we suppose the scalar is a WIMP with the mass m_S and coupling λ_{hs}. When you compile your main program, you have to link it to the core library `src/libds_core.a`, this is represented by the black line between the box **Main program** and **DarkSUSY core library** in figure A.1. Linking our main program to the Silveira-Zee module is done by linking to `src/libds_silveira_zee.a`, this is represented by the green line in figure A.1. For an example on a make file that does this, see `examples/makefile`. If you would like to use any user replaceable, one would have to remember to include them as well at the linking stage. The main program must first include a call to the subroutine `dsinit` in order to initiate DarkSUSY. Then you would call the routine `dsgivemodel_silveira_zee` with λ_{hs} and m_S as parameters in order to initialize the scalar singlet model with coupling λ_{hs} and mass m_S. You would then call `dsmodelsetup`, which returns error flags if something went wrong with the initialization. We would now call the routine `dsrdomega` provided by `ds_core` to calculate the relic density. The routine would

then use `dsanwx` and `dsrdparticles` provided by the Silveira-Zee module (this is represented by the black arrows in figure A.1), or a user replaced function if linked. Compiling and running the program would now calculate the relic density. If we instead wanted to calculate the relic density one would get if the scalar was a FIMP we would have to use the routine `dsfi2to2oh2` which I will now introduce together with the other freeze-in routines.

The Freeze-in module

Most of the new routines for freeze-in calculations I have created for DarkSUSY reside in the folder `src/fi` and I have listed the routines used for relic density and abundance calculations in table A.1. The main routines I provide are the `dsfi2to2ab` and `dsfi2to2oh2` routines, which calculate the relic abundance resulting from $2 \to 2$ processes, $Y_\chi^{2\to 2}$ given by Eq.(5.18) and its resulting relic density $\Omega_c h^2$, respectively. These only need three inputs, $T_{\min}$ which is the lowest temperature assumed, T_R which is the reheating temperature and `statistis` which have to be set to 0 (1) to use Maxwell-Boltzmann distributions (Fermi-Dirac or Bose-Einstein distributions) for the SM particles, which is communicated by the particle physics module. All other parameters are given by using `dsrdparticles`. Both the `statistics` $= 0$ and `statistical` $= 1$ routine uses modified versions of `dsrdthav` which calculates $\langle \sigma v \rangle$ and resides in `src/rd`. `statistics` $= 0$ uses the function `dsrdthav_fi` which simply is the usual `dsrdthav` given by Eq.(4.22), but it will also integrate up to much higher momenta than one has to do when studying freeze-out. The `statistics` $= 1$ case uses the function `dsrdthav_plasma` which calculates Eq.(5.34). Numerically it is very similar to `dsrdthav_fi`, but it takes as input `dsanwx_plasma` instead of `dsanwx`, which uses that the cross section with no quantum statistical factors is replaced by the cross section with quantum statistical factors given by Eq.(5.35). The routines `dsfidecab` and `dsfidecoh2` calculate the relic abundance $Y_\chi^{1\to 2}$ and relic density $\Omega_c h^2$ coming from a $1 \to 2$ process, involving a particle s with mass m_s decaying with the width Γ_s. The routines takes as input $T_{\min}$, T_R and `statistics` which is the same as for the $2 \to 2$ process, but it also has to get the inputs m_s, Γ_s and ε_s. Future implementations will either include a routine to find s-channel resonances (thus using $1 \to 2$) or let the particle physics modules give this information. The $1 \to 2$ routines use Eq.(5.47) if `statistics` $= 0$ and the replacement given in Eq.(5.48) if `statistics` $= 1$. Finally, the function `dsfi2to2dYdx` calculates the value for $\frac{dY_\chi^{2\to 2}}{dx}$ and its input is $x = m_\chi/T$ and `statistics`.

For the scalar singlet model, found in the folder `src_models/silveira_zee`, I created and added various needed functions and effects. The expression for `dsanwx_plasma` has been added by using Eq.(5.36). I made the function `dsanGbar` which returns the value for $\bar{G}$ given by Eq.(5.39) and it is used in `dsanwx_plasma`. The temperatures effects described and used in chapter 6 and 8 has been implemented

Routine	Description
`dsfi2to2ab`	Calculates the relic abundance $Y_\chi^{2\to2}$ for a FIMP produced from $2 \to 2$ processes, using Eq.(5.18).
`dsfi2to2oh2`	Calculates $\Omega_c h^2$ for $2 \to 2$ processes using Eq.(4.24) and `dsfi2to2ab` to provide $Y_\chi^{2\to2}$
`dsfidecab`	Calculates the relic abundance $Y_\chi^{1\to2}$ for a FIMP produced from $1 \to 2$ processes, using Eq.(5.47) when Maxwell-Boltzmann is assumed and uses the replacement given by Eq(5.48) when Fermi-Dirac- or Bose-Einstein distribution is used.
`dsfidecoh2`	Calculates $\Omega_c h^2$ for $1 \to 2$ processes using Eq.(4.24) and `dsfidecab` to provide $Y_\chi^{1\to2}$.
`dsfi2to2dYdx`	Calculates $\frac{dY_\chi^{2\to2}}{dx}$ as a function of x.

Table A.1: Freeze-in routines located in the folder `src/fi` that are used to calculate the relic- abundance and density for $1 \to 2$ and $2 \to 2$ processes, as well as dY/dx.

in the functions `dsanwx` and `dsanwx_plasma`. In order to include the thermal effects, one has to change the value of `phase_par` whose default is 1, to `phase_par` $= 2$. It is found in `ini/dsinit_module`. In order to let the model know what the temperature is, one has to call the subroutine `dsgivemodel_temp`. If the temperature $T > T_c = 163$ GeV, then EWSB has not yet happened and the only process we have is $HH \to SS$. The thermal mass for the Higgs given by Eq.(6.42) is then used and the cross section for $SS \to HH$ is given by Eq.(7.10). If $T_c > T > T_{\rm QCD}$ we use the broken theory with the thermal vev and thermal Higgs mass calculated numerically and tabulated, these tabulations can be found in the folder `/data` with the names `vev_temp.dat` and `mh_temp.dat`. When $T < T_{\rm QCD}$ it is used that Higgs decays to free quarks no longer happen and decays to hadrons are used instead. This decay width is given by the function `dssmgammah_hadron_tab`, which uses the tabulated result found in Ref. [137]. Finally, the unitarization procedure outlined in section 7.2 has been implemented and can be turned on by setting the value of `unitar` to 2, this is also found in `ini/dsinit_module`. All of these functions have been used to make the plots displayed in chapter 8. The numerical stability has been well tested for the mass ranges and temperatures displayed in 8, and provides physically sensible results, as discussed in the main body of the thesis. However, this implementation is only preliminary, and the routines will form the basis of new capability of DarkSUSY to perform freeze-in calculations, to be released as DarkSUSY 6.3.

Appendix B

On-shell Higgs decay

In this appendix I will show that when the freeze-in relic abundance is calculated using $2 \to 2$ scatterings and we have an s-channel resonance, we will have that $Y^{\chi}_{1\to 2} = Y^{\chi}_{2\to 2}$ if Maxwell-Boltzmann distributions are assumed. The relic abundance for $2 \to 2$ scatterings are given by Eq.(5.18) and the thermally averaged cross section is given by Eq.(4.22). Since the $1 \to 2$ abundance is produced from decay of on-shell particles, I believe that setting the mediator almost on-shell will give the same result. I will use the narrow width approximation (NWA), which for the process $\chi\bar{\chi} \to Y \to 1, 2$ is (see further down for proof):

$$\sigma^{\text{NWA}}(s) = \frac{g_Y}{g_\chi^2} \frac{16\pi^2 m_Y^2}{\sqrt{s}(s - 4m_\chi^2)} N_\chi \Gamma_{Y\to\chi\bar{\chi}} \text{Br}(Y \to 1, 2)\delta(s - m_Y^2) \ . \tag{B.1}$$

Rewriting Eq.(5.18) using Eq.(4.22) gives us (for the process $1, 2 \to \chi$):

$$Y_{2\to 2} = \frac{g_\chi^2}{32\pi^4} \int_{T_0}^{T_R} \int_{4m_\chi^2}^{\infty} \frac{dT ds}{\overline{H} s(T)} \sigma_{\chi\bar{\chi}\to 1,2}(s - 4m_\chi^2)\sqrt{s} K_1(\sqrt{s}/T) \ . \tag{B.2}$$

Using Eq.(B.1) to rewrite the cross-section gives us:

$$Y_{2\to 2 \text{ on-shell}} = \frac{g_Y}{2\pi^2} m_Y^2 N_\chi \Gamma_{Y\to\chi\bar{\chi}} \text{Br}(Y \to 1, 2) \int_{T_0}^{T_R} \frac{dT}{\overline{H} s(T)} K_1(m_Y/T) \ . \tag{B.3}$$

Summing over all the channels will result in summing all the branching ratios, which gives us:

$$Y_{2\to 2 \text{ on-shell}} = \frac{g_Y N_\chi}{2\pi^2} m_Y^2 \Gamma_{Y\to\chi\bar{\chi}} \int_{T_0}^{T_R} \frac{dT}{\overline{H} s(T)} K_1(m_Y/T) \ , \tag{B.4}$$

which is Eq.(5.47). Hence, the $1 \to 2$ abundance and the $2 \to 2$ abundance with an almost on-shell mediator will give the same result, which is why I have used the $2 \to 2$ result in the main body of this thesis. This argument relies however crucially on the MB distribution. Including quantum statistics would mean that finite temperature field theory has to be used, which is beyond the scope of this thesis.

B.1 Proof for NWA

Using that the mediator is on-shell, I use the usual Breit-Wigner distribution. This means that the propagator squared becomes

$$\left|\frac{i}{s-m_Y^2+im_Y\Gamma_{\rm tot}}\right|^2=\frac{1}{(s-m_Y^2)^2+m_Y^2\Gamma_{\rm tot}^2}\approx\frac{\pi}{m_Y\Gamma_{\rm tot}}\delta(s-m_Y^2)\ , \tag{B.5}$$

where in the last step the limit $\Gamma_{\rm tot}/M_Y\to 0$ is used. This means that the cross section becomes

$$4Fg_\chi^2\sigma(\chi\bar{\chi}\to Y\to 1,2)=\frac{2\pi}{\Gamma_{\rm tot}}\sum_{\rm spin}\left|\mathcal{M}_{\chi\bar{\chi}\to Y}\right|^2 g_Y\Gamma_{Y\to 1,2}\delta(s-m_Y^2)\ , \tag{B.6}$$

where F is the Møller flux factor and g_χ^2 comes from averaging over spins. N_{12}^{-1} is a symmetry factor taking into account if particle 1 and 2 are self-conjugate ($N_{12}=1$) or not ($N_{12}=2$). Now I use that

$$\Gamma_{Y\to\chi\bar{\chi}}=N_\chi^{-1}\frac{\sum_{\rm spin}\frac{1}{g_Y}\left|\mathcal{M}_{\chi\bar{\chi}\to Y}\right|^2}{8\pi m_Y^2}|p|\Rightarrow\sum_{\rm spin}\left|\mathcal{M}_{\chi\bar{\chi}\to Y}\right|^2=\frac{8\pi g_\chi N_\chi\Gamma_{Y\to\chi\bar{\chi}}m_Y^2}{|p|}\ , \tag{B.7}$$

thus continuing, using that $|p_{\chi\bar{\chi}}|=\frac{1}{2}\sqrt{s-4m_\chi^2}$, we get:

$$\sigma^{\rm NWA}(s)=\frac{g_Y}{g_\chi^2}\frac{16\pi^2m_Y^2N_\chi\Gamma_{Y\to\chi\bar{\chi}}}{\sqrt{s}(s-4m_\chi^2)}{\rm Br}(Y\to 1,2)\delta(s-m_Y^2)\ . \tag{B.8}$$

This result enters in Eq.(B.3).

Bibliography

[1] N. Aghanim et al. 'Planck 2018 results. VI. Cosmological parameters'. In: (July 2018). arXiv: 1807.06209 [astro-ph.CO].

[2] Leszek Roszkowski, Enrico Maria Sessolo and Sebastian Trojanowski. 'WIMP dark matter candidates and searches—current status and future prospects'. In: *Rept. Prog. Phys.* 81.6 (2018), p. 066201. DOI: 10.1088/1361-6633/aab913. arXiv: 1707.06277 [hep-ph].

[3] Giorgio Arcadi et al. 'The waning of the WIMP? A review of models, searches, and constraints'. In: *Eur. Phys. J. C* 78.3 (2018), p. 203. DOI: 10.1140/epjc/s10052-018-5662-y. arXiv: 1703.07364 [hep-ph].

[4] Edward W Kolb and Michael Turner. *The early universe*. CRC Press, 2018.

[5] Lawrence J. Hall et al. 'Freeze-In Production of FIMP Dark Matter'. In: *JHEP* 03 (2010), p. 080. DOI: 10.1007/JHEP03(2010)080. arXiv: 0911.1120 [hep-ph].

[6] Vanda Silveira and A. Zee. 'SCALAR PHANTOMS'. In: *Phys. Lett. B* 161 (1985), pp. 136–140. DOI: 10.1016/0370-2693(85)90624-0.

[7] Torsten Bringmann et al. 'DarkSUSY 6 : An Advanced Tool to Compute Dark Matter Properties Numerically'. In: *JCAP* 07 (2018), p. 033. DOI: 10.1088/1475-7516/2018/07/033. arXiv: 1802.03399 [hep-ph].

[8] Sean M. Carroll. *Spacetime and Geometry*. Cambridge University Press, July 2019. ISBN: 978- 1-292-02663-3.

[9] Viatcheslav Mukhanov. *Physical Foundations of Cosmology*. Cambridge University Press, 2005.

[10] F. Zwicky. 'Die Rotverschiebung von extragalaktischen Nebeln'. In: *Helv. Phys. Acta* 6 (1933), pp. 110–127. DOI: 10.1007/s10714-008-0707-4.

[11] Sinclair Smith. 'The Mass of the Virgo Cluster'. In: *Astrophys. J.* 83 (1936), pp. 23–30. DOI: 10.1086/143697.

[12] Vera C. Rubin and Jr. Ford W.Kent. 'Rotation of the Andromeda Nebula from a Spectroscopic Survey of Emission Regions'. In: *Astrophys. J.* 159 (1970), pp. 379–403. DOI: 10.1086/150317.

[13] V.C. Rubin, N. Thonnard and Jr. Ford W.K. 'Rotational properties of 21 SC galaxies with a large range of luminosities and radii, from NGC 4605 /R = 4kpc/ to UGC 2885 /R = 122 kpc/'. In: *Astrophys. J.* 238 (1980), p. 471. DOI: 10.1086/158003.

[14] Mordehai Milgrom. 'The MOND paradigm'. In: (Jan. 2008). arXiv: 0801.3133 [astro-ph].

[15] Arno A. Penzias and Robert Woodrow Wilson. 'A Measurement of excess antenna temperature at 4080-Mc/s'. In: *Astrophys. J.* 142 (1965), pp. 419–421. DOI: 10.1086/148307.

[16] G. Hinshaw et al. 'NINE-YEAR WILKINSON MICROWAVE ANISOTROPY PROBE (WMAP) OBSERVATIONS: COSMOLOGICAL PARAMETER RESULTS'. In: *The Astrophysical Journal Supplement Series* 208.2 (Sept. 2013), p. 19. ISSN: 1538-4365. DOI: 10.1088/0067-0049/208/2/19. URL: http://dx.doi.org/10.1088/0067-0049/208/2/19.

[17] Matthias Bartelmann. 'Gravitational Lensing'. In: *Class. Quant. Grav.* 27 (2010), p. 233001. DOI: 10.1088/0264-9381/27/23/233001. arXiv: 1010.3829 [astro-ph.CO].

[18] Douglas Clowe et al. 'A direct empirical proof of the existence of dark matter'. In: *Astrophys. J. Lett.* 648 (2006), pp. L109–L113. DOI: 10.1086/508162. arXiv: astro-ph/0608407.

[19] Joel R. Primack. 'Dark matter and structure formation'. In: *Midrasha Mathematicae in Jerusalem: Winter School in Dynamical Systems*. July 1997. arXiv: astro-ph/9707285.

[20] Michael Boylan-Kolchin et al. 'Resolving cosmic structure formation with the Millennium-II Simulation'. In: *Monthly Notices of the Royal Astronomical Society* 398.3 (Sept. 2009), pp. 1150–1164. ISSN: 1365-2966. DOI: 10.1111/j.1365-2966.2009.15191.x. URL: http://dx.doi.org/10.1111/j.1365-2966.2009.15191.x.

[21] Marco Taoso, Gianfranco Bertone and Antonio Masiero. 'Dark Matter Candidates: A Ten-Point Test'. In: *JCAP* 03 (2008), p. 022. DOI: 10.1088/1475-7516/2008/03/022. arXiv: 0711.4996 [astro-ph].

[22] R. D. Peccei and Helen R. Quinn. 'CP Conservation in the Presence of Instantons'. In: *Phys. Rev. Lett.* 38 (1977), pp. 1440–1443. DOI: 10.1103/PhysRevLett.38.1440.

[23] Leanne D. Duffy and Karl van Bibber. 'Axions as Dark Matter Particles'. In: *New J. Phys.* 11 (2009), p. 105008. DOI: 10.1088/1367-2630/11/10/105008. arXiv: 0904.3346 [hep-ph].

[24] Luca Di Luzio et al. 'The landscape of QCD axion models'. In: *Phys. Rept.* 870 (2020), pp. 1–117. DOI: 10.1016/j.physrep.2020.06.002. arXiv: 2003.01100 [hep-ph].

[25] A. Boyarsky et al. 'Sterile neutrino Dark Matter'. In: *Prog. Part. Nucl. Phys.* 104 (2019), pp. 1–45. DOI: 10.1016/j.ppnp.2018.07.004. arXiv: 1807.07938 [hep-ph].

[26] Anirban Biswas and Aritra Gupta. 'Freeze-in Production of Sterile Neutrino Dark Matter in $U(1)_{B-L}$ Model'. In: *JCAP* 09 (2016). [Addendum: JCAP 05, A01 (2017)], p. 044. DOI: 10.1088/1475-7516/2016/09/044. arXiv: 1607.01469 [hep-ph].

[27] Manuel Drees and Fazlollah Hajkarim. 'Neutralino Dark Matter in Scenarios with Early Matter Domination'. In: *JHEP* 12 (2018), p. 042. DOI: 10.1007/JHEP12(2018)042. arXiv: 1808.05706 [hep-ph].

[28] Ken Osato et al. 'Cosmological Constraint on the Light Gravitino Mass from CMB Lensing and Cosmic Shear'. In: *JCAP* 06 (2016), p. 004. DOI: 10.1088/1475-7516/2016/06/004. arXiv: 1601.07386 [astro-ph.CO].

[29] Karim Benakli et al. 'Minimal model of gravitino dark matter'. In: *Phys. Rev. D* 95.9 (2017), p. 095002. DOI: 10.1103/PhysRevD.95.095002. arXiv: 1701.06574 [hep-ph].

[30] Bernard Carr and Florian Kuhnel. 'Primordial Black Holes as Dark Matter: Recent Developments'. In: (June 2020). DOI: 10.1146/annurev-nucl-050520-125911. arXiv: 2006.02838 [astro-ph.CO].

[31] Nicolás Bernal et al. 'The Dawn of FIMP Dark Matter: A Review of Models and Constraints'. In: *Int. J. Mod. Phys. A* 32.27 (2017), p. 1730023. DOI: 10.1142/S0217751X1730023X. arXiv: 1706.07442 [hep-ph].

[32] Scott Dodelson and Lawrence M. Widrow. 'Sterile-neutrinos as dark matter'. In: *Phys. Rev. Lett.* 72 (1994), pp. 17–20. DOI: 10.1103/PhysRevLett.72.17. arXiv: hep-ph/9303287.

[33] M. Drewes et al. 'A White Paper on keV Sterile Neutrino Dark Matter'. In: *JCAP* 01 (2017), p. 025. DOI: 10.1088/1475-7516/2017/01/025. arXiv: 1602.04816 [hep-ph].

[34] Bibhushan Shakya. 'Sterile Neutrino Dark Matter from Freeze-In'. In: *Mod. Phys. Lett. A* 31.06 (2016), p. 1630005. DOI: 10.1142/S0217732316300056. arXiv: 1512.02751 [hep-ph].

[35] Sean Tulin and Hai-Bo Yu. 'Dark Matter Self-interactions and Small Scale Structure'. In: *Phys. Rept.* 730 (2018), pp. 1–57. DOI: 10.1016/j.physrep.2017.11.004. arXiv: 1705.02358 [hep-ph].

[36] Björn Penning. 'The pursuit of dark matter at colliders—an overview'. In: *J. Phys. G* 45.6 (2018), p. 063001. DOI: 10.1088/1361-6471/aabea7. arXiv: 1712.01391 [hep-ex].

[37] David G. Cerdeno and Anne M. Green. 'Direct detection of WIMPs'. In: (Feb. 2010), pp. 347–369. arXiv: 1002.1912 [astro-ph.CO].

[38] Thomas Hambye et al. 'Dark matter direct detection is testing freeze-in'. In: *Phys. Rev. D* 98.7 (2018), p. 075017. DOI: 10.1103/PhysRevD.98.075017. arXiv: 1807.05022 [hep-ph].

[39] R. Bernabei et al. 'First model independent results from DAMA/LIBRA-phase2'. In: *Nucl. Phys. Atom. Energy* 19.4 (2018), pp. 307–325. DOI: 10.15407/jnpae2018.04.307. arXiv: 1805.10486 [hep-ex].

[40] E. Aprile et al. 'Dark Matter Search Results from a One Ton-Year Exposure of XENON1T'. In: *Phys. Rev. Lett.* 121.11 (2018), p. 111302. DOI: 10.1103/PhysRevLett.121.111302. arXiv: 1805.12562 [astro-ph.CO].

[41] D. S. Akerib et al. 'Results from a search for dark matter in the complete LUX exposure'. In: *Phys. Rev. Lett.* 118.2 (2017), p. 021303. DOI: 10.1103/PhysRevLett.118.021303. arXiv: 1608.07648 [astro-ph.CO].

[42] Andi Tan et al. 'Dark Matter Results from First 98.7 Days of Data from the PandaX-II Experiment'. In: *Phys. Rev. Lett.* 117.12 (2016), p. 121303. DOI: 10.1103/PhysRevLett.117.121303. arXiv: 1607.07400 [hep-ex].

[43] D. W. Amaral et al. 'Constraints on low-mass, relic dark matter candidates from a surface-operated SuperCDMS single-charge sensitive detector'. In: *Phys. Rev. D* 102.9 (2020), p. 091101. DOI: 10.1103/PhysRevD.102.091101. arXiv: 2005.14067 [hep-ex].

[44] Liron Barak et al. 'SENSEI: Direct-Detection Results on sub-GeV Dark Matter from a New Skipper-CCD'. In: *Phys. Rev. Lett.* 125.17 (2020), p. 171802. DOI: 10.1103/PhysRevLett.125.171802. arXiv: 2004.11378 [astro-ph.CO].

[45] Torsten Bringmann. 'Indirect dark matter searches: A mini-review'. In: *PoS* EPS-HEP2011 (2011), p. 061. DOI: 10.22323/1.134.0061.

[46] Michael Gustafsson et al. 'Significant Gamma Lines from Inert Higgs Dark Matter'. In: *Phys. Rev. Lett.* 99 (2007), p. 041301. DOI: 10.1103/PhysRevLett.99.041301. arXiv: astro-ph/0703512.

[47] Torbjorn Sjostrand, Stephen Mrenna and Peter Z. Skands. 'PYTHIA 6.4 Physics and Manual'. In: *JHEP* 05 (2006), p. 026. DOI: 10.1088/1126-6708/2006/05/026. arXiv: hep-ph/0603175.

[48] Torsten Bringmann and Christoph Weniger. 'Gamma Ray Signals from Dark Matter: Concepts, Status and Prospects'. In: *Phys. Dark Univ.* 1 (2012), pp. 194–217. DOI: 10.1016/j.dark.2012.10.005. arXiv: 1208.5481 [hep-ph].

[49] Tracy R. Slatyer. 'Indirect Detection of Dark Matter'. In: *Theoretical Advanced Study Institute in Elementary Particle Physics: Anticipating the Next Discoveries in Particle Physics*. Oct. 2017. DOI: 10.1142/9789813233348_0005. arXiv: 1710.05137 [hep-ph].

[50] Lisa Goodenough and Dan Hooper. 'Possible Evidence For Dark Matter Annihilation In The Inner Milky Way From The Fermi Gamma Ray Space Telescope'. In: (Oct. 2009). arXiv: 0910.2998 [hep-ph].

[51] M. Ajello et al. 'Fermi-LAT Observations of High-Energy γ-Ray Emission Toward the Galactic Center'. In: *Astrophys. J.* 819.1 (2016), p. 44. DOI: 10.3847/0004-637X/819/1/44. arXiv: 1511.02938 [astro-ph.HE].

[52] Jovana Petrović, Pasquale Dario Serpico and Gabrijela Zaharijaš. 'Galactic Center gamma-ray "excess" from an active past of the Galactic Centre?' In: *JCAP* 10 (2014), p. 052. DOI: 10.1088/1475-7516/2014/10/052. arXiv: 1405.7928 [astro-ph.HE].

[53] F. Calore, M. Di Mauro and F. Donato. 'Diffuse gamma-ray emission from galactic pulsars'. In: *Astrophys. J.* 796 (2014), p. 1. DOI: 10.1088/0004-637X/796/1/14. arXiv: 1406.2706 [astro-ph.HE].

[54] Ilias Cholis, Dan Hooper and Tim Linden. 'Challenges in Explaining the Galactic Center Gamma-Ray Excess with Millisecond Pulsars'. In: *JCAP* 06 (2015), p. 043. DOI: 10.1088/1475-7516/2015/06/043. arXiv: 1407.5625 [astro-ph.HE].

[55] A. Albert et al. 'Searching for Dark Matter Annihilation in Recently Discovered Milky Way Satellites with Fermi-LAT'. In: *Astrophys. J.* 834.2 (2017), p. 110. DOI: 10.3847/1538-4357/834/2/110. arXiv: 1611.03184 [astro-ph.HE].

[56] Torsten Bringmann, Martin Vollmann and Christoph Weniger. 'Updated cosmic-ray and radio constraints on light dark matter: Implications for the GeV gamma-ray excess at the Galactic center'. In: *Phys. Rev. D* 90.12 (2014), p. 123001. DOI: 10.1103/PhysRevD.90.123001. arXiv: 1406.6027 [astro-ph.HE].

[57] L. Struder et al. 'The European Photon Imaging Camera on XMM-Newton: The pn-CCD camera'. In: *Astron. Astrophys.* 365 (2001), pp. L18–26. DOI: 10.1051/0004-6361:20000066.

[58] Martin J. L. Turner et al. 'The European Photon Imaging Camera on XMM-Newton: The MOS cameras'. In: *Astron. Astrophys.* 365 (2001), pp. L27–35. DOI: 10.1051/0004-6361:20000087. arXiv: astro-ph/0011498.

[59] Esra Bulbul et al. 'Detection of An Unidentified Emission Line in the Stacked X-ray spectrum of Galaxy Clusters'. In: *Astrophys. J.* 789 (2014), p. 13. DOI: 10.1088/0004-637X/789/1/13. arXiv: 1402.2301 [astro-ph.CO].

[60] M. Aguilar et al. 'Antiproton Flux, Antiproton-to-Proton Flux Ratio, and Properties of Elementary Particle Fluxes in Primary Cosmic Rays Measured with the Alpha Magnetic Spectrometer on the International Space Station'. In: *Phys. Rev. Lett.* 117.9 (2016), p. 091103. DOI: 10.1103/PhysRevLett.117.091103.

[61] Alessandro Cuoco, Michael Krämer and Michael Korsmeier. 'Novel Dark Matter Constraints from Antiprotons in Light of AMS-02'. In: *Phys. Rev. Lett.* 118.19 (2017), p. 191102. DOI: 10.1103/PhysRevLett.118.191102. arXiv: 1610.03071 [astro-ph.HE].

[62] Gaëlle Giesen et al. 'AMS-02 antiprotons, at last! Secondary astrophysical component and immediate implications for Dark Matter'. In: *JCAP* 09 (2015), p. 023. DOI: 10.1088/1475-7516/2015/9/023. arXiv: 1504.04276 [astro-ph.HE].

[63] Oscar Adriani et al. 'An anomalous positron abundance in cosmic rays with energies 1.5-100 GeV'. In: *Nature* 458 (2009), pp. 607–609. DOI: 10.1038/nature07942. arXiv: 0810.4995 [astro-ph].

[64] M. Aguilar et al. 'First Result from the Alpha Magnetic Spectrometer on the International Space Station: Precision Measurement of the Positron Fraction in Primary Cosmic Rays of 0.5–350 GeV'. In: *Phys. Rev. Lett.* 110 (14 Apr. 2013), p. 141102. DOI: 10.1103/PhysRevLett.110.141102. URL: https://link.aps.org/doi/10.1103/PhysRevLett.110.141102.

[65] M. Ackermann et al. 'Measurement of Separate Cosmic-Ray Electron and Positron Spectra with the Fermi Large Area Telescope'. In: *Physical Review Letters* 108.1 (Jan. 2012). ISSN: 1079-7114. DOI: 10.1103/physrevlett.108.011103. URL: http://dx.doi.org/10.1103/PhysRevLett.108.011103.

[66] Dan Hooper, Pasquale Blasi and Pasquale Dario Serpico. 'Pulsars as the Sources of High Energy Cosmic Ray Positrons'. In: *JCAP* 01 (2009), p. 025. DOI: 10.1088/1475-7516/2009/01/025. arXiv: 0810.1527 [astro-ph].

[67] M. Di Mauro et al. 'Interpretation of AMS-02 electrons and positrons data'. In: *JCAP* 04 (2014), p. 006. DOI: 10.1088/1475-7516/2014/04/006. arXiv: 1402.0321 [astro-ph.HE].

[68] A. Arbey and F. Mahmoudi. 'Dark matter and the early Universe: a review'. In: (Apr. 2021). DOI: 10.1016/j.ppnp.2021.103865. arXiv: 2104.11488 [hep-ph].

[69] Felix Kahlhoefer. 'Review of LHC Dark Matter Searches'. In: *Int. J. Mod. Phys. A* 32.13 (2017), p. 1730006. DOI: 10.1142/S0217751X1730006X. arXiv: 1702.02430 [hep-ph].

[70] 'Combination of searches for invisible Higgs boson decays with the ATLAS experiment'. In: (Oct. 2020).

[71] Vardan Khachatryan et al. 'Searches for invisible decays of the Higgs boson in pp collisions at $\sqrt{s} = 7$, 8, and 13 TeV'. In: *JHEP* 02 (2017), p. 135. DOI: 10.1007/JHEP02(2017)135. arXiv: 1610.09218 [hep-ex].

[72] Joel R. Primack and David B. Cline. 'Cosmology: Small Scale Issues'. In: *AIP Conference Proceedings* (2009). DOI: 10.1063/1.3232194. URL: http://dx.doi.org/10.1063/1.3232194.

[73] David N. Spergel and Paul J. Steinhardt. 'Observational Evidence for Self-Interacting Cold Dark Matter'. In: *Physical Review Letters* 84.17 (Apr. 2000), pp. 3760–3763. ISSN: 1079-7114. DOI: 10.1103/physrevlett.84.3760. URL: http://dx.doi.org/10.1103/PhysRevLett.84.3760.

[74] Sean Tulin and Hai-Bo Yu. 'Dark matter self-interactions and small scale structure'. In: *Physics Reports* 730 (Feb. 2018), pp. 1–57. ISSN: 0370-1573. DOI: 10.1016/j.physrep.2017.11.004. URL: http://dx.doi.org/10.1016/j.physrep.2017.11.004.

[75] Ricardo A. Flores and Joel R. Primack. 'Observational and theoretical constraints on singular dark matter halos'. In: *The Astrophysical Journal* 427 (May 1994), p. L1. ISSN: 1538-4357. DOI: 10.1086/187350. URL: http://dx.doi.org/10.1086/187350.

[76] Michael Boylan-Kolchin, James S. Bullock and Manoj Kaplinghat. 'Too big to fail? The puzzling darkness of massive Milky Way subhaloes'. In: *Monthly Notices of the Royal Astronomical Society: Letters* 415.1 (June 2011), pp. L40–L44. ISSN: 1745-3925. DOI: 10.1111/j.1745-3933.2011.01074.x. URL: http://dx.doi.org/10.1111/j.1745-3933.2011.01074.x.

[77] Kyle A. Oman et al. 'The unexpected diversity of dwarf galaxy rotation curves'. In: *Monthly Notices of the Royal Astronomical Society* 452.4 (Aug. 2015), pp. 3650–3665. ISSN: 1365-2966. DOI: 10.1093/mnras/stv1504. URL: http://dx.doi.org/10.1093/mnras/stv1504.

[78] Ben Moore et al. 'Dark Matter Substructure within Galactic Halos'. In: *The Astrophysical Journal* 524.1 (Oct. 1999), pp. L19–L22. ISSN: 0004-637X. DOI: 10.1086/312287. URL: http://dx.doi.org/10.1086/312287.

[79] B. Moore. 'Evidence against dissipationless dark matter from observations of galaxy haloes'. In: *Nature* 370 (1994), p. 629. DOI: 10.1038/370629a0.

[80] Julio F. Navarro, Carlos S. Frenk and Simon D. M. White. 'A Universal Density Profile from Hierarchical Clustering'. In: *The Astrophysical Journal* 490.2 (Dec. 1997), pp. 493–508. ISSN: 1538-4357. DOI: 10.1086/304888. URL: http://dx.doi.org/10.1086/304888.

[81] W. J. G. de Blok. 'The Core-Cusp Problem'. In: *Advances in Astronomy* 2010 (2010), pp. 1–14. ISSN: 1687-7977. DOI: 10.1155/2010/789293. URL: http://dx.doi.org/10.1155/2010/789293.

[82] Se-Heon Oh et al. 'High-resolution mass models of dwarf galaxies from LITTLE THINGS'. In: *Astron. J.* 149 (2015), p. 180. DOI: 10.1088/0004-6256/149/6/180. arXiv: 1502.01281 [astro-ph.GA].

[83] Manoj Kaplinghat, Sean Tulin and Hai-Bo Yu. 'Dark Matter Halos as Particle Colliders: Unified Solution to Small-Scale Structure Puzzles from Dwarfs to Clusters'. In: *Phys. Rev. Lett.* 116.4 (2016), p. 041302. DOI: 10.1103/PhysRevLett.116.041302. arXiv: 1508.03339 [astro-ph.CO].

[84] Ayuki Kamada et al. 'How the Self-Interacting Dark Matter Model Explains the Diverse Galactic Rotation Curves'. In: *Phys. Rev. Lett.* 119.11 (2017), p. 111102. DOI: 10.1103/PhysRevLett.119.111102. arXiv: 1611.02716 [astro-ph.GA].

[85] Shea Garrison-Kimmel et al. 'Too big to fail in the Local Group'. In: *Monthly Notices of the Royal Astronomical Society* 444.1 (Aug. 2014), pp. 222–236. ISSN: 1365-2966. DOI: 10.1093/mnras/stu1477. URL: http://dx.doi.org/10.1093/mnras/stu1477.

[86] Michael Boylan-Kolchin, James S. Bullock and Manoj Kaplinghat. 'The Milky Way's bright satellites as an apparent failure of ΛCDM'. In: *Monthly Notices of the Royal Astronomical Society* 422.2 (Mar. 2012), pp. 1203–1218. ISSN: 0035-8711. DOI: 10.1111/j.1365-2966.2012.20695.x. URL: http://dx.doi.org/10.1111/j.1365-2966.2012.20695.x.

[87] Kyle A. Oman et al. 'Missing dark matter in dwarf galaxies?' In: *Monthly Notices of the Royal Astronomical Society* 460.4 (May 2016), pp. 3610–3623. ISSN: 1365-2966. DOI: 10.1093/mnras/stw1251. URL: http://dx.doi.org/10.1093/mnras/stw1251.

[88] Anatoly Klypin et al. 'Where Are the Missing Galactic Satellites?' In: *The Astrophysical Journal* 522.1 (Sept. 1999), pp. 82–92. ISSN: 1538-4357. DOI: 10.1086/307643. URL: http://dx.doi.org/10.1086/307643.

[89] Azadeh Fattahi et al. *The cold dark matter content of Galactic dwarf spheroidals: no cores, no failures, no problem.* 2016. arXiv: 1607.06479 [astro-ph.GA].

[90] Till Sawala et al. 'The APOSTLE simulations: solutions to the Local Group's cosmic puzzles'. In: *Monthly Notices of the Royal Astronomical Society* 457.2 (Feb. 2016), pp. 1931–1943. ISSN: 1365-2966. DOI: 10.1093/mnras/stw145. URL: http://dx.doi.org/10.1093/mnras/stw145.

[91] Mei-Yu Wang et al. 'Cosmological simulations of decaying dark matter: implications for small-scale structure of dark matter haloes'. In: *Monthly Notices of the Royal Astronomical Society* 445.1 (Sept. 2014), pp. 614–629. ISSN: 1365-2966. DOI: 10.1093/mnras/stu1747. URL: http://dx.doi.org/10.1093/mnras/stu1747.

[92] Paul Bode, Jeremiah P. Ostriker and Neil Turok. 'Halo formation in warm dark matter models'. In: *Astrophys. J.* 556 (2001), pp. 93–107. DOI: 10.1086/321541. arXiv: astro-ph/0010389.

[93] Jesper Sommer-Larsen and Alexandre Dolgov. 'Formation of Disk Galaxies: Warm Dark Matter and the Angular Momentum Problem'. In: *The Astrophysical Journal* 551.2 (Apr. 2001), pp. 608–623. ISSN: 1538-4357. DOI: 10.1086/320211. URL: http://dx.doi.org/10.1086/320211.

[94] Manoj Kaplinghat, Sean Tulin and Hai-Bo Yu. 'Dark Matter Halos as Particle Colliders: Unified Solution to Small-Scale Structure Puzzles from Dwarfs to Clusters'. In: *Physical Review Letters* 116.4 (Jan. 2016). ISSN: 1079-7114. DOI: 10.1103/physrevlett.116.041302. URL: http://dx.doi.org/10.1103/PhysRevLett.116.041302.

[95] D. Harvey et al. 'The nongravitational interactions of dark matter in colliding galaxy clusters'. In: *Science* 347.6229 (Mar. 2015), pp. 1462–1465. ISSN: 1095-9203. DOI: 10.1126/science.1261381. URL: http://dx.doi.org/10.1126/science.1261381.

[96] Scott W. Randall et al. 'Constraints on the Self-Interaction Cross-Section of Dark Matter from Numerical Simulations of the Merging Galaxy Cluster 1E 0657-56'. In: *Astrophys. J.* 679 (2008), pp. 1173–1180. DOI: 10.1086/587859. arXiv: 0704.0261 [astro-ph].

[97] Andrew Robertson, Richard Massey and Vincent Eke. 'What does the Bullet Cluster tell us about self-interacting dark matter?' In: *Monthly Notices of the Royal Astronomical Society* 465.1 (Oct. 2016), pp. 569–587. ISSN: 1365-2966. DOI: 10.1093/mnras/stw2670. URL: http://dx.doi.org/10.1093/mnras/stw2670.

[98] Stacy Y. Kim, Annika H. G. Peter and David Wittman. 'In the wake of dark giants: new signatures of dark matter self-interactions in equal-mass mergers of galaxy clusters'. In: *Monthly Notices of the Royal Astronomical Society* 469.2 (Apr. 2017), pp. 1414–1444. ISSN: 1365-2966. DOI: 10.1093/mnras/stx896. URL: http://dx.doi.org/10.1093/mnras/stx896.

[99] David N. Spergel and Paul J. Steinhardt. 'Observational evidence for selfinteracting cold dark matter'. In: *Phys. Rev. Lett.* 84 (2000), pp. 3760–3763. DOI: 10.1103/PhysRevLett.84.3760. arXiv: astro-ph/9909386.

[100] Laura G. van den Aarssen, Torsten Bringmann and Christoph Pfrommer. 'Is dark matter with long-range interactions a solution to all small-scale problems of \Lambda CDM cosmology?' In: *Phys. Rev. Lett.* 109 (2012), p. 231301. DOI: 10.1103/PhysRevLett.109.231301. arXiv: 1205.5809 [astro-ph.CO].

[101] Paolo Gondolo and Graciela Gelmini. 'Cosmic abundances of stable particles: Improved analysis'. In: *Nuclear Physics, Section B* (1991). ISSN: 05503213. DOI: 10.1016/0550-3213(91)90438-4.

[102] Michael E. Peskin and Daniel V. Schroeder. *An Introduction to quantum field theory*. Reading, USA: Addison-Wesley, 1995. ISBN: 978-0-201-50397-5.

[103] Kim Griest and David Seckel. 'Three exceptions in the calculation of relic abundances'. In: *Phys. Rev. D* 43 (1991), pp. 3191–3203. DOI: 10.1103/PhysRevD.43.3191.

[104] Torsten Bringmann et al. 'Precise dark matter relic abundance in decoupled sectors'. In: (July 2020). arXiv: 2007.03696 [hep-ph].

[105] Gary Steigman, Basudeb Dasgupta and John F. Beacom. 'Precise Relic WIMP Abundance and its Impact on Searches for Dark Matter Annihilation'. In: *Phys. Rev. D* 86 (2012), p. 023506. DOI: 10.1103/PhysRevD.86.023506. arXiv: 1204.3622 [hep-ph].

[106] Kari Enqvist et al. 'Standard Model with a real singlet scalar and inflation'. In: *JCAP* 08 (2014), p. 035. DOI: 10.1088/1475-7516/2014/08/035. arXiv: 1407.0659 [astro-ph.CO].

[107] Fatemeh Elahi, Christopher Kolda and James Unwin. 'UltraViolet Freeze-in'. In: *JHEP* 03 (2015), p. 048. DOI: 10.1007/JHEP03(2015)048. arXiv: 1410.6157 [hep-ph].

[108] Mattias Blennow, Enrique Fernandez-Martinez and Bryan Zaldivar. 'Freeze-in through portals'. In: *JCAP* 01 (2014), p. 003. DOI: 10.1088/1475-7516/2014/01/003. arXiv: 1309.7348 [hep-ph].

[109] Saniya Heeba, Felix Kahlhoefer and Patrick Stöcker. 'Freeze-in production of decaying dark matter in five steps'. In: *JCAP* 11 (2018), p. 048. DOI: 10.1088/1475-7516/2018/11/048. arXiv: 1809.04849 [hep-ph].

[110] Ashok K. Das. *Finite Temperature Field Theory*. New York: World Scientific, 1997. ISBN: 978-981-02-2856-9.

[111] Giorgio Arcadi et al. 'Real Scalar Dark Matter: Relativistic Treatment'. In: *JHEP* 08 (2019), p. 050. DOI: 10.1007/JHEP08(2019)050. arXiv: 1906.07659 [hep-ph].

[112] Mariano Quiros. 'Finite temperature field theory and phase transitions'. In: *ICTP Summer School in High-Energy Physics and Cosmology*. Jan. 1999. arXiv: hep-ph/9901312.

[113] Matthew D. Schwartz. *Quantum Field Theory and the Standard Model*. Cambridge University Press, Mar. 2014. ISBN: 978-1-107-03473-0.

[114] Greg W. Anderson and Lawrence J. Hall. 'The Electroweak phase transition and baryogenesis'. In: *Phys. Rev. D* 45 (1992), pp. 2685–2698. DOI: 10.1103/PhysRevD.45.2685.

[115] D. A. Kirzhnits. 'Weinberg model in the hot universe'. In: *JETP Lett.* 15 (1972), pp. 529–531.

[116] L. Dolan and R. Jackiw. 'Symmetry behavior at finite temperature'. In: *Phys. Rev. D* 9 (12 June 1974), pp. 3320–3341. DOI: 10.1103/PhysRevD.9.3320. URL: https://link.aps.org/doi/10.1103/PhysRevD.9.3320.

[117] Steven Weinberg. 'Gauge and global symmetries at high temperature'. In: *Phys. Rev. D* 9 (12 June 1974), pp. 3357–3378. DOI: 10.1103/PhysRevD.9.3357. URL: https://link.aps.org/doi/10.1103/PhysRevD.9.3357.

[118] D. A. Kirzhnits and Andrei D. Linde. 'Macroscopic Consequences of the Weinberg Model'. In: *Phys. Lett. B* 42 (1972), pp. 471–474. DOI: 10.1016/0370-2693(72)90109-8.

[119] D. A. Kirzhnits and Andrei D. Linde. 'A Relativistic phase transition'. In: *Zh. Eksp. Teor. Fiz.* 67 (1974), pp. 1263–1275.

[120] D. A. Kirzhnits and Andrei D. Linde. 'Symmetry Behavior in Gauge Theories'. In: *Annals Phys.* 101 (1976), pp. 195–238. DOI: 10.1016/0003-4916(76)90279-7.

[121] Andrei D. Linde. 'Phase Transitions in Gauge Theories and Cosmology'. In: *Rept. Prog. Phys.* 42 (1979), p. 389. DOI: 10.1088/0034-4885/42/3/001.

[122] Andrei D. Linde. 'GRAND BANG'. In: *Phys. Lett. B* 99 (1981), pp. 391–395. DOI: 10.1016/0370-2693(81)90555-4.

[123] S. M. Boucenna and S. Morisi. 'Theories relating baryon asymmetry and dark matter: A mini review'. In: *Front. in Phys.* 1 (2014), p. 33. DOI: 10.3389/fphy.2013.00033. arXiv: 1310.1904 [hep-ph].

[124] Anupam Mazumdar and Graham White. 'Review of cosmic phase transitions: their significance and experimental signatures'. In: *Rept. Prog. Phys.* 82.7 (2019), p. 076901. DOI: 10.1088/1361-6633/ab1f55. arXiv: 1811.01948 [hep-ph].

[125] Daniel J. H. Chung, Andrew J. Long and Lian-Tao Wang. '125 GeV Higgs boson and electroweak phase transition model classes'. In: *Phys. Rev. D* 87 (2 Jan. 2013), p. 023509. DOI: 10.1103/PhysRevD.87.023509. URL: https://link.aps.org/doi/10.1103/PhysRevD.87.023509.

[126] A. Bazavov et al. 'The chiral and deconfinement aspects of the QCD transition'. In: *Phys. Rev. D* 85 (2012), p. 054503. DOI: 10.1103/PhysRevD.85.054503. arXiv: 1111.1710 [hep-lat].

[127] Benjamin W. Lee, C. Quigg and H. B. Thacker. 'Weak Interactions at Very High-Energies: The Role of the Higgs Boson Mass'. In: *Phys. Rev. D* 16 (1977), p. 1519. DOI: 10.1103/PhysRevD.16.1519.

[128] James M. Cline et al. 'Update on scalar singlet dark matter'. In: *Phys. Rev. D* 88 (2013). [Erratum: Phys.Rev.D 92, 039906 (2015)], p. 055025. DOI: 10.1103/PhysRevD.88.055025. arXiv: 1306.4710 [hep-ph].

[129] M. Spira et al. 'Higgs boson production at the LHC'. In: *Nucl. Phys. B* 453 (1995), pp. 17–82. DOI: 10.1016/0550-3213(95)00379-7. arXiv: hep-ph/9504378.

[130] Michael Spira. 'Higgs Boson Production and Decay at Hadron Colliders'. In: *Prog. Part. Nucl. Phys.* 95 (2017), pp. 98–159. DOI: 10.1016/j.ppnp.2017.04.001. arXiv: 1612.07651 [hep-ph].

[131] A. Djouadi, M. Spira and P. M. Zerwas. 'Production of Higgs bosons in proton colliders: QCD corrections'. In: *Phys. Lett. B* 264 (1991), pp. 440–446. DOI: 10.1016/0370-2693(91)90375-Z.

[132] K. G. Chetyrkin, Bernd A. Kniehl and M. Steinhauser. 'Hadronic Higgs decay to order alpha-s**4'. In: *Phys. Rev. Lett.* 79 (1997), pp. 353–356. DOI: 10.1103/PhysRevLett.79.353. arXiv: hep-ph/9705240.

[133] P. A. Baikov and K. G. Chetyrkin. 'Top Quark Mediated Higgs Boson Decay into Hadrons to Order α_s^5'. In: *Phys. Rev. Lett.* 97 (2006), p. 061803. DOI: 10.1103/PhysRevLett.97.061803. arXiv: hep-ph/0604194.

[134] A. Djouadi, J. Kalinowski and M. Spira. 'HDECAY: A Program for Higgs boson decays in the standard model and its supersymmetric extension'. In: *Comput. Phys. Commun.* 108 (1998), pp. 56–74. DOI: 10.1016/S0010-4655(97)00123-9. arXiv: hep-ph/9704448.

[135] John McDonald. 'Gauge singlet scalars as cold dark matter'. In: *Phys. Rev. D* 50 (1994), pp. 3637–3649. DOI: 10.1103/PhysRevD.50.3637. arXiv: hep-ph/0702143.

[136] Valentin V. Khoze and Michael Spannowsky. 'Higgsplosion: Solving the hierarchy problem via rapid decays of heavy states into multiple Higgs bosons'. In: *Nucl. Phys. B* 926 (2018), pp. 95–111. DOI: 10.1016/j.nuclphysb.2017.11.002. arXiv: 1704.03447 [hep-ph].

[137] Martin Wolfgang Winkler. 'Decay and detection of a light scalar boson mixing with the Higgs boson'. In: *Phys. Rev. D* 99.1 (2019), p. 015018. DOI: 10.1103/PhysRevD.99.015018. arXiv: 1809.01876 [hep-ph].

[138] Benjamin Grinstein, Lawrence J. Hall and Lisa Randall. 'Do B meson decays exclude a light Higgs?' In: *Phys. Lett. B* 211 (1988), pp. 363–369. DOI: 10.1016/0370-2693(88)90916-1.

[139] C. P. Burgess, Maxim Pospelov and Tonnis ter Veldhuis. 'The Minimal model of nonbaryonic dark matter: A Singlet scalar'. In: *Nucl. Phys. B* 619 (2001), pp. 709–728. DOI: 10.1016/S0550-3213(01)00513-2. arXiv: hep-ph/0011335.

[140] Yann Mambrini. 'Invisible Higgs and Scalar Dark Matter'. In: *J. Phys. Conf. Ser.* 375 (2012). Ed. by Lothar Oberauer, Georg Raffelt and Robert Wagner, p. 012045. DOI: 10.1088/1742-6596/375/1/012045. arXiv: 1112.0011 [hep-ph].

[141] Carlos E. Yaguna. 'Gamma rays from the annihilation of singlet scalar dark matter'. In: *JCAP* 03 (2009), p. 003. DOI: 10.1088/1475-7516/2009/03/003. arXiv: 0810.4267 [hep-ph].

[142] A. Goudelis, Y. Mambrini and C. Yaguna. 'Antimatter signals of singlet scalar dark matter'. In: *JCAP* 12 (2009), p. 008. DOI: 10.1088/1475-7516/2009/12/008. arXiv: 0909.2799 [hep-ph].

[143] Carlos E. Yaguna. 'The Singlet Scalar as FIMP Dark Matter'. In: *JHEP* 08 (2011), p. 060. DOI: 10.1007/JHEP08(2011)060. arXiv: 1105.1654 [hep-ph].

[144] Geneviève Bélanger et al. 'micrOMEGAs5.0 : Freeze-in'. In: *Comput. Phys. Commun.* 231 (2018), pp. 173–186. DOI: 10.1016/j.cpc.2018.04.027. arXiv: 1801.03509 [hep-ph].

[145] P. F. de Salas et al. 'Bounds on very low reheating scenarios after Planck'. In: *Phys. Rev. D* 92.12 (2015), p. 123534. DOI: 10.1103/PhysRevD.92.123534. arXiv: 1511.00672 [astro-ph.CO].